

Fluorescent Nanoparticles for Ion Sensing

Dissertation

zur Erlangung des akademischen Grades doctor rerum naturalium

(Dr. rer. nat.)

vorgelegt dem Rat der Chemisch-Geowissenschaftlichen Fakultät der
Friedrich-Schiller-Universität Jena

von Diplom-Chemikerin Anja Schulz, geb. Gräfe
geboren am 05.12.1981 in Merseburg

Gutachter 1: Dr. habil. Gerhard J. Mohr; FSU Jena
Gutachter 2: Prof. Dr. Thomas Heinze; FSU Jena
Tag der öffentlichen Verteidigung: 08. Juli 2009

Contents

1	Introduction	7
1.1	Theoretical Aspects	7
1.1.1	Fluorescence Spectroscopy	7
1.1.2	Fluorescence Quenching Processes	9
1.1.3	Size and Size Distribution	14
1.1.4	Zeta-Potential	15
1.2	State of the Art	16
1.2.1	Optical Chemical Sensors	18
1.2.2	Nanoparticles in Sensing	20
1.3	Motivation	26
1.3.1	Important Ionic Analytes	26
1.3.2	Suitable Indicator and Reference Dyes	27
1.3.3	Immobilization of the Sensor Dyes	29
1.4	Aims	31
2	Poly(acrylamide) Nanoparticles	32
2.1	Structural and Physico-chemical Properties	32
2.1.1	Size and Size Distribution	35
2.1.2	Density and Specific Surface	37
2.1.3	Solid State-NMR Spectroscopy	38
2.1.4	Zeta Potential	41
2.2	Chloride-Sensitive Nanoparticles	42
2.2.1	Structural Properties of the Fluorescent Nanoparticles	43
2.2.2	Absorption and Fluorescence	44

2.2.3	Response to Halides and Pseudohalides	46
2.2.4	Interfering Species	48
2.2.5	Oxidation of the Fluorophores	51
2.2.6	Application of the NPs inside Living Cells	52
2.3	pH-Sensitive Nanoparticles	55
2.3.1	pH-Sensing using Fluorescent Indicators	55
2.3.2	Influence of Dye Immobilization	60
2.3.3	Absorption and Fluorescence	62
2.3.4	Response to pH	67
2.3.5	Interfering Species	68
2.3.6	Photostability and Stability against Oxidation	71
3	Functionalization of Nanoparticles	73
3.1	Surface Coating	73
3.2	pH-swellaable poly(DEAMA) Nanoparticles	75
3.3	Core-Shell Nanoparticles	77
3.3.1	Size and Zeta-Potential	79
3.3.2	Fluorescence and Sensing Properties	80
4	Discussion and Conclusion	83
4.1	Inverse Microemulsion Polymerization	83
4.2	Structural and Physico-chemical Properties	84
4.3	Chloride-Sensitive Nanoparticles	85
4.4	pH-Sensitive Nanoparticles	88
4.5	Functionalized Nanoparticles	90
5	Summary and Outlook	93
6	Zusammenfassung und Ausblick	95
7	Experimental	97
7.1	Apparatus and Materials	97
7.2	Procedures	99
7.2.1	Synthesis of the Polymerizable Dyes	99

7.2.2	Preparation of the Nanoparticles	103
7.2.3	Cell Transfection Procedure	106
	References	107
	List of Figures	110
	List of Tables	112
	Appendix	113
	A Investigated Fluorophores	114
	B Spectra	115
	List of Publications	117
	Curriculum Vitæ	119
	Danksagung	120
	Selbständigkeitserklärung	121

Abbreviation Index

AAm	Acrylamide
AAPH	2,2'-Azobis(2-methylpropionamide) dihydrochloride
AIBN	2,2'-Azobis(2-methylpropionitrile)
AOT	Bis(2-ethylhexyl) sulfosuccinate sodium salt
APS	Ammonium peroxydisulfate
ATP	Adenosine 5'-triphosphate
BET	Brunauer, Emmett and Teller
Brij 30	Polyethylene glycol dodecyl ether (main component: tetraethylene glycol dodecyl ether)
BSA	Bovine Serum Albumin
CHO	Chinese Hamster Ovary
CTAB	Cetyltrimethylammonium bromide
d_H	Hydrodynamic Diameter
DLS	Dynamic Light Scattering
DEAMA	<i>N,N</i> Diethyl-2-aminoethyl methacrylate
DMAPA	<i>N,N</i> -Dimethyl-2-aminopropyl acrylamide
DMSO	Dimethyl sulfoxide
ϵ	Molar Extinction Coefficient
ϕ	Quantum Yield
HOMO	Highest Occupied Molecule Orbital
HPTS	8-Hydroxy-1,3,6-pyrene trisulfonic acid
K_{SV}	Stern-Volmer Constant
IS	Ionic Strength
LUMO	Lowest Unoccupied Molecule Orbital
m/z	Mass-to-Charge Ratio
MAS	Magic Angle Spinning
MBAAm	<i>N,N'</i> -Methylene bisacrylamide

mp	Melting Point
MS	Mass Spectrometry
ss-NMR	Solid-state Nuclear Magnetic Resonance
NPs	Nanoparticles
PDI	Polydispersity Index
PEBBLE	Probes Encapsulated by Biologically Localized Embedding
PEGDMA	Poly(ethylene glycol) dimethacrylate
PEI	Poly(ethyleneimine)
PET	Photoinduced Electron Transfer
RET	Resonance Energy Transfer
SEM	Scanning Electron Microscope
TEA	Triethylamine
TEMED	<i>N,N,N',N'</i> -Tetramethylethylenediamine
TLC	Thin Layer Chromatography
w/o	Water-in-Oil

1

Introduction

1.1 Theoretical Aspects

1.1.1 Fluorescence Spectroscopy

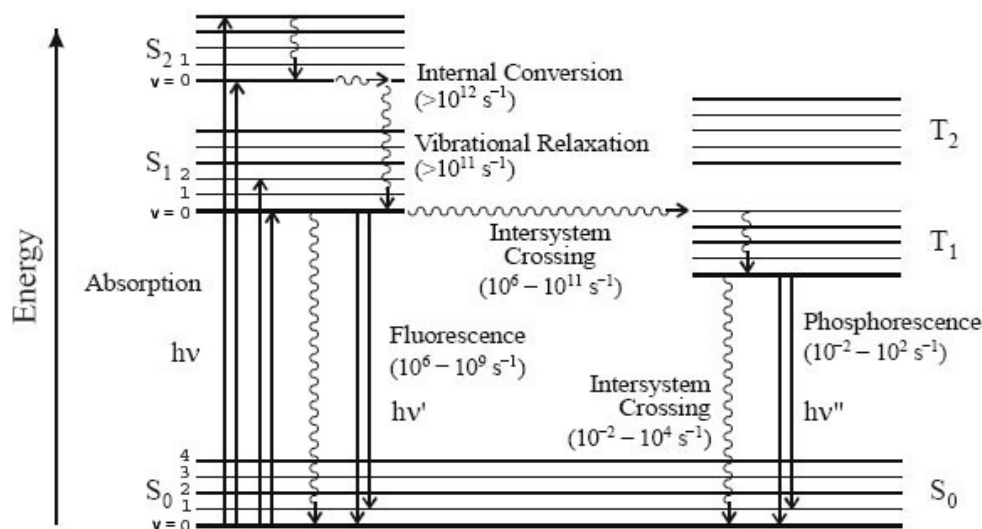


Figure 1.1: Jablonski diagram showing radiative (straight lines) and non-radiative (sinuous lines) electron transition processes. The electronic ground and excited states (S_0 , S_1 , S_2 and T_1) show further differentiation into vibrational levels (depicted by $v = 0, 1, 2, \dots$). Picture adapted from Handbook of Photochemistry.¹

Photoluminescence combines the terms fluorescence and phosphorescence, which are considered as cold light emission processes from electronically excited molecule

states.¹⁻³ The best overview about these processes gives **Figure 1.1** showing the Jablonski-Perrin diagram. If a molecule is irradiated with light, electrons from the ground state take up the energy and the molecule is brought to an excited state of higher energy. That part of the light with the wavelength corresponding to the energy gap between the ground and the excited state is absorbed. Phosphorescence occurs, if an electron from a triplet excited state (T_1), in which the electron has the same spin orientation as the electron in the ground state, returns to the singlet ground state (S_0). Theoretically the transition from the triplet to the singlet state is forbidden and thus the emission rate is slow. This leads to the relatively long phosphorescence lifetimes of 10^{-3} to 10^0 seconds. In contrast, fluorescence is light emission due to the transition of a paired electron (opposite spin orientation) from an excited singlet state (S_1, S_2) to the singlet ground state. The spin allowed transition process leads to faster emission rates and hence, much shorter fluorescence lifetimes in the range of a few nanoseconds.

According to the Born-Oppenheimer approximation the electronic transitions are much faster (10^{-15} s) than the movement of the atom nuclei in their environment (10^{-10} to 10^{-12} s). Thus the electronic transition is most likely to occur without changes in the position of the nuclei. As a consequence of this so-called Franck-Condon principle the transitions from one energy potential curve to another are vertical. Upon light-induced excitation of a luminescent molecule, it can exist in some higher vibrational levels of the S_1 or S_2 state. As seen in **Figure 1.2** the vertical transition from the ground to the excited state is the most probable and thus shows the highest intensity in the absorption spectrum. Rapidly, a non-radiative vibrational relaxation of the excited molecule to the lowest vibrational state follows. This so-called internal conversion takes only 10^{-12} s compared to the slower process of fluorescence (10^{-6} to 10^{-9} s). Hence, internal conversion is mostly prior to emission of fluorescence and relaxation to the ground state occurs from the lowest vibrational level of the excited state.

The emission to the ground state ends in a higher vibrational level of S_0 due to the Franck-Condon principle (vertical transition). The vertical transition exhibits the highest intensity in the resulting emission spectrum. The molecule quickly reaches

thermal equilibrium after vibrational deactivation. As a result of internal conversion and vibrational deactivation the energy of fluorescence emission is less than that of absorption. Therefore, the emission maximum in spectra of fluorophores in solution is usually shifted to longer wavelengths. The gap between the wavelengths maximum of the emission and the absorption spectra is called Stoke's shift. In fluorescence spectroscopy, fluorophores with a large Stoke's shift are preferred, because commercially available glass filters can be used, without filtering off parts of the incident or emitted light.

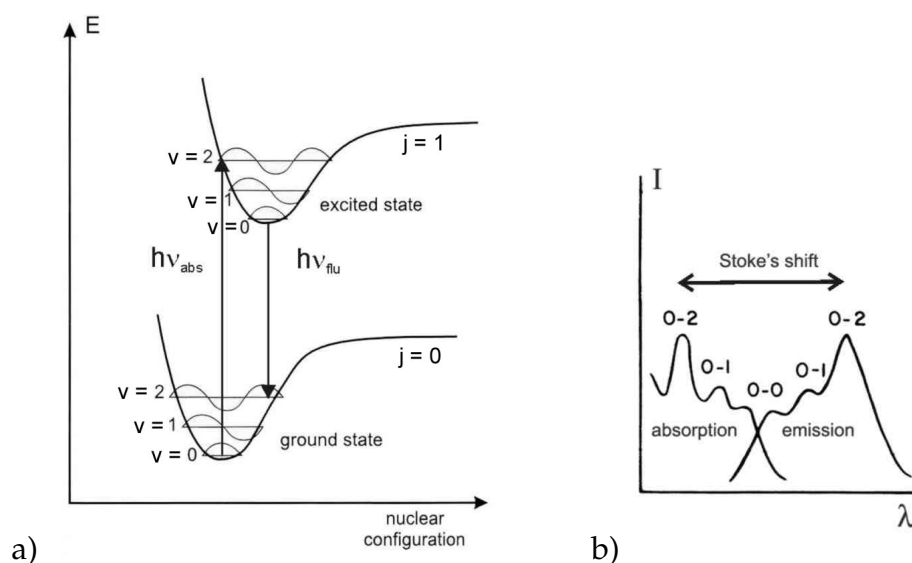


Figure 1.2: a) Energy potential curves of a fluorophore in the electronic ground ($j = 0$) and excited state ($j = 1$). Absorption and emission of light are depicted as vertical transitions according to the Franck-Condon principle. b) The resulting Stoke's shift for the absorption and emission spectra.

1.1.2 Fluorescence Quenching Processes

Beside the emission of light (fluorescence) other relaxation processes of an excited molecule (M^*) are known that result in a decrease of fluorescence intensity (=fluorescence quenching). Some of them, such as:

- static and dynamic quenching
- formation of excimers and exiplexes
- photoinduced electron transfer (PET)

- photoinduced proton transfer and
- resonance energy transfer (RET)

involve the presence of a quencher molecule (Q). Observation of the fluorescence quenching provides information about the environment of the fluorophore and therefore about the concentration of Q. Important mechanisms are presented in the following.

Static and Dynamic Quenching

Both static and dynamic quenching are reversible processes and occur upon collision of an excited fluorophore with heavy ions like Br^- and Cl^- or with paramagnetic species (e.g. O_2 , NO^\bullet). The processes as well as the fluorescence lifetimes differ in their dependence on temperature and viscosity. Collisional quenching of a fluorophore is supposed to occur upon intersystem crossing (ISC) from the first excited singlet state (S_1) to the excited triplet state (T_1). The intrinsically forbidden ISC is possible due to spin-orbit coupling with a heavy atom or ion (e.g. halides). The efficiency of spin-orbit coupling depends on the fourth power of the atomic number and is therefore favored by the presence of heavy quenching species. The deactivation of the triplet state fluorophore can take place by phosphorescence, non-radiative processes or after quenching by dissolved oxygen.

Static quenching can be observed in two cases: (1) M and Q form a stable ground state non-fluorescent complex (MQ). (2) The quencher Q is in close distance to M^* and thus inside the so-called effective sphere of quenching. Inside this imaginary sphere around M^* no fluorescence of M^* is observed due to quenching. This process is mainly observed for high concentrations of Q or in viscous/rigid matrices (**Figure 1.3**).

But collision of M^* and Q can also lead to dynamic quenching or simultaneous dynamic and static quenching. **Figure 1.4 a)** schematically shows the deactivation pathways of M^* and the corresponding rate constants. The rate constant for deactivation by quenching is k_q and the rate constant k_M for radiative deactivation of M^* is determined by the fluorescence lifetime of M^* in absence of Q (τ_0). According to this scheme the fluorescence lifetime and therefore also the fluorescence intensity of

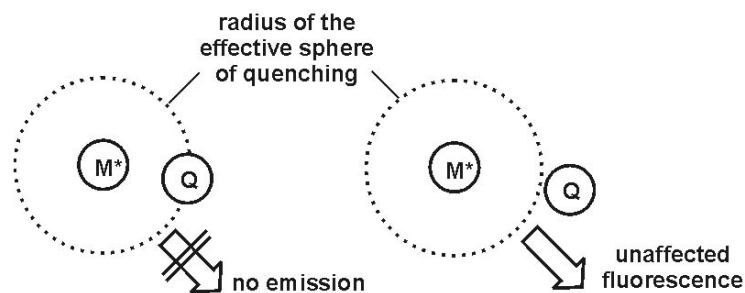


Figure 1.3: Static quenching of M^* at high concentrations of Q or in viscous or rigid matrices. Picture according to B. Valeur.²

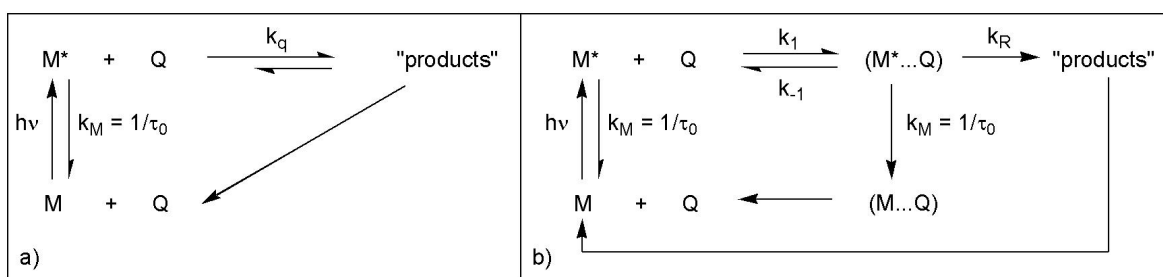


Figure 1.4: Schematic drawing of the deactivation pathways of M^* and the corresponding rate constants. Scheme according to B. Valeur.²

M^* depends on the concentration of Q . The relation is described by the Stern-Volmer equation, which is commonly used for quantitative optical determination of anions like chloride, bromide and iodide:

$$\frac{\tau_0}{\tau} = \frac{F_0}{F} = 1 + k_q \tau_0 [Q] = 1 + K_{SV} [Q] \quad (1.1)$$

F_0 and τ_0 are the fluorescence intensity and lifetime of the fluorophore in absence, and F and τ are the fluorescence intensity and lifetime in presence of the quenching species, respectively. Plotting the ratio of F_0/F against the quencher concentration gives the Stern-Volmer quenching constant K_{SV} .² The higher the quenching constant the more sensitive is the fluorophore to the quencher.

Dynamic quenching also known as Stern-Volmer quenching involves diffusion of M^* and Q to form an encounter pair ($M^* \cdots Q$) that “reacts” to the non-fluorescent species as depicted in **Figure 1.4 b**). Hence, the fluorescence quenching process consists of a diffusion controlled formation of the encounter pair (described by the rate constants k_1 and k_{-1}) and the subsequent formation of the “products” (described

by k_R). In case of $k_R \gg k_1[Q], k_{-1}, k_M$ then the overall rate for quenching of M^* is diffusion limited. That means k_q is equal to k_1 . The rate constant for the formation of the encounter pair depends on the diffusion coefficients of M^* and Q which in turn depend on the viscosity of the solvent. The higher the viscosity of a medium the lower the diffusion coefficients and the slower the formation of the encounter pair. That decreases the overall quenching constant k_q and in order to that the Stern-Volmer constant.

Photoinduced Electron Transfer (PET)

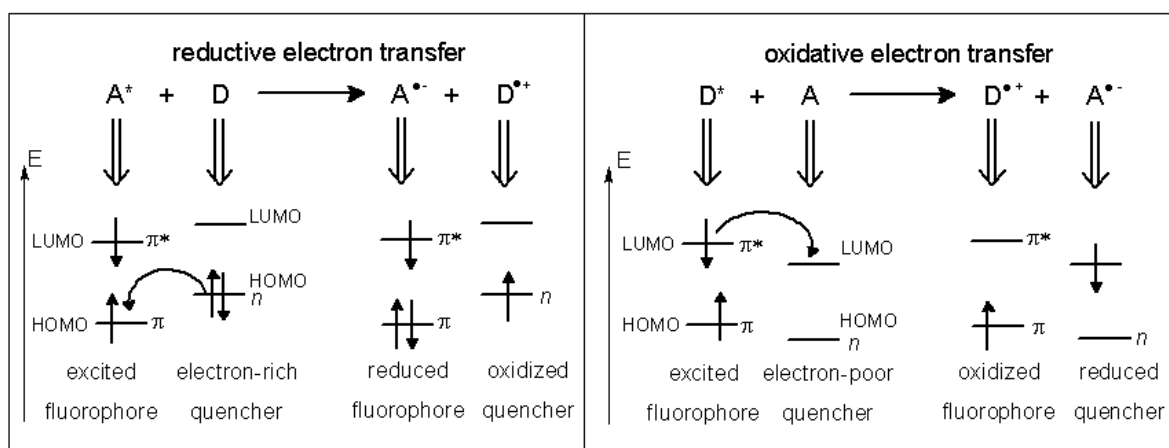


Figure 1.5: Intermolecular reductive and oxidative PET between an excited fluorophore and a quencher.²

Photoinduced electron transfer describes processes that prevent the relaxation of the excited state electron of a fluorophore (LUMO) to the ground state (HOMO) of the fluorophore. The emission of light (fluorescence) which commonly follows the relaxation is therefore prevented as well. The photoinduced electron transfer can be distinguished into inter- and intramolecular exchange of electrons between an electron donor (D) and an electron acceptor (A). The oxidative and reductive intermolecular electron transfer between an excited state fluorophore and a quencher molecule is depicted in **Figure 1.5**. The more important process for this work is the intramolecular transfer of electrons, which usually occurs from an electron-rich part of the molecule (donor) to the aromatic system (acceptor) as shown in **Figure 1.6**

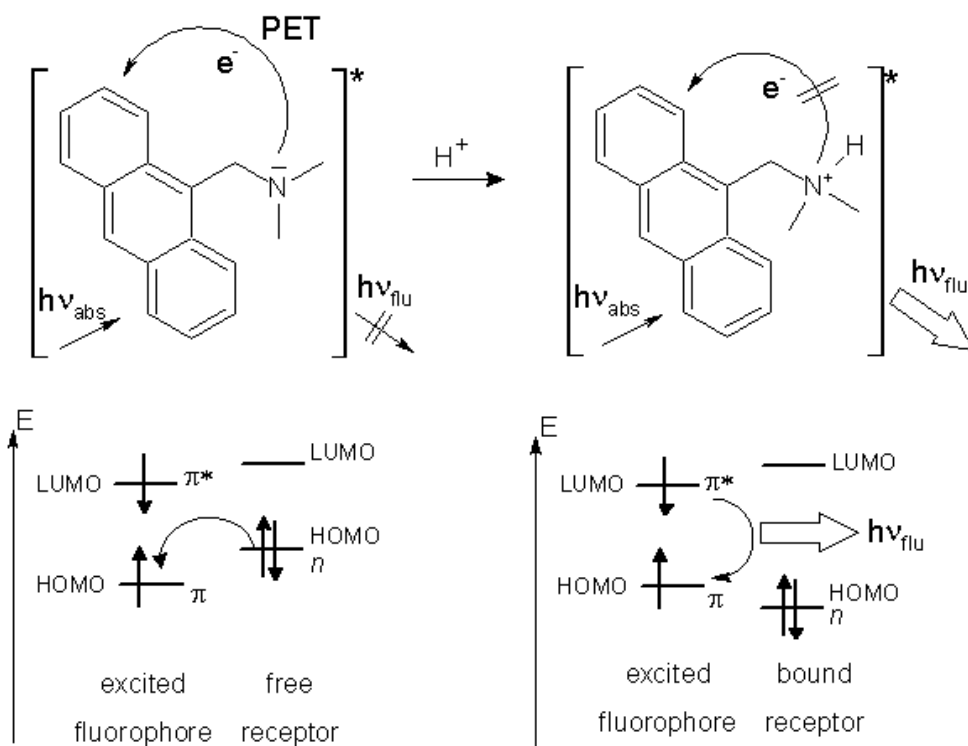


Figure 1.6: Mechanism of intramolecular PET used for sensing of protons.

for *N,N*-dimethylaminomethyl anthracene.⁴ The lone pair of the tertiary nitrogen transfers an electron to the HOMO of the excited molecule and no fluorescence is observed. In presence of protons the lone pair of the receptor group is used to bind the protons and strong fluorescence becomes visible. This example shows how PET can be used for sensing of analytes, which are able to react with a receptor group connected to a fluorophore.

Resonance Energy Transfer (RET)

Energy transfer is observed due to excited state interaction between a fluorescent donor and a fluorescent acceptor molecule. The transfer of energy can occur in two manners: (1) radiative, which involves emission and re-absorption of photons and (2) non-radiative energy transfer due to dipole-dipole coupling between donor and acceptor. A non-radiative energy transfer takes place, if the emission spectra of the donor overlaps with the absorption spectra of the acceptor fluorophore (**Figure 1.7**). That means the vibrational transitions in the donor are coupled (i.e. are in reso-

nance) to the corresponding transitions in the acceptor that have the same energy. The integral of the overlap between donor emission and acceptor absorption determines the rate of resonance energy transfer. Additionally, the distance between the two molecules and their relative orientation to each other contributes to the efficiency of RET. This can be used for analytical purposes, since the RET delivers information about the distance (r) between the donor and acceptor molecule according to the following equation:

$$E = \frac{R_0^6}{R_0^6 + r^6} \quad (1.2)$$

E is the efficiency of the energy transfer and R_0 is the distance between donor and acceptor, where the transfer efficiency is 50% (Förster distance). In the literature R_0 is tabulated for several donor-acceptor pairs.²

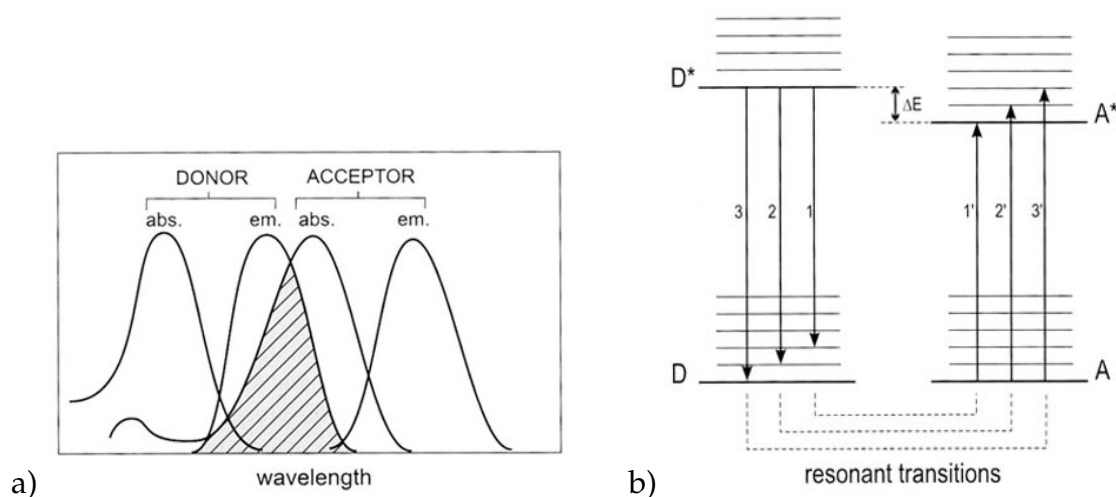


Figure 1.7: a) Absorption and emission spectra illustrating the integral overlap between donor emission and acceptor absorption. b) The energy level scheme shows the resonant transitions between donor and acceptor. Picture adapted from B. Valeur.²

1.1.3 Size and Size Distribution

The size of nanoparticles can be determined using dynamic light scattering (DLS). By measuring the Brownian motion of the particles their size can be calculated. The larger the particles, the slower the Brownian motion will be. The velocity of the particle motion is defined by the so-called translational diffusion coefficient D from

which the hydrodynamic diameter d_H of the particles is calculated using the Stokes-Einstein equation:

$$d_H = \frac{kT}{3\pi\eta D} \quad (1.3)$$

where k is the Boltzmann's constant, T the absolute temperature and η the viscosity of the solvent. The diameter that is obtained by this technique is the diameter of a sphere that has the same translational diffusion coefficient as the particle and is thus called hydrodynamic diameter. From the size distribution the polydispersity index (PDI) is received. The lower the PDI of a sample, the more monodisperse are the particles.

1.1.4 Zeta-Potential

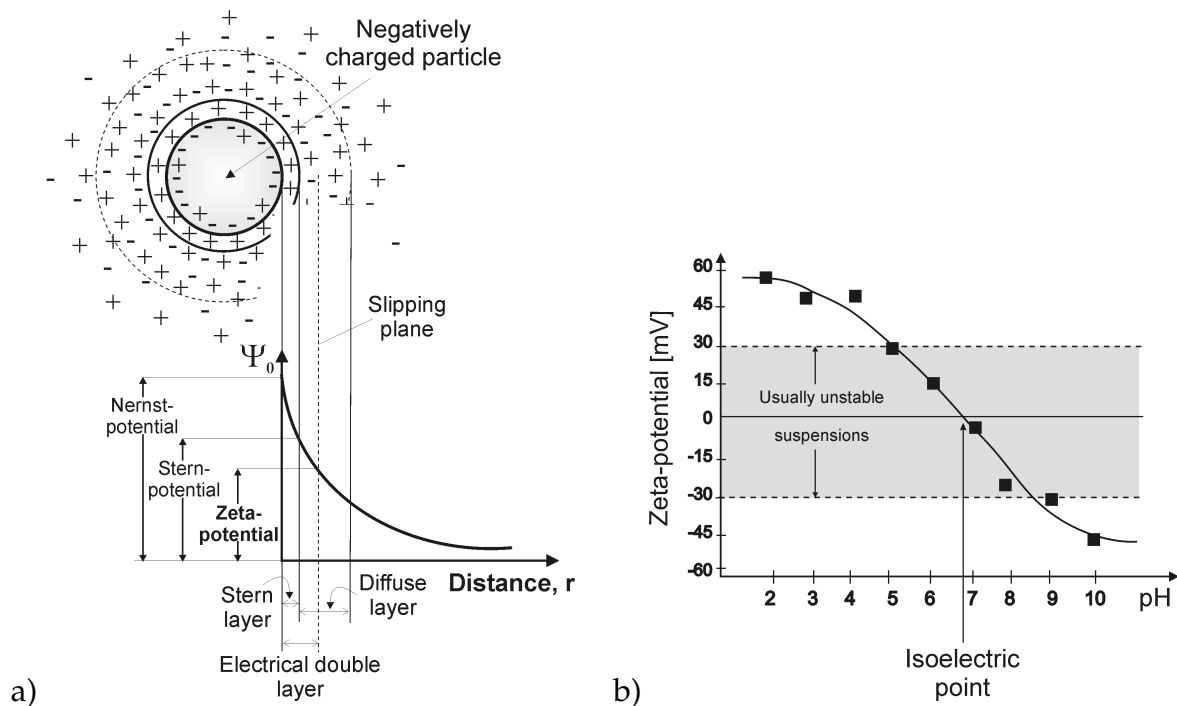


Figure 1.8: a) Schematic drawing of a negatively charged particle and the resulting electrical double layer. The graph depicts the surface-potential (Ψ) depending on the distance (r) from the particle surface. b) The zeta-potential in dependence on the pH of the particle suspension.

Any type of particle in aqueous, buffered suspension exhibits an electric surface charge affecting the distribution of ions in the surrounding solution. Close to

the surface of the particle the concentration of ions with opposite charge to that of the particle increases. In this manner a so-called electrical double layer builds up around each particle. The liquid layer consists of an inner region where the ions are strongly associated to the surface of the particle and a diffuse outer region where they are more loosely bound. The particle and the double layer form a stable entity and if the particle moves, the ions outside this boundary stay with the bulk aqueous phase. **Figure 1.8 a)** exemplary shows a particle having a negative surface charge and the resulting electric double layer. The potential at the boundary relative to the potential of the solvent is called zeta-potential (ζ -potential) or surface of hydrodynamic shear. The zeta-potential strongly depends on the material the particle is made of and on the pH of the particle suspension. At low pH basic surface groups like amines are protonated giving a positive ζ -potential. In contrast, acidic groups at the particle's surface are deprotonated at basic conditions. Hence, the ζ -potential usually decreases with increasing pH of the suspension as shown in **Figure 1.8 b)**. The magnitude of the ζ -potential is a good indicator to predict the stability of colloidal solution. Particles exhibiting ζ -potentials less than -30 mV or higher than +30 mV usually form stable suspensions due sufficient electrostatic repulsion between the particles. Another possibility of stabilization is steric repulsion achieved by substances adsorbed on the surface of the particle.

1.2 State of the Art

Sensors have become omnipresent in the last century, since they encounter us several times a day and accompany us during our whole life. Among mechanical, acoustic, conductive and calorimetric sensors, chemical sensors play a particular role in our daily life. Usually, technical devices, which are able to continuously detect chemical species are referred as chemical sensors. In recent times, also particles, layers and even single molecules like indicator dyes are considered as sensors, but per definition a true sensor requires a signal processing unit. To avoid confusion the concept of "chemosensors" was introduced by Czarnik in 1993. A chemosensor is defined as a compound of abiotic origin that complexes to an analyte reversibly with

a concomitant signal transduction.^{5,6} Furthermore, one has to differentiate between chemical sensors and probes. The latter do not work reversibly and can be found in single shot tests used for e.g. pH-indicator strips or pregnancy tests. Chemical sensors and chemosensors are widely used in medical diagnostic e.g. to control the blood glucose level of Diabetes Mellitus patients or to monitor blood gases and electrolytes.⁷ New insights into the physiology of cells and micro-organisms are made with chemosensors detecting biomolecules such as ATP, dopamine, acetylcholin, glutamate, glycine, aspartate or tracking specific cell organelles (e.g. lysosomes). Even cellular metabolic and transport processes are now visible for the researchers by using chemical sensors (**Figure 1.9**).⁸⁻¹⁰

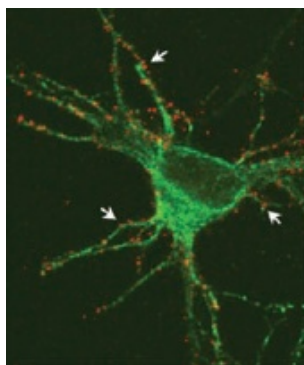


Figure 1.9: Glycine receptors in living neuron cells marked with fluorescent Quantum Dots (red).

Not to forget that the working routine in a chemical laboratory often requires chemical sensing with digital pH-meters. The biological equivalents to artificial chemical sensors are natural receptor molecules, that take part in nearly every biological process. Specific receptors at the surface of neurons, for example, allow the transmission of neuronal signals through the body. But also in our every day life we are surrounded by chemical sensors e.g. in smoke gas detectors, breath testing of alcohol, process control in food and beverage industry¹¹ as well as in electronic noses and tongues.

1.2.1 Optical Chemical Sensors

All the different kinds of sensors have a common design as depicted in **Figure 1.10**. They consist of a receptor site responsible for the recognition of the analyte and a transducer unit for converting the recognition event into an analytically useful signal. The signal from the transducer is usually processed to a computing unit reading out the analytical information. There are different ways to transmit the sensing event to the processing unit, like electrical, mechanical, thermal, magnetic and optical signal transduction. The latter can be further differentiated into colorimetric and luminescent signal transmission. Luminescent signal transduction including fluorescence and phosphorescence is used for most applications as described in the following.

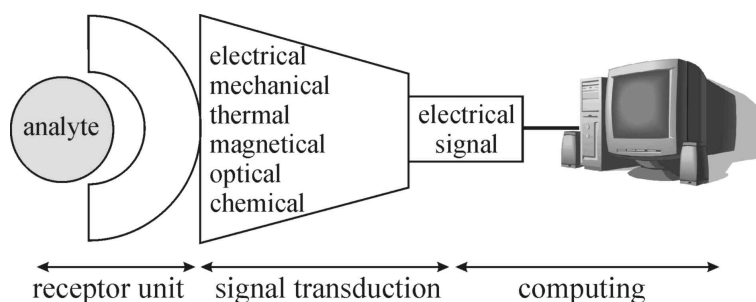


Figure 1.10: General design of a chemical sensor. The analyte is recognized at the receptor unit creating a signal that is transduced to the computing unit.

Optical (and in particular fluorescent) signal transmission has significant advantages compared to the before mentioned methods: (1) The measurement can be performed without direct contact to the sample, which is thus neither contaminated, consumed nor destroyed during analysis. (2) Since the sample is not consumed and the sensor works reversibly, continuous analyte detection is possible, which is necessary for on-line measurements (e.g. in process monitoring). (3) Optical signal transduction is much faster and safer than electrical transduction and needs no calibration/reference electrodes for ratiometric analyte detection. Furthermore, the optical output can be tailored to be compatible with common laser wavelengths. (4) Fluorescence spectroscopy is highly sensitive and even single molecule detection becomes possible with the so-called near-field scanning optical microscopy (NSOM).²

(5) Temporal- and spatially resolved determination of more than one substance simultaneously is achieved.¹⁰ Additionally, the information gathered with fluorescent sensors is very high, since numerous parameters like spectra, fluorescence decay times, energy transfer, quenching efficiency and fluorescence polarization can be determined. (6) Optical sensors are well suited for application in industry and research, because they can be miniaturized and the production costs are low.

Fluorescent chemosensors

As already mentioned one has to distinguish between a true optical sensor device and an indicator dye that signals the presence of a chemical species (chemosensor). In the following the focus will be on such chemosensors involving fluorophores, which can be further classified into:

- (1) fluorophores that are quenched upon collision with the analyte (e.g. O₂, Cl⁻),
- (2) fluorophores reversibly binding to the analyte with subsequent fluorescence quenching or enhancement and
- (3) fluorophores that are linked to a receptor group optionally *via* a spacer unit.

The fluorescence is either quenched or enhanced upon analyte recognition at the receptor due to photoinduced processes such as electron transfer, charge transfer and energy transfer. The schematic designs of the different types of fluorescent molecular sensors are depicted in **Figure 1.11**.

For evaluation the chemosensors are often immobilized on several solid supports depending on the field of application. Today, a number of fiber-optical sensors (also called optodes),¹²⁻¹⁴ sensor layers¹⁵⁻¹⁷ and micro-/nanoparticles^{18,19} are existing for analysis of ions and molecules. All together, the sensing principle is based on indicator dyes that specifically change their spectral properties upon reaction with the analyte. The first fluorescent chemosensor, an indicator dye for the recognition of calcium, was reported by Tsien *et al.* in 1980.^{20,21} The great variety of the indicator dyes and the possibility of functionalizing them allow the specific detection of nearly every chemical substance. Nevertheless, for sufficient performance the inter-

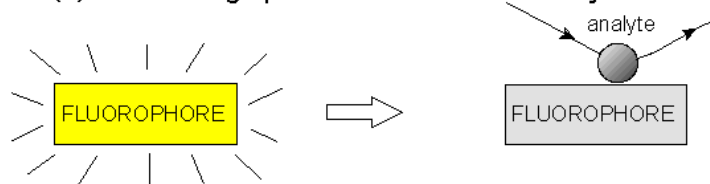
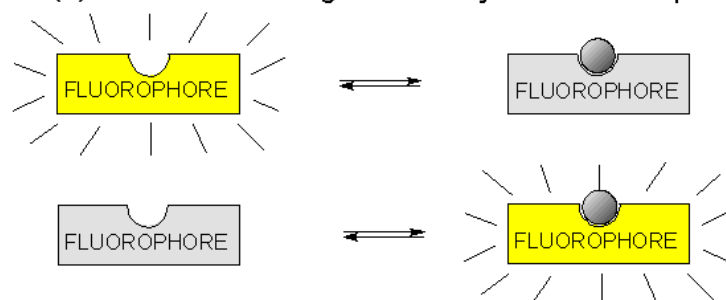
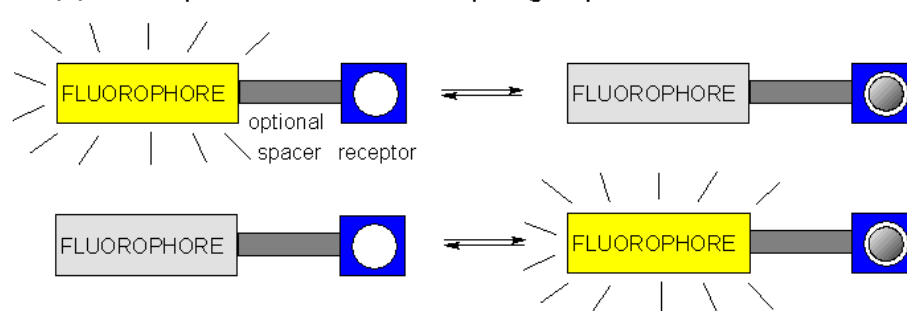
Class (1): Quenching upon collision with the analyte**Class (2): Reversible binding of the analyte to the fluorophore****Class (3): Fluorophores linked to a receptor group**

Figure 1.11: Schematic design of fluorophores for sensing of ions or molecules.

action between the indicator and the analyte has to be very sensitive (in the relevant analytical range), selective, fast and reversible.

1.2.2 Nanoparticles in Sensing

Typically, nanoparticles (NPs) have dimensions ranging from 1 - 1000 nm and can be made of inorganic, organic or composite materials. The most important feature of nano-sized particles is their great surface-to-volume ratio, resulting in modified physico-chemical characteristics compared to the bulk material. The small diameter of nanoparticles makes them highly suitable for sensing purposes in samples of limited dimensions, like cells and micro-organisms, because high loading capaci-

ties and reduced response times are achieved. The analytes to be determined range from simple inorganic ions to neutral organic substances and biomolecules such as proteins. Sensor nanoparticles can consist of various materials (e.g. hydrophilic, biodegradable and hydrophobic organic polymers and dendrimers, silica, zeolite, composite materials, (ferro)-magnetic materials, inorganic oxides, carbon, metals).¹⁸ Fluorescent nano-sized sensors are the most suitable and important tools for sensing purposes in biological samples. They are further distinguished into: (1) materials showing intrinsic fluorescence like quantum dots and fluorescent proteins and (2) NPs with extrinsic fluorescence due to immobilized fluorescent/luminescent dyes. Substances or particles with intrinsic fluorescence play a role as RET-based sensors (see page 13) and for labeling, which enables optical distance measurements. However, the more common sensors are those showing extrinsic fluorescence. In 1995 Wolfbeis *et al.* published one of the earliest articles describing the use of nanoparticles as luminescent sensors. They developed zeolite-Y-nanocrystals with Ru(bipy)₃²⁺ fluorophores immobilized inside the cavities for oxygen sensing.²² Only a few years later the group of Kopelman was one of the first applying fluorescent poly(acrylamide) nanoparticles for sensing of pH and Ca²⁺ in biosamples.²³ Furthermore, they established the term PEBBLE (probes encapsulated by biologically localized embedding), which is now a widely used abbreviation for such fluorescent nanosensors.

To achieve extrinsic fluorescence the particle matrix has to contain one or more fluorophores. The dyes can be located on the surface²⁴ of the particles or they can be incorporated inside the particle matrix *via* simple physical entrapment²⁵ or covalent attachment.²⁶ Embedding the dyes inside the particles is usually preferred over surface attachment, since a higher fluorophore loading is obtained. Additionally, unspecific interactions with other components of the biological samples, which may give changes in fluorescence are prevented (**Figure 1.12**). The development of particles with physical immobilized dyes is much easier, but covalent dye attachment provides more stable signals due to reduced leaching. A drawback of covalent binding of the sensor chemistry to the particles is that dyes with specific functional groups have to be available or synthesized.

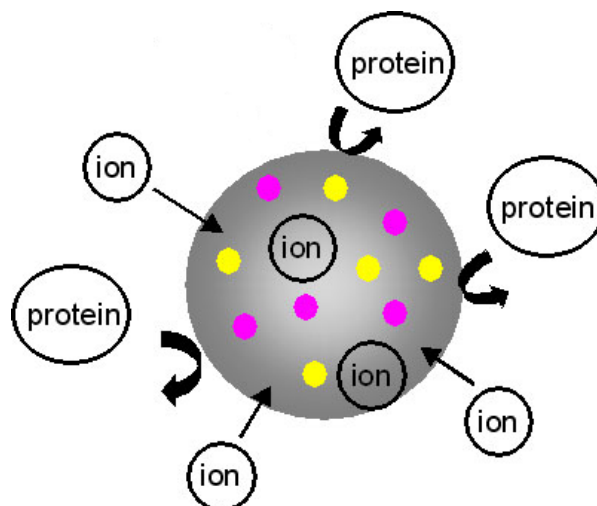


Figure 1.12: Typical design of a sensor nanoparticle with entrapped indicator and reference dyes.

In general, sensor particles show a more uniform distribution in biological samples and are less toxic than most of the available sensing dyes. Effects like aggregation, intercalation into DNA as well as compartmentalization that are observed with plain dyes are prevented. As already mentioned, the dyes are protected from unspecific reactions with proteins, enzymes or DNA in the biosample when embedded in the matrix of particles.²⁷ At the same time sensing of smaller analytes like inorganic ions still remains possible. Another advantage of immobilizing the dyes in NPs is that the matrix can be easily changed or functionalized and thus can be adapted to other sensing conditions. To enable multiple-analyte or ratiometric detection more than one dye is embedded in the particles.

For the delivery of particles into cells or micro-organisms several methods are available. The most common are gene gun, pico-injection, liposomal delivery and phagocytosis as depicted in **Figure 1.13**.¹⁹ Liposomal delivery makes use of cationic lipids so-called transfection reagents which form vesicles (e.g. LipofectamineTM from Invitrogen) and are usually used to deliver DNA to cells. As depicted in **Figure 1.14** the liposomes containing the nanoparticles associate with the cell membrane and are internalized by phagocytosis as well. After the cellular uptake via phagocytosis the particles are mostly located in primary endosomes - small vesicles (0.1 - 1 μm) formed by inversion of the cell membrane.²⁸ The early endosomes fuse

with cellular vesicles to endo-lysosomes in which usually degradation of nutrients take place by enzymes under acidic conditions. The processes are schematically shown in **Figure 1.15**. The cellular internalization of nanoparticles highly depends on the hydrophilicity, surface charge (ζ -potential) and size of the particles as well as on the type of cell.

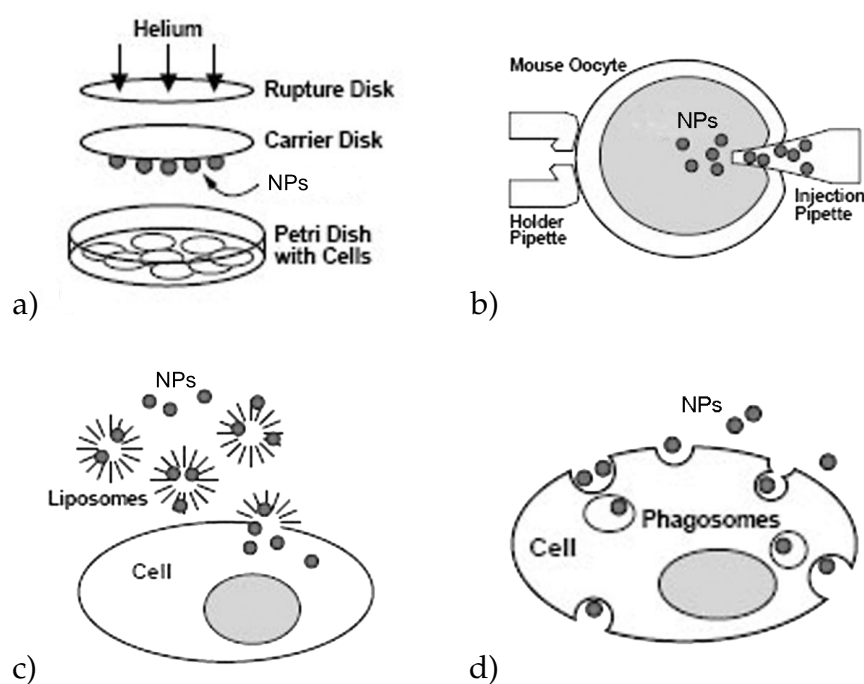


Figure 1.13: Common methods for delivering nanoparticles into cells. a) gene gun, b) picro-injection, c) liposomal delivery and d) phagocytosis. Picture according to Buck *et al.*¹⁹

Since the analytically interesting part of the cell is the cytosol the NPs have to escape from the endosomes. Two theories have been established for the endosomal escape, both employing the much lower pH in endosomes (pH 4.5) compared to the cytosol (pH 7). (1) If the NPs exhibit functional groups such as amino functions they are protonated due to the lower pH in the endosome. In parallel to protonation an active ATPase-driven proton accumulation inside the endosome takes place. This additional proton accumulation inside the endosomes is accompanied by a passive influx of chloride ions. The higher ion concentration inside the endosomes results in an influx of water from the cytosol. The following osmotic swelling of the endosome will cause disruption of the membrane and release of the NPs to the cytosol. This is known as the proton sponge effect (**Figure 1.15**).^{29,30} (2) NPs with a positive sur-

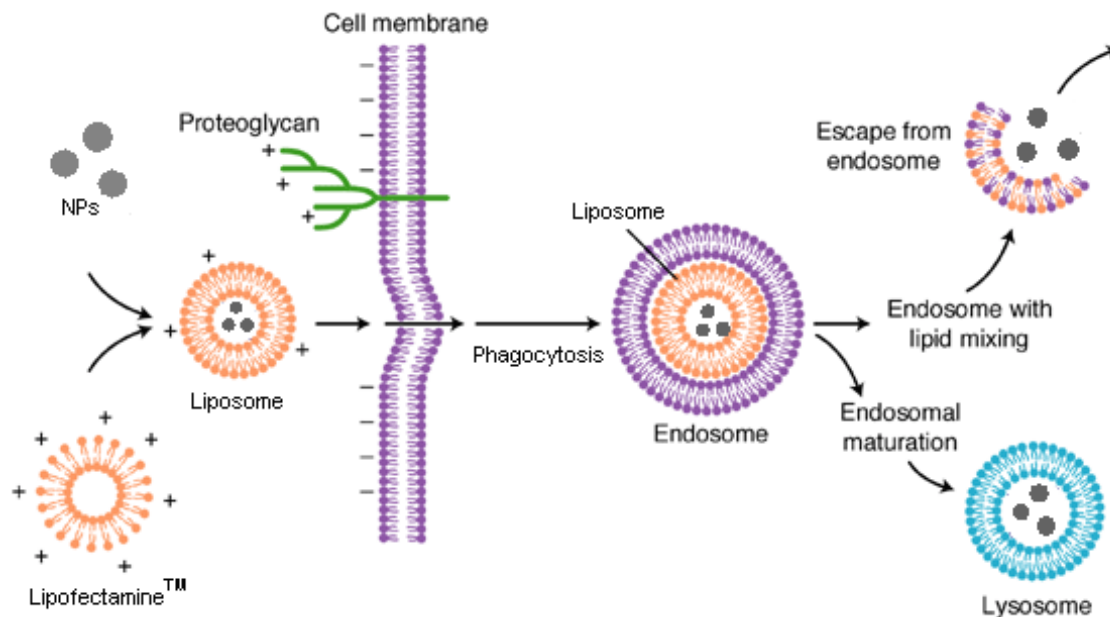


Figure 1.14: Cellular uptake of NPs using the lipofectamine technique. Scheme according to Expert Reviews in Molecular Medicine (Cambridge University Press).

face charge are supposed to interact with the negatively charged membrane of the endosomes leading to a destabilization of the membrane and subsequent escape of the NPs to the cytosol.^{31,32} A drawback of polycationic substances is their tendency to destabilize the cell membrane as well leading to lysis of the cell and cell death. This can be avoided by the use of materials that are only protonated at $\text{pH} \leq 5$ and not at cytosolic pH.

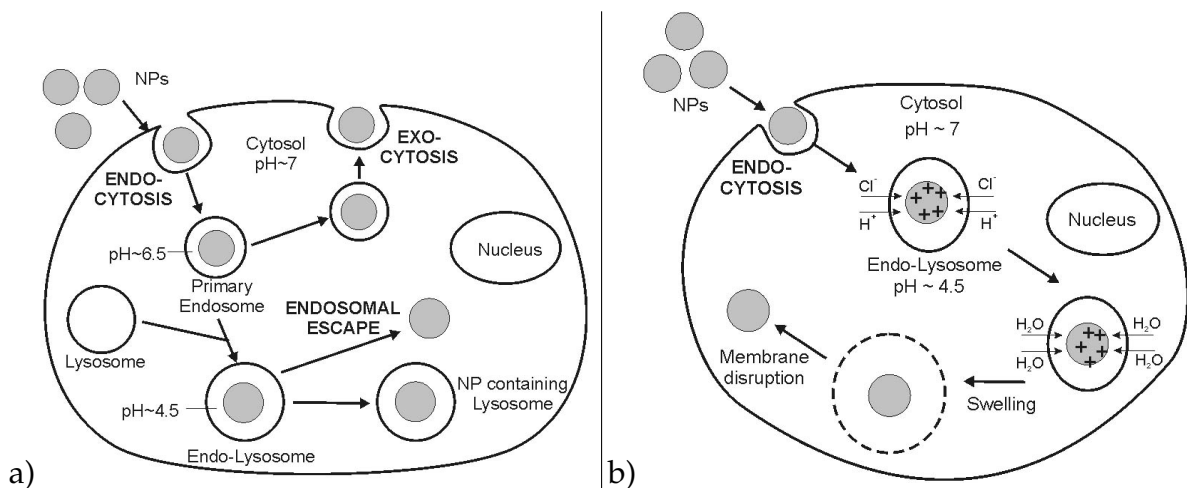


Figure 1.15: Schematic drawing of an eukaryotic cell showing a) the cellular uptake and distribution ways of nanoparticles. Upon attachment to the cell membrane the NPs are unspecifically internalized by endocytosis. The nanoparticle containing vesicles (primary endosomes) either fuse with cellular vesicles (lysosomes) to form endo-lysosomes or fuse with the cell membrane again and release the NPs (exocytosis). The pH inside the vesicles is continuously lowered from pH around 6.5 in the endosomes to 4.5 in the lysosomes. To distribute inside the cytosol the NPs have to escape from the endo-lysosomes otherwise they will be degraded by enzymes inside the lysosomes. Panel b) depicts the endosomal escape of NPs *via* the proton sponge effect.

1.3 Motivation

The most challenging problems of optical chemical sensors for bio-analytics are the signal stability, photobleaching and unspecific reactions with other substances than the analyte. The intensity of the optical output signal not only depends on the analyte concentration, but can also be influenced by the concentration and distribution of the sensor or the intensity of the light source. In case of cells investigated with a fluorescence microscope, the sensor signal can shift due to movement of the observed cell out of the focus of the excitation light beam. Such fluctuations in signal intensity can be reduced by ratiometric measurements. An analyte independent reference signal is mandatory to enable a reliable quantification, especially when using fluorescence microscopy. For ratiometric measurements only the ratio between the signals of the indicator dye and the reference dye is needed to determine the analyte concentration. Thus, signal changes that are due to fluctuations in light source intensity or sensor distribution are eliminated. Embedding the dye chemistry in layers or particles is a fashionable way to enhance the photostability and reduce cross-reactivity. It could be shown that the photostability and the brightness of fluorophores is improved, if they are incorporated inside silica nanoparticles.³³ Furthermore, the bio-sample is protected from possibly toxic dyes and unspecific reactions with the sample are reduced, if the fluorescent dyes are located inside particles.

1.3.1 Important Ionic Analytes

Two ubiquitous and biologically important ionic analytes are chloride ions and protons (pH). Chloride ions can be found nearly everywhere in the environment influencing e.g. corrosion processes and composition of sea water. Furthermore, chloride plays a central role in several physiological processes like cell volume regulation or transport processes. The human physiological concentration range from 2 mM in skeletal muscle, 20-40 mM in epithelial cells to 90 mM in erythrocytes, but can change dramatically in case of diseases such as cystic fibrosis.^{34,35} For example, a high chloride concentration in the sweat is associated with cystic fibrosis and used to establish the diagnosis, since other diseases showing elevated sweat electrolytes

are rare. To understand the underlying pathomechanisms, however, it would be desirable to determine the chloride concentration not only in body fluids but also in the cytosol and intracellular compartments.

The second parameter to be evaluated is the pH with focus on determination in biological samples. The proton concentration e.g. inside a cell or in tissue is tightly regulated, since the activity of most enzymes is highly sensitive to changes in pH. Aberrations from the preset pH caused by mutations in proton-translocating enzymes, disease or by pharmacological means can lead to severe functional changes.^{36,37} The accurate measurement of the proton concentration is the first step to locate and understand the causes behind. Furthermore, pH-sensing can help to identify specific types of tissues or cells. The pH inside a living cell can significantly vary from acidic (pH 4.5 in lysosomes) to neutral conditions (pH 7 in the cytosol). For example cancer cells can be distinguished from healthy cells by their much lower cytosolic pH.

1.3.2 Suitable Indicator and Reference Dyes

The detection of chloride inside cells using (chromo)ionophores was already described by Brasuel *et al.*³⁸ A chloride selective ionophore together with a pH-indicator dye were both embedded inside hydrophobic nanoparticles. The selective extraction of chloride into the nanoparticles leads to a co-extraction of protons causing changes in fluorescence. A limitation of these sensor particles is their size of around 600 nm and their hydrophobicity, which is not compatible with the hydrophilic environment in biological samples and complicates the uptake by the cell (endocytosis). Additionally, ionophores suffer from their cross-sensitivity to pH and the difficult evaluation of the measurement signals. To address the issues of size and bio-compatibility other materials and preparation methods for the nanoparticles (e.g. microemulsion polymerization of acrylamide) need to be employed. To circumvent the drawbacks of ionophores, quinolinium and acridinium-based indicator dyes (**Figure 1.16**) for direct determination of chloride have been introduced.³⁹⁻⁴² The fluorescence of quinolinium and acridinium-based dyes is reversibly quenched by anions such as chloride, bromide, iodide, isothiocyanate and by amines due to a

collisional mechanism.

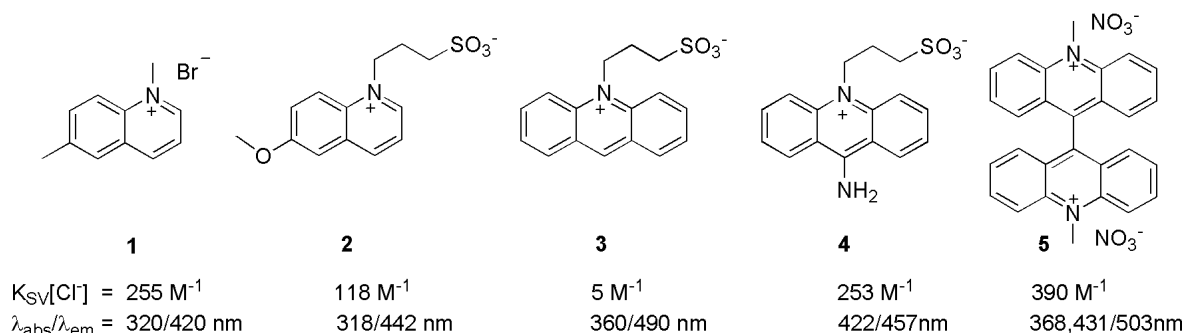


Figure 1.16: Acridinium-based fluorophores for anion sensing. 6-Methyl-*N*-(methyl) quinolinium bromide (**1**), 6-methoxy-*N*-(3-sulfopropyl) quinolinium (**2**), *N*-(3-sulfopropyl) acridinium (**3**), 9-amino-*N*-(3-sulfopropyl) acridinium (**4**), *N,N'*-dimethyl-9,9'-bisacridinium nitrate (**5**, lucigenin).

For the choice of the pH-indicator dye the location where the proton concentration is going to be determined should be considered. An indicator dye with pK_a of around 7 is well suited to measure cytosolic pH, whereas dyes with different pK_a have to be found for more acidic or basic compartments of the cell. The number of fluorescent pH indicators is categorized into their mechanism of sensing:

- (1) pH-sensing due to photoinduced proton transfer, but not electron transfer (e.g. pyranine, hydroxycoumarins),^{43,44}
- (2) fluorophores that show neither photoinduced proton transfer nor electron transfer (e.g. xanthene dyes like fluorescein, seminaphthorhodafluors and seminaphthofluoresceins (SNARF and SNAFL dyes))⁴⁵⁻⁴⁷ and
- (3) pH-sensing due to photoinduced electron transfer (PET) (e.g. naphthalene-1,8-dicarboximide derivatives and anthracene derivatives).^{4,48}

In this work indicators for the neutral pH-range are chosen, because they will be applied at physiological conditions (e.g. inside the cytosol). Some of the above mentioned relevant pH-indicators for the near neutral pH-range are shown in **Figure 1.17**.

For ratiometric measurements a reference fluorophore is needed in addition to the fluorescent indicator dye, unless both the acid and the base form of the indicator

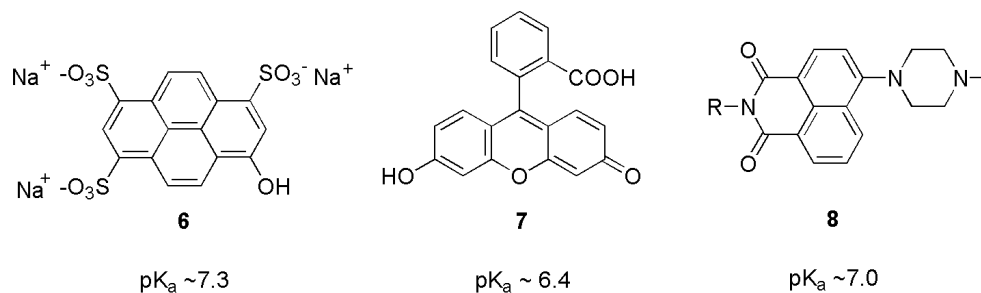


Figure 1.17: Fluorescent pH-indicators for the near neutral range. 8-Hydroxy-1,3,6-pyrene trisulfonic acid (6, HPTS, pyranine), fluorescein (7) and a derivative of 4-(N-methylpiperazinyl) naphthalene-1,8-dicarboximide (8).

show significant emission. The reference should exhibit an analyte independent fluorescence at longer-wavelengths in order to avoid RET from the indicator dye. Rhodamine-based fluorophores are suitable references, since they can be excited at wavelengths above 550 nm, are highly photostable and commercially available.

1.3.3 Immobilization of the Sensor Dyes

For optical sensing in bio-analytics the fluorescent indicator dyes need to be immobilized on solid supports to prevent contamination of the sample. Several attempts have been made to measure intracellular chloride and proton concentrations e.g. using ion-sensitive fiber optics.^{12,49} The drawbacks of optodes are their relatively big dimensions leading to damages of the cell membrane, and the complex experimental setup to measure only one single cell. To overcome these shortcuts fluorescent sensor nanoparticles are well suited, which can be easily and non-invasively transferred into cells. Using a fluorescence microscope time- and spatial resolved analyte monitoring inside many cells simultaneously is achieved. Depending on the material and preparation various types and sizes of particles are obtained. Microparticle sensors like lipobeads (phospholipids coated polystyrene particles)⁵⁰ and polyelectrolyte microcapsules were reported for pH-sensing in murine macrophages and fibroblast cells.⁵¹ Recently, novel core-shell silica nanoparticles were developed incorporating a reference- and sensor dye by covalent bonding in the core-shell architecture.⁵² One further approach is the encapsulation of fluorescent probes by physical

incorporation inside poly(acrylamide) nanoparticles during microemulsion polymerization.^{23,25} The particle preparation is simple and the poly(acrylamide) matrix provides a hydrophilic environment that is mandatory to measure in aqueous samples. The nanosensors can be easily resuspended in water forming a stable colloidal solution and thus can be spectroscopically evaluated. The already discussed drawbacks of physical immobilization (see page 21) are going to be addressed by synthesis of polymerizable dye derivatives and their covalent attachment to the polymer matrix. For intracellular measurements functionalized polymer matrices are needed, which foster on the one hand cellular uptake of the NPs and on the other hand their endosomal escape.

1.4 Aims

The aim of this work is to develop and to characterize fluorescent polymer nanoparticles for sensing of chloride ions and of pH. The focus is on application of the nanosensors in biological media e.g. (living) cells, micro-organisms and tissue. To enable ratiometric analyte determination both an indicator and a reference dye are immobilized inside the particles preferably by covalent attachment. The fluorophores should exhibit high quantum yields to obtain highly fluorescent nanoparticles with little amounts of incorporated dye. The indicator is chosen with respect to good solubility in aqueous media as well as high sensitivity and selectivity to chloride and pH, respectively. The reference dye is supposed to provide an analyte-independent and, in case of chloride sensing, also a pH-independent fluorescence signal. Furthermore, small particle diameters in the range of 20 to 100 nm are desired as well as good monodispersity. The small size of the sensors both enhances the uptake of the particles by cells (with the help of so-called transfection agents) and allows a high loading of the sample under investigation. The obtained nanosensors are intended to enable stable measurements with low cross-reactivity to e.g. ionic strength over a long period of time. Prior to application in real bio-samples the sensor beads are spectroscopically evaluated in aqueous suspension. In case of living cells, the most interesting part to measure analytes is the cytosol. However, after phagocytosis the particles are mostly located inside small cytosolic vesicles called endo-lysosomes. It is known that NPs functionalized with amino groups and a resulting positive surface potential show enhanced endosomal escape. Thus, different methods to functionalize the NPs are carried out and evaluated.

2

Poly(acrylamide) Nanoparticles

2.1 Structural and Physico-chemical Properties

Cross-linked poly(acrylamide) particles in the nanometer range can easily be obtained *via* inverse microemulsion polymerization of the monomers as shown in Figure 2.1.

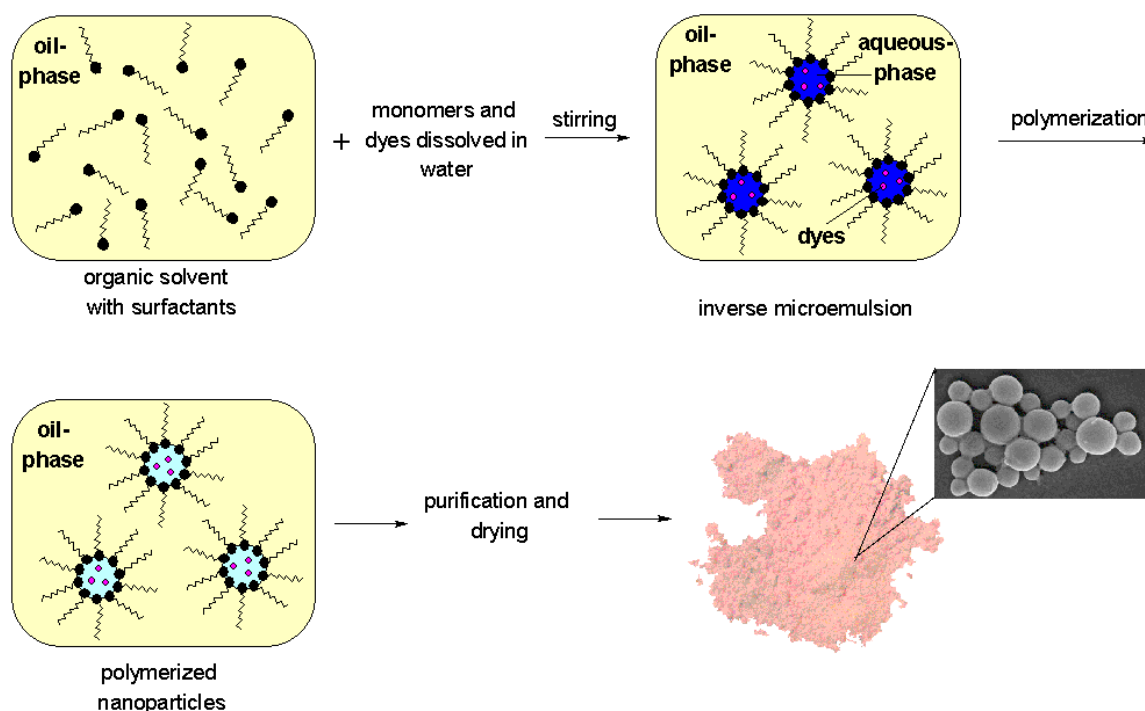


Figure 2.1: Preparation of cross-linked poly(acrylamide) nanoparticles *via* inverse microemulsion polymerization.

Unlike emulsions, microemulsions are optically transparent and kinetically stable due to the use of a co-surfactant. For preparation of a typical inverse microemulsion, the water-soluble monomer acrylamide (AAm) and the crosslinking agent N,N' -methylene bisacrylamide (MBAAm) were dissolved in a small amount of buffer and emulsified with the help of surfactants (AOT, Brij 30) in a non-polar organic solvent (e.g. hexane, heptane). The resulting water-in-oil (w/o) microemulsion consisted of small water droplets dispersed in a continuous organic phase.⁵³ A pseudo-ternary phase diagram shows the composition of a typical polymerization mixture (Figure 2.2).

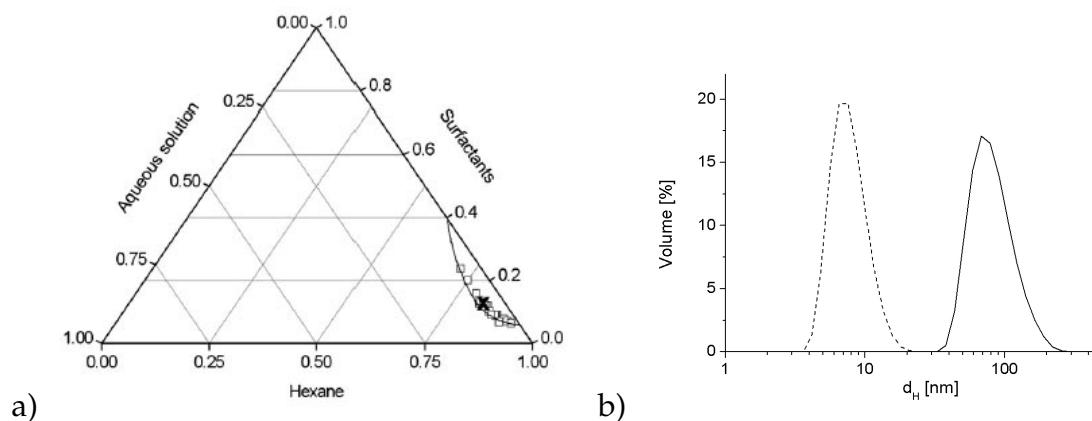


Figure 2.2: a) Pseudo-ternary phase diagram according to Almdal *et al.*⁵⁴ with the experimentally determined area for a one-phase system and the composition of a standard polymerization mixture (x). b) Size distribution graph of two inverse microemulsions with a surfactant-to-water ratio of 4.67 (dashed line) and 2.34 (solid line).

The size of the inverse micelles can be controlled by the surfactant-to-water ratio ($r_{S/W} = m$ (surfactants)/ m (aqueous phase)) of the w/o microemulsion. A surfactant-to-water ratio of 4.67 gave micelles with a mean diameter of approx. 10 nm as determined by dynamic light scattering (DLS). The size of the micelles was in agreement with values reported in the literature.^{53,55} For a typical polymerization approach $r_{S/W}$ was 2.36 and thus close to the maximum solubilization capacity of the surfactants.⁵⁴ Figure 2.2 depicts that the droplet size increased from 10 to 68 nm and the PDI from 0.06 to 0.10, if the surfactant-to-water ratio was reduced to the half.

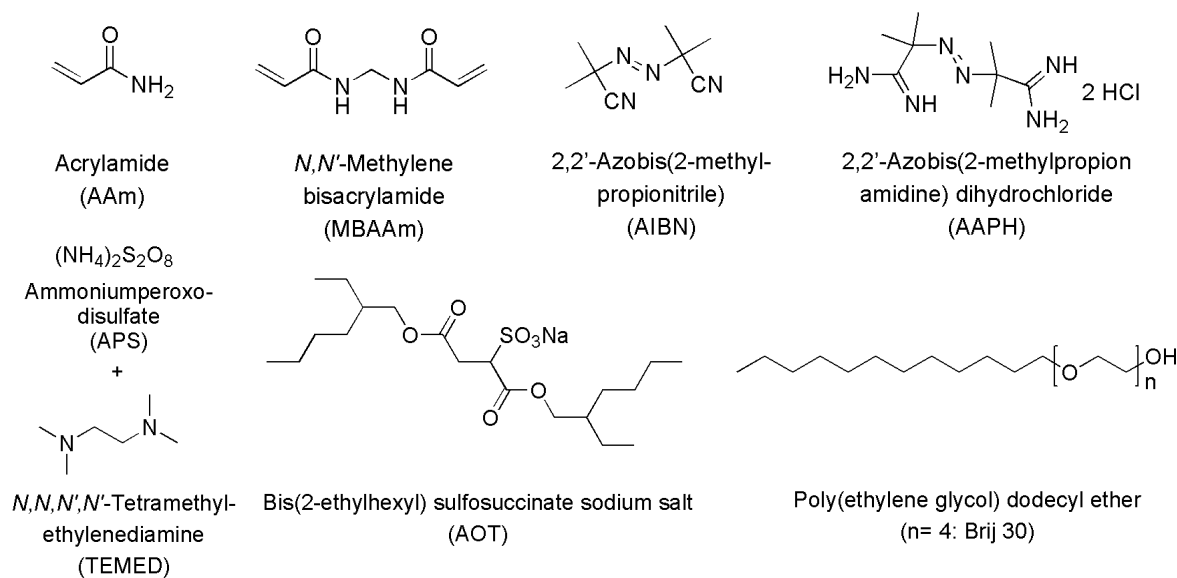


Figure 2.3: Structure of acrylamide, N,N' -methylene bisacrylamide, AIBN, AAPH, APS/TEMED, AOT and Brij 30.

The radicalic polymerization can either be started with hydrophilic (APS/TEMED and AAPH) or hydrophobic initiators (AIBN), respectively (**Figure 2.3**). The polymerization temperature for the redox initiator system APS/TEMED was 25 °C and for the azo-initiators the temperature was raised to 70 °C. Since the w/o microemulsion tended to undergo phase separation at temperatures above 50 °C, a larger $r_{S/W}$ was used in case of the thermal initiation (see **Table 2.1**). By the use of either hydrophilic or lipophilic initiators the location where the polymerization started could be influenced. It was supposed, that in case of the water-soluble initiators, the polymerization was initiated inside the inverse micelles. On the contrary, the hydrophobic initiator AIBN was expected to be mainly dissolved in the organic continuous phase and thus start the polymerization at the interface between the organic phase and the micelles.⁵⁶ Polymerization using APS/TEMED as radical starter gave NPs in yields of 76 - 98%. In case of AIBN the yield of polymeric material was about 90% and for AAPH it was 83 - 99%. **Table 2.1** summarizes the composition of the microemulsions that have been polymerized with three different initiator systems.

After polymerization the NPs were collected by removal of the organic solvent and subsequent precipitation with ethanol. The surfactants and unreacted monomers were removed by extensive washing with ethanol and subsequent ultrafil-

initiator	amount of initiator [%] ^a	oil-phase [wt. - %]	surfactants [wt. - %]	aqueous-phase [wt. - %]	$r_{S/W}$
APS	0.5	81.5	13.0	5.5	2.36
AIBN	2.5	82.7	13.1	4.2	3.12
AAPH	2.5	82.7	13.1	4.2	3.12

^amol-% of the total amount of double bonds in the aqueous phase

Table 2.1: Composition of the w/o microemulsions that were polymerized using three different initiator systems.

tration or centrifugation. Residual ethanol and water were removed by drying *in vacuo*. The NPs were stored in the dry state and resuspended in water using ultrasonification. Upon resuspension of the beads in aqueous media an optically transparent colloidal solution was obtained. In contrast to poly(acrylamide), the NPs were not water-soluble anymore due to their cross-linked macromolecular structure. Furthermore, the NPs can not be dissolved in any common organic solvent as determined by ¹H-NMR-spectroscopy.

2.1.1 Size and Size Distribution

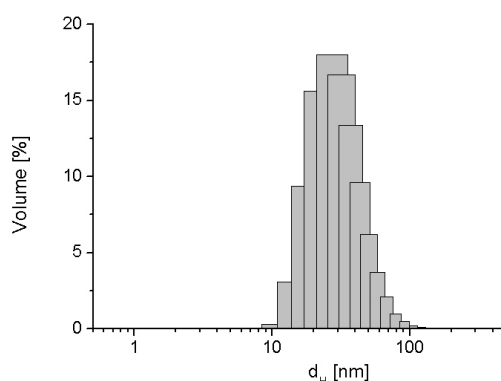


Figure 2.4: Size distribution of NPs prepared under standard conditions.

The hydrodynamic diameter of the aqueous particle suspensions was assessed *via* DLS. The resulting size distribution graph of NPs prepared under standard condi-

tions is shown in **Figure 2.4**. It can be seen that the NPs were homogeneous in size with a mean diameter of *ca.* 30 nm and a narrow size distribution (PDI = 0.16). However, it was observed that a part of the final polymer particles were larger than the micelles in the *w/o*-microemulsion. This might be explained by the fusion of two or more micelles to one larger droplet during the polymerization.⁵⁵ The higher dispersity of the NPs compared to the microemulsion would also support this thesis.

Table 2.2 gives an overview about the size and the polydispersity of poly(acrylamide) NPs obtained from microemulsion polymerization. The size and PDI were observed depending on the variation of different reaction parameters such as the surfactant-to-water ratio, the temperature and the initiator system. The DLS measurements were performed in aqueous buffered suspensions of pH 7.0 as well as in buffers of pH 4.0 and 9.0 in order to exclude pH-induced changes of the particle size.

$r_{S/W}$	T [°C]	initiator	yield [%]	d_H [nm]	PDI
2.36	25	APS/TEMED	78	28	0.16
2.93	25	APS/TEMED	78	24	0.20
3.5	25	APS/TEMED	62	24	0.17
2.36	0	APS/TEMED	68	28	0.17
2.36	60	APS/TEMED	66	33	0.12
3.12	70	AIBN	92	38	0.10
3.12	70	AAPH	99	33	0.18

Table 2.2: Size and polydispersity of the nanoparticles depending on the initiator and pH of the suspension medium. The PDI was obtained from second order cumulant analysis.

The higher surfactant concentration in the microemulsion was supposed to yield a higher number of micelles possessing a smaller diameter. However, it was observed that the influence of $r_{S/W}$ on the nanoparticle size was rather small. The hydrodynamic diameter was just reduced by 4 nm, if $r_{S/W}$ was increased from 2.93 to 3.5.

The higher polymerization temperature of 60 °C slightly increased the hydrodynamic diameter of the particles, whereas a lower temperature neither influenced the

size nor the polydispersity. Therefore, the effect of temperature on the particle size was less than expected from the literature.^{54,55} It was reported that the one-phase area in the pseudo-ternary phase diagram becomes smaller with rising temperature and thus the microemulsion may separate into a two-phase system. The polymerizations using azo-initiators have been carried out at 70 °C. Here, the microemulsion showed beginning phase separation and so the $r_{S/W}$ was raised to 3.12. The obtained particles possessed slightly larger hydrodynamic diameters compared to the polymerization at room temperature. In case of AIBN as the initiator the NPs had a narrower size distribution, which is in agreement with the results obtained from the polymerization at 60 °C.

Figure 2.5 shows a SEM micrograph of NPs polymerized with AAPH. Characterization using electron microscopy had the disadvantage that the NPs could not be imaged in their native wet state. Upon drying larger nanoparticle aggregates with diameters ranging from 100 - 300 nm were predominant. At higher magnification it can be seen that a single particle aggregate consisted of smaller NPs with a mean diameter of 10 nm. It was assumed that the particle aggregates were dissolved during resuspension in buffer by ultrasonification. The NPs with a diameter of 10 nm were then supposed to swell giving the measured hydrodynamic diameter of approx. 30 nm.

2.1.2 Density and Specific Surface

The specific surface of NPs polymerized with different initiators was assessed *via* nitrogen adsorption and evaluated using multipoint BET adsorption isotherms. **Table 2.3** gives an overview about the surface areas and densities determined for the NPs. The specific surfaces varied between 160 and 180 m²/g and the densities were determined to be between 1.4 and 1.7 g/cm³. A correlation between the results and the type of initiator used for polymerization was not observed. Therefore, it can be assumed that the initiator itself and the location where the polymerization was started had no influence on the morphology and density of the particles. From the surface area and the density a theoretical particle diameter can be calculated assum-

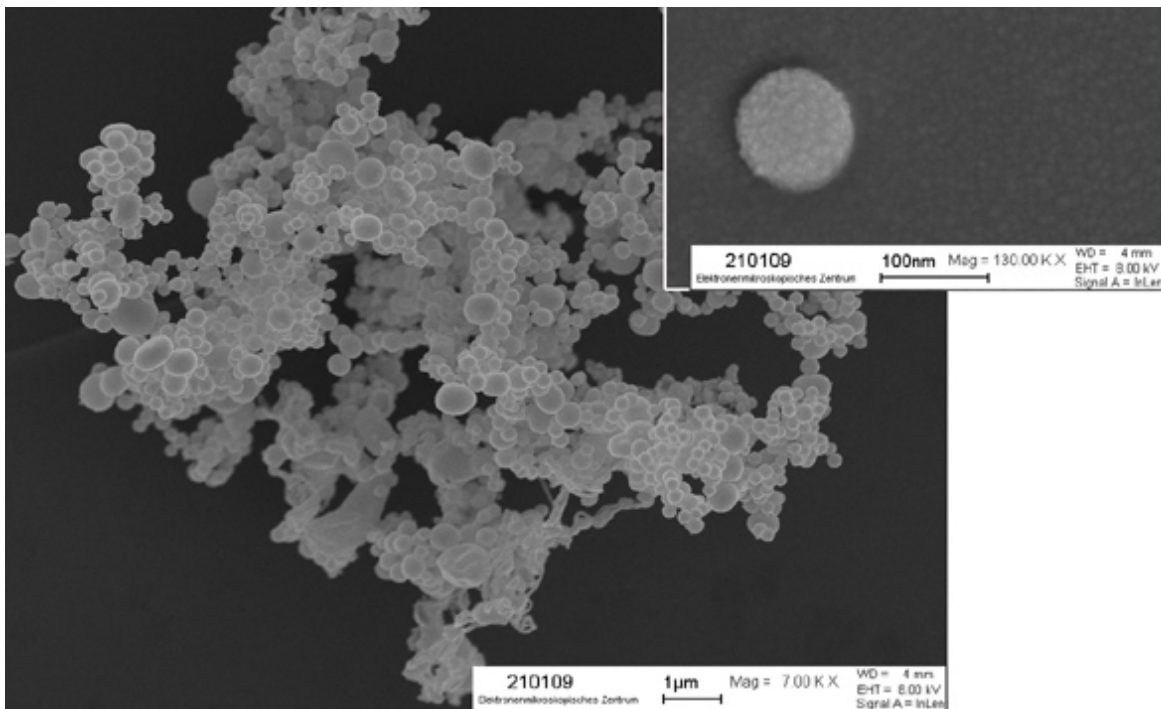


Figure 2.5: SEM micrographs of NPs polymerized with AAPH at 70 °C.

ing a spherical geometry and a smooth surface of the beads:

$$d_{calc} [nm] = \frac{6000}{BET - surface [m^2/g] \cdot \rho [g/cm^3]} \quad (2.1)$$

In general, higher surface areas than the measured ones were expected, due to a certain roughness and porosity of the particle surface. The lower measured specific surface areas can be ascribed to the aggregation of the NPs upon drying. However, the calculated particle diameters for the NPs polymerized with APS/TEMED and AAPH were in the same order of magnitude as the hydrodynamic diameters measured *via* DLS. In case of AIBN the calculated diameter was only half of the hydrodynamic diameter. In other words: the measured BET-surface area was twice as high as the expected specific surface. This can be explained by a rougher surface topology causing an enlarged surface area.

2.1.3 Solid State-NMR Spectroscopy

Since the nanoparticles were not soluble in water or any organic solvent, the conversion of the monomers and the purity of the NPs were determined using ^{13}C -ss-

initiator	BET-surface [m^2/g]	ρ [g/cm^3]	d_{calc} [nm]	d_H [nm]
APS/TEMED	159	1.7	23	28
AIBN	180	1.6	20	38
AAPH	163	1.4	26	33

Table 2.3: Determined BET-surfaces, densities and the resulting theoretical diameters of NPs polymerized using APS/TEMED, AIBN and AAPH, respectively.

NMR. The broadening of the resonance signals was minimized by fast rotation of the sample at an angle of 54.74° relative to the magnetic field during the measurement. This so-called magic angle spinning (MAS) technique gives spectra, which can be compared with common NMR spectra from solutions. The ^{13}C chemical shifts of the monomers (AAm, MBAAm) obtained from NMR in solution and ss-NMR as well as the shifts of the nanoparticles are summarized in **Table 2.4**. Additionally, the ^{13}C -NMR shifts of the dissolved surfactants are given. The data show that the shifts of AAm and MBAAm obtained from NMR of the solutions and ss-NMR are comparable.

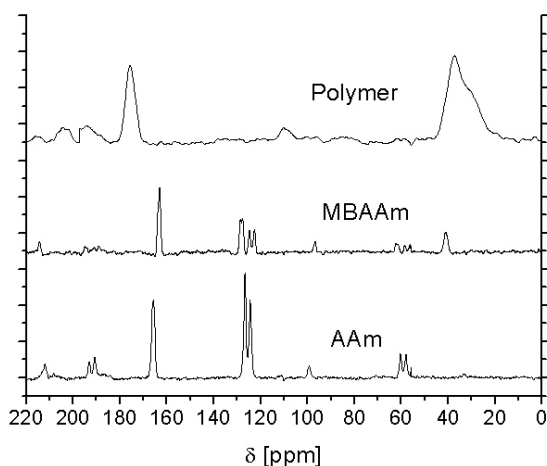


Figure 2.6: MAS- ^{13}C -ss-NMR spectra of the monomer (AAm), the crosslinker (MBAAm) and the polymerized nanoparticles.

In the spectrum of the nanoparticles (**Figure 2.6**) the olefinic ss-NMR shifts of the monomers disappeared and two signals became visible belonging to the carbonyl

and the methylene groups, respectively. From the ss-NMR spectrum it was assumed that the conversion of the monomers during polymerization was higher than 95% (resulting from the detection limit of NMR spectroscopy). Furthermore, possible impurities from residual surfactants (AOT, Brij 30) that were not removed during the washing procedure can be precluded.

	$^{13}\text{C-NMR}$ shifts [ppm]	MAS- $^{13}\text{C-ss-NMR}$ shifts [ppm]
AAm	166.8, 132.4, 126.0	165.8, 126.7, 124.4
MBAAm	166.4, 131.8, 126.4, 43.8	163.1, 128.6, 127.7, 124.8, 122.7, 41.2
NPs	-	175.7, 37.4
AOT	10.7, 14.0, 23.0, 23.4, 28.8, 30.1, 33.0, 38.4, 61.2, 67.5, 68.7, 169.7, 171.6	-
Brij 30	14.1, 22.6, 26.1, 29.3-29.6, 31.9, 61.8, 70.0-70.6, 71.5, 72.5	-

Table 2.4: $^{13}\text{C-NMR}$ shifts of the monomers, the particles and the surfactants. The MAS- $^{13}\text{C-ss-NMR}$ spectra of the monomers and the NPs are given in the appendix on page 115.

2.1.4 Zeta Potential

To some extent the surface charge is supposed to be controlled by the choice of initiator.⁵⁷ Polymerization with APS/TEMED should give negatively charged particles due to the sulfate groups of the initiator, which terminate the ends of the polymer chains. When using the non-ionic initiator AIBN, a neutral polymer is supposed to be afforded. In the same manner, polymerization with AAPH results in terminal amidinium groups at the polymer chains and protonation of the amidinium groups is intended to yield a positively charged polymer. These assumptions could not be verified. All the obtained ζ -potentials for poly(acrylamide) nanoparticles were nearly zero, since poly(acrylamide) is a neutral polymer (**Figure 2.7**). Protonation of the amino group leading to a positive surface potential is expected only at strongly acidic pH (pK_a of AAm in $H_2O = -0.83$). However, the particles have not been applied at such acidic conditions.

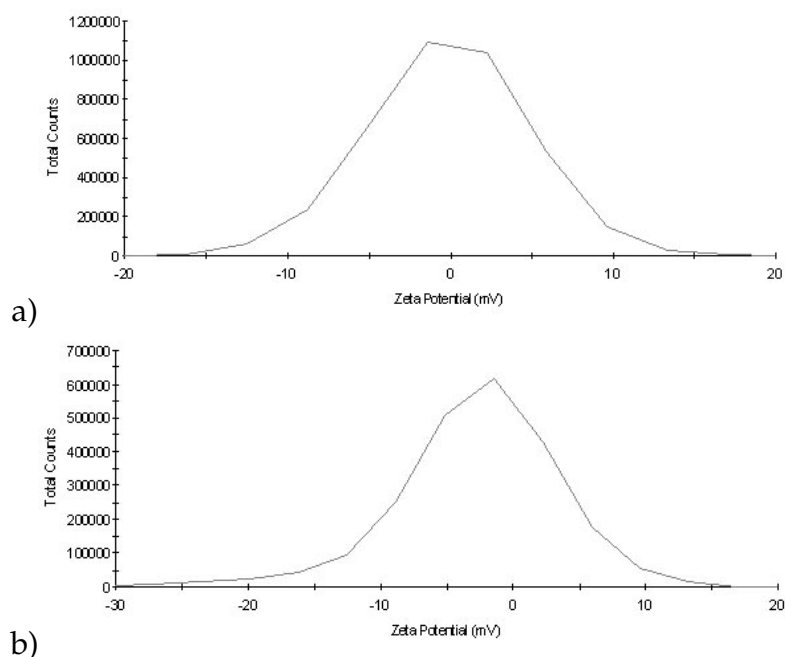


Figure 2.7: Zeta potential of NPs polymerized with a) APS/TEMED and b) AAPH as the initiator.

2.2 Chloride-Sensitive Nanoparticles

To establish new sensor materials for chloride determination in biology and medical research, first an appropriate indicator-reference-dye system had to be found. Three water-soluble acridinium-based fluorophores have been evaluated regarding their spectral properties and response to Cl^- in solution. The structures, the excitation/emission wavelengths and the Stern-Volmer constants for fluorescence quenching of the investigated dyes are shown in **Figure 2.8**. Lucigenin exhibited the most suitable properties to be used for sensing at physiological conditions. It possessed a higher Stern-Volmer constant and excitation/emission maxima at longer wavelengths compared to the dyes possessing only one acridinium unit.

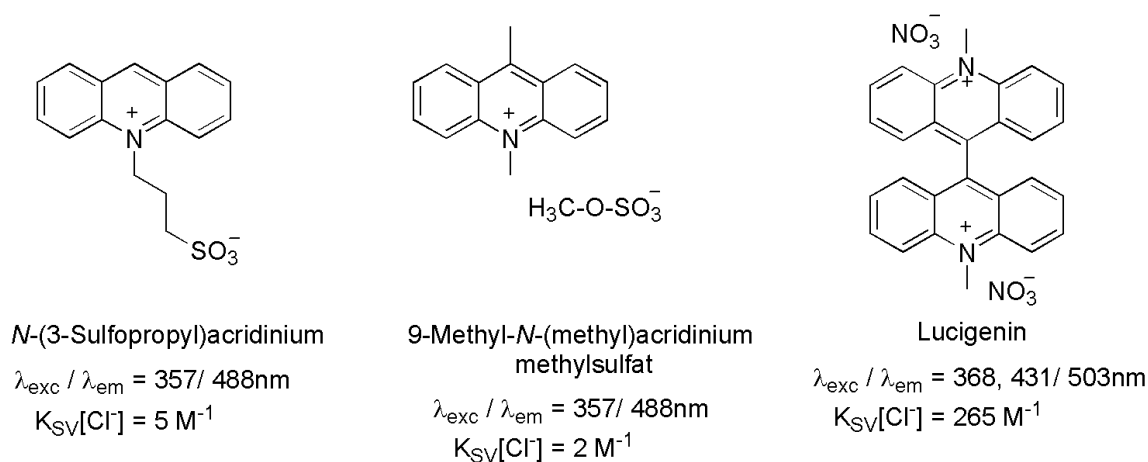


Figure 2.8: Structure, excitation/emission maxima and Stern-Volmer constants of the three investigated chloride-sensitive fluorophores in buffered solution (pH 7.2).

The long-wavelength excitation is important since biological samples show strong autofluorescence when excited with light of wavelengths below 350 nm. Autofluorescence mainly originates from fluorescent amino acids such as tryptophan that can be found in many bio-molecules.³ Therefore, lucigenin, which is excitable at wavelengths higher than 350 nm was preferred over short-wavelengths absorbing dyes. The fluorescence emission wavelength of the indicator dye determined the choice of the analyte-insensitive reference dye, which had to absorb and emit at longer wavelengths. To minimize resonance energy transfer (RET) from the indicator (donor) to the reference fluorophore (acceptor) the overlap between donor

emission and acceptor absorption had to be reduced (see page 13). Rhodamine-based dyes are suitable references, because long-wavelength excitable, pH-insensitive, water-soluble and photostable derivatives are commercially available. Starting from sulforhodamine Q5 acid fluoride a polymerizable derivative was synthesized (**Figure 2.9**), which in the following was used as the reference dye (**R3**).⁵⁸

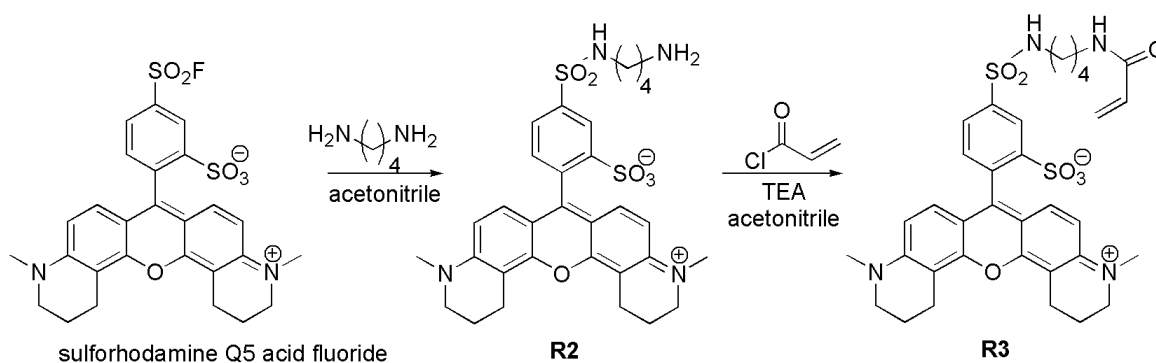


Figure 2.9: Synthesis of the polymerizable reference dye **R3**.

In the next step lucigenin and **R3** were incorporated inside nano-sized polymer beads during inverse microemulsion polymerization. A derivatization of lucigenin to introduce a polymerizable function was not carried out. All attempts to modify simple acridinium dyes in order to introduce a monomer group failed even under harsh reaction conditions. Moreover, a substituent at the aromatic system will probably cause a lower quenching constant. Thus, lucigenin was entrapped inside the particles *via* physical interaction, whereas the reference dye was covalently attached to the polymer backbone.

2.2.1 Structural Properties of the Fluorescent Nanoparticles

The NPs were obtained in 89% yield and showed a bimodal size distribution resulting in a higher PDI of 0.32 compared to the non-dyed NPs (see **Table 2.2**). As depicted in **Figure 2.10 a**) the major part of the beads had a mean hydrodynamic diameter of 24 nm, but a minor fraction of 20% with 200 nm diameter was present as well. **Figure 2.10 b**) shows the SEM micrograph of NPs containing lucigenin and **R3**. As already observed for the non-doped NPs in the dry state, the particles probably formed larger aggregates which were around 200 nm in size. The larger

particle population observed in the DLS could be explained by the presence of such aggregates that have not been completely suspended after ultrasonification. The relatively low specific surface of $48 \text{ m}^2/\text{g}$ determined with the BET-method correlates with a mean diameter of around 100 nm. This underlines the presence of a larger nanoparticle fraction or nanoparticle aggregates also in the dry state. The spectroscopic characterization of both lucigenin and **R3** in solution and when embedded inside poly(acrylamide) nanoparticles is described in the following section.

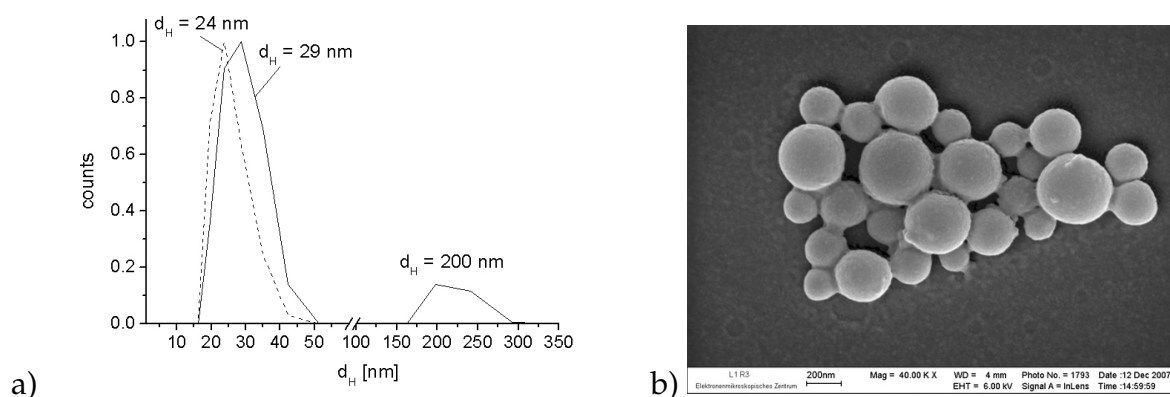


Figure 2.10: a) Size distribution of NPs containing lucigenin and **R3** without weighting (solid line) and with mass-average weighting (dashed line) obtained from DLS. The size and PDI of the particles were determined in aqueous buffered suspension (pH 7.2) using an ALV-NIBS/HPPS and an external ALV-5000/EPP correlator. b) SEM micrograph of NPs doped with lucigenin and **R3**.

2.2.2 Absorption and Fluorescence

The absorption and fluorescence spectra of both dyes in buffered solution are shown in **Figure 2.11** and the spectra of the fluorophores inside the NPs in **Figure 2.12**. Due to the strong scattering of the nanoparticle suspensions it was not possible to receive absorption spectra of the fluorescent nanosensors. Incorporation of the dyes had no significant influence on the excitation and emission wavelengths. In case of the NPs one common wavelength (360 nm) can be used for excitation of both fluorophores. **Table 2.5** summarizes the maxima in absorbance, excitation and emission as well as the quantum yields and extinction coefficients of the dyes.

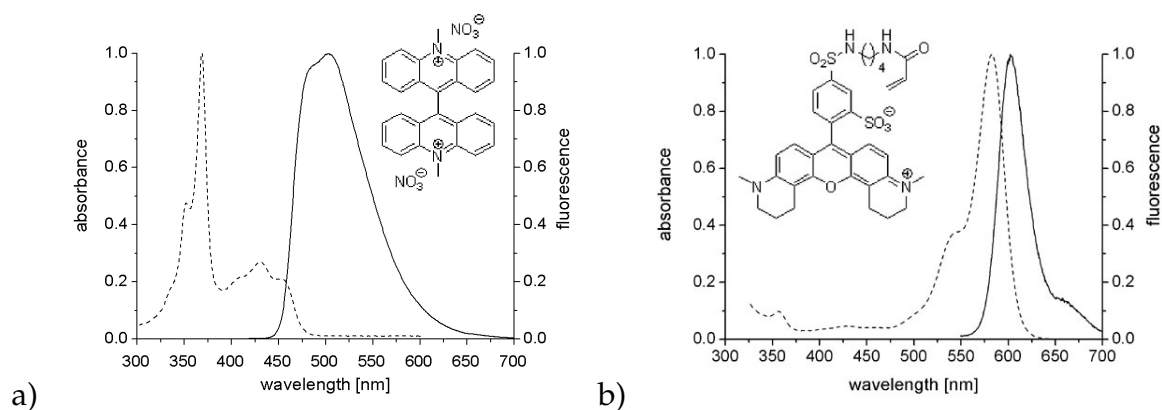


Figure 2.11: Absorption (dashed line) and emission spectra (solid line) of a solution of a) lucigenin (in phosphate buffer pH 7.2) and b) the reference dye **R3** (in MeOH/buffer 1:12, v/v). The dyes were excited at 368 nm and 583 nm, respectively.

	Lucigenin		R3	
	in solution	in NPs	in solution	in NPs
λ_{abs} [nm]	369, 431	-	582	-
λ_{exc} [nm]	368.5, 431	371, 430	582.5	585.5
λ_{em} [nm]	503	507.5	602	605
ϕ	0.37	-	0.35	-
ϵ [$M^{-1}cm^{-1}$]	≈ 32000	-	≈ 40000	-

Table 2.5: Absorption/excitation and emission wavelengths, quantum yields (ϕ) and molar extinction coefficients (ϵ) of the dissolved dyes and when incorporated inside NPs (pH 7.2).

The leaching of the physically entrapped lucigenin and the covalently bound **R3** from the NPs was examined by dialysis of a nanoparticle suspension against phosphate buffer. **Figure 2.13** shows the decrease in fluorescence intensity of both fluorophores during a period of 24 hours. It is remarkable that the fluorescence intensity of lucigenin decreased by 32%, but that of the reference dye only by 11%, clearly demonstrating the importance of covalent attachment. The graph also shows that the major part of lucigenin was washed out during the first hour of dialysis probably due to dye molecules at the surface of the NPs or loosely entrapped dye molecules close to the surface. For this reason, all the following measurements have been performed with nanoparticle suspensions dialyzed for 24 hours.

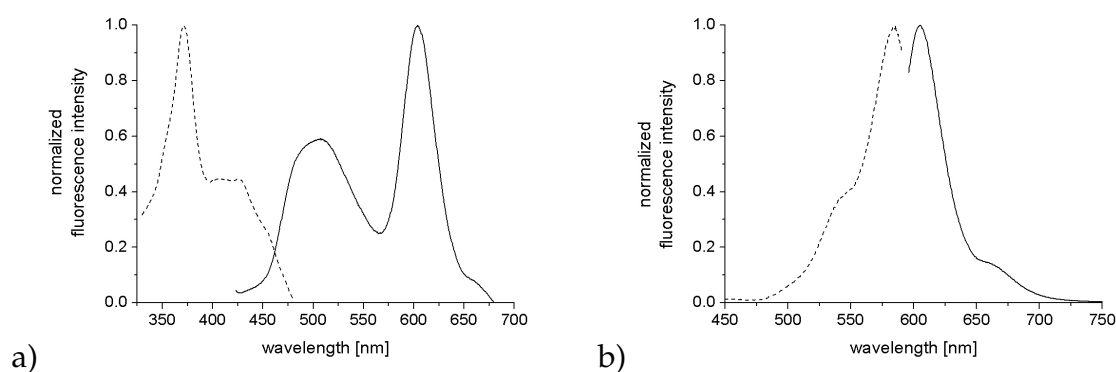


Figure 2.12: Excitation (dashed line) and emission (solid line) spectra of NPs containing lucigenin and **R3**. a) Simultaneous excitation of both fluorophores at a wavelength of 360 nm and b) excitation of **R3** at a wavelength of 584 nm. All spectra were taken in aqueous buffered suspensions of pH 7.2.

2.2.3 Response to Halides and Pseudohalides

The fluorescence quenching of lucigenin by chloride can be described by Stern-Volmer kinetics (see page 10). The fluorescence intensities in presence (F) and in absence of chloride (F_0) were plotted as a function of the chloride concentration $[Cl^-]$ to give the Stern-Volmer constant. **Figure 2.14** shows the response of dissolved lucigenin to increasing concentrations of chloride. The resulting quenching constant K_{SV} was $265 \pm 2 \text{ M}^{-1}$ ($R=0.9996$).

Evaluation of fluorescent NPs with immobilized lucigenin and **R3** gave a smaller quenching constant of $K_{SV} = 53 \pm 1.5 \text{ M}^{-1}$ ($R = 0.9955$) compared to K_{SV} in solution. This might be caused by the hindered access of chloride ions to the dye inside the polymer matrix. In contrast to quenching in solution the quenching of lucigenin inside the NPs is most probably diffusion limited. The higher viscosity of the particle matrix compared to solutions lowers the diffusion coefficient of chloride and therefore the rate of the quenching process. Thus, the Stern-Volmer constant decreases. However, the kinetics of the diffusion was not determined, since the process was too fast to be measured by steady-state fluorescence spectroscopy. Another possibility is that a part of the lucigenin molecules are located deep inside the particle matrix and are not accessible to the analyte at all.

Figure 2.15 shows the resulting K_{SV} constants for quenching of the nanosensors

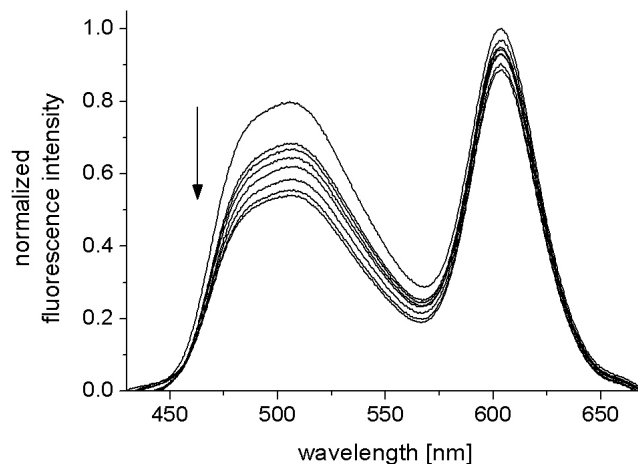


Figure 2.13: Emission spectra of NPs containing lucigenin ($\lambda_{em} \approx 500$ nm) and **R3** ($\lambda_{em} \approx 600$ nm) before and after 60, 120, 180, 1200, 1260, 1380 and 1500 min of dialysis against phosphate buffer of pH 7.2.

by Cl^- and other relevant ions such as Br^- , I^- and SCN^- . As Stern-Volmer fluorescence quenching is a physical process, neither the fluorophore nor the quencher undergo a chemical reaction upon collision with each other. The quenching rates and the resulting Stern-Volmer constants only depend on the radii of both collision partners and the mass of the quenching ion. Since the ion radii of the examined halides and isothiocyanate were in the same order of magnitude, K_{SV} increased with increasing atomic number of the quencher ions (see page 10).

The sensitivity of the NPs was determined by plotting the ratio of fluorescence intensities of lucigenin and **R3** against the concentration of chloride as depicted in **Figure 2.16**. In case of Cl^- as the quenching species the sensitivity was $79.7 \pm 3.5 \text{ M}^{-1}$ ($R = 0.9943$). As expected, the quenching constants and the sensitivities for bromide, isothiocyanate and iodide were higher due to the higher mass of these ions. This, however, does not impede the determination of chloride in biological tissues, since the concentration of these ions is too low to have a significant impact on the quenching of lucigenin.⁴⁹

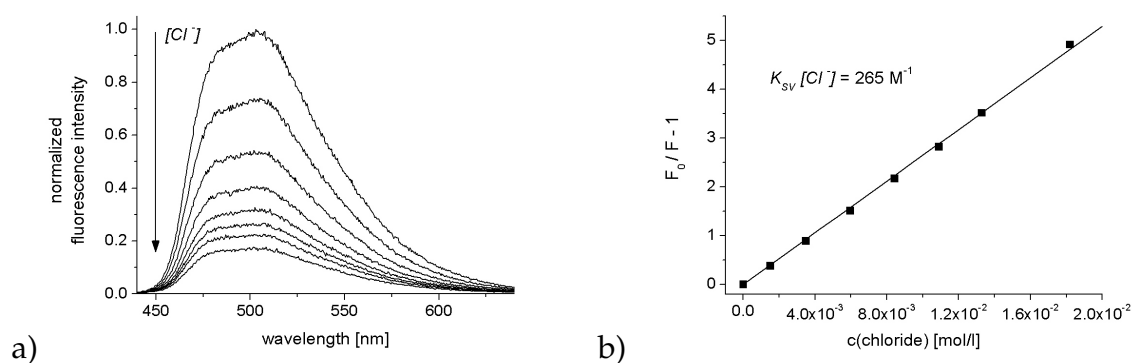


Figure 2.14: a) Emission spectra of lucigenin in phosphate buffered solution of pH 7.2 and b) Stern-Volmer plot for increasing concentrations of 0, 1.5, 3.5, 6, 8.4, 10.9, 13.3 and 18.2 mM KCl.

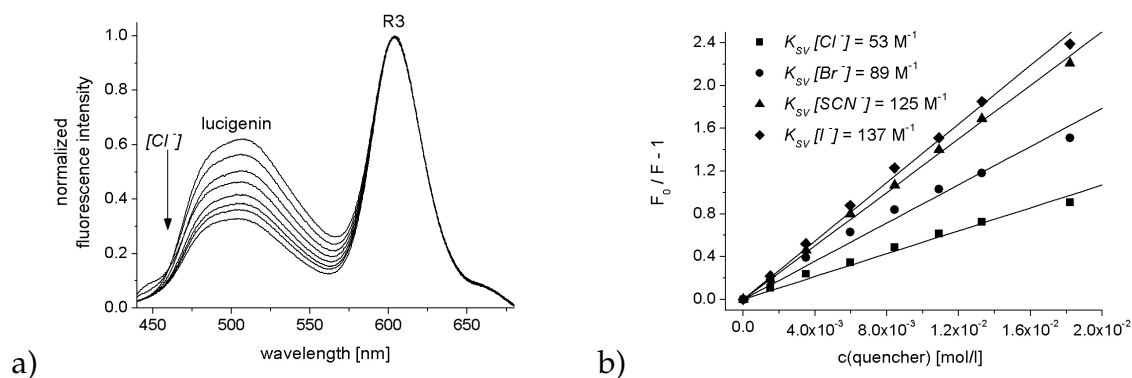


Figure 2.15: a) Emission spectra of NPs in buffered suspension of pH 7.2 and b) Stern-Volmer plot for increasing concentration of 0, 1.5, 3.5, 6, 8.4, 10.9, 13.3 and 18.2 mM KCl, KBr, KSCN and KI, respectively. The excitation wavelength was 360 nm.

2.2.4 Interfering Species

The fluorophores in solution as well as the fluorescent nanoparticles were evaluated with regard to possible interfering species such as sodium hydrogen phosphate, sodium sulfate, pH and proteins. The reference dye **R3** was completely inert to all tested substances except proteins. Hydrogen phosphate, which was used as buffer, had no significant effect on the fluorescence of lucigenin in concentrations ranging from 0 to 22 mM. The same applied to sodium sulfate, which was tested in concentrations ranging from 0 to 14 mM sulfate dissolved in phosphate buffer of pH 7.2.

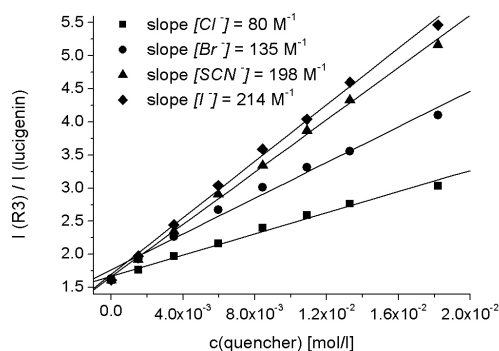


Figure 2.16: Sensitivity of the NPs in suspension for increasing concentrations of 0, 1.5, 3.5, 6, 8.4, 10.9, 13.3 and 18.2 mM KCl, KBr, KSCN and KI. The ratio of fluorescence intensities is $I(R3)_{604nm}/I(lucigenin)_{505nm}$.

pH-Sensitivity

The pH of living tissues can vary during the course of an experiment. This change in pH can also bias the fluorescence signal of lucigenin. In the absence of chloride, the fluorescence of lucigenin in solution decreased by 33%, if the pH of the buffer solution increased from 4.9 to 8.1 (**Figure 2.17 a**). In contrast, the fluorescence did not change significantly, if lucigenin was dissolved in a 12 mM potassium chloride solution, because the quenching constant for Cl^- in solution is higher than that for hydroxyl ions.

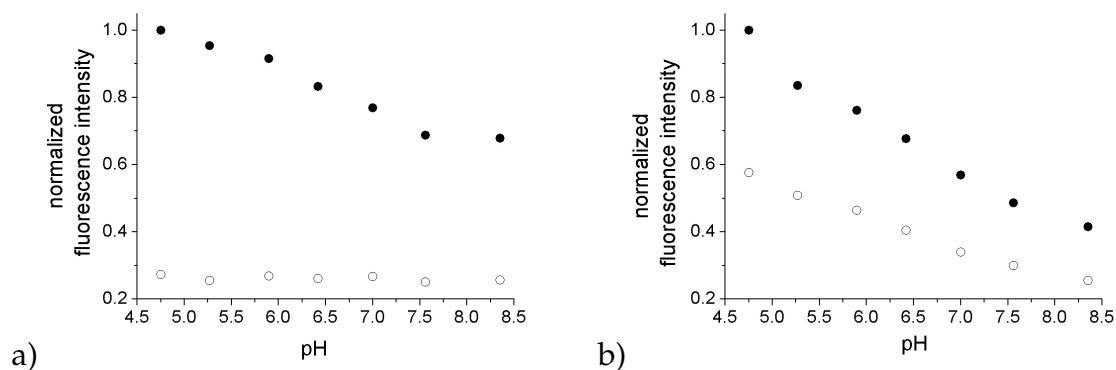


Figure 2.17: Effect of pH on fluorescence of lucigenin. a) Lucigenin in solution and b) lucigenin incorporated in particles. Fluorescence ($\lambda_{exc}/\lambda_{em} = 360/505$ nm) was measured at the indicated pH with potassium chloride concentrations of 0 mM (\bullet) and 12 mM (\circ).

If lucigenin was incorporated into the sensor particles, fluorescence decreased by 58% when pH was varied from 4.9 to 8.1. The quenching of immobilized lucigenin by OH^- can be explained by the fact that hydroxyl ions can easily enter the hydrophilic polymer matrix, due to their small ion radius ($r_{\text{OH}^-} = 120 \text{ pm}$, $r_{\text{Cl}^-} = 181 \text{ pm}$)^a. A smaller radius of the quencher ions affords a higher diffusion coefficient ($D_{\text{OH}^-} = 5.3 \cdot 10^{-9} \text{ m}^2\text{s}^{-1}$, $D_{\text{Cl}^-} = 2 \cdot 10^{-9} \text{ m}^2\text{s}^{-1}$)^b, according to the Stokes-Einstein equation:

$$D = \frac{kT}{6\pi\eta} \left(\frac{1}{R_M} + \frac{1}{R_Q} \right) \quad (2.2)$$

D is the diffusion coefficient, k the Boltzmann's constant, η the viscosity of the solvent and R_M and R_Q are the radii of the fluorophore and the quencher, respectively (see also page 14). Additionally, OH^- ions possess a higher ion mobility caused by the transport mechanism (Grotthuss mechanism), which is much faster compared to the diffusion of other ions.

When the pH was increased in presence of Cl^- , the fluorescence intensity of the NPs decreased, like in absence of Cl^- , by $\sim 50\%$ (see **Figure 2.17 b**). In other words, the quenching constant for OH^- is equal to that for Cl^- or even higher, if lucigenin is incorporated into the polymer matrix. This is the opposite behavior to the quenching of lucigenin in solution. As already mentioned, the OH^- ions exhibit a higher diffusion coefficient compared to Cl^- ions and a much higher ion mobility. Therefore, the diffusion coefficient of OH^- within the polymer matrix is also higher resulting in a higher quenching constant. Consequently, quenching by hydroxyl ions in the polymer matrix is almost not diminished and dominates over the reduced quenching of chloride, whereas in solution quenching by chloride is by far more effective.

Interaction with Proteins

Representative for the number of proteins that are present inside cells or tissues, bovine serum albumine (BSA) was utilized to evaluate the interaction between fluorophores and proteins. The spectral properties of fluorescent dyes can change by

^a data from J. Huheey, E. Keiter, R. Keiter *Anorganische Chemie* Walter de Gruyter Berlin 1995

^b data from P. W. Atkins *Physikalische Chemie* Wiley-VCH Weinheim 2001

the presence of proteins e.g. due to formation of aggregates with dyes.²⁷ This interaction can seriously affect measurements with ion indicators in biological tissues where proteins are omnipresent. **Figure 2.18** shows that fluorescence of plain lucigenin and **R3** was considerably quenched by BSA. In particular the fluorescence intensity of lucigenin decreased by 70% at a BSA concentration of 5 wt.-%. As already mentioned the influence of the polymer matrix on the behavior of the incorporated dyes was going to be assessed. For this purpose, the same amount of BSA was added to a nanoparticle suspension. In this case the fluorescence intensity of the protected dyes decreased only slightly. The strong absorption of BSA at 300 - 350 nm and scattering of the emitted fluorescence by BSA contribute to this decrease. Thus, the dyes might be even better shielded by the polymer matrix than it appears from this plot.

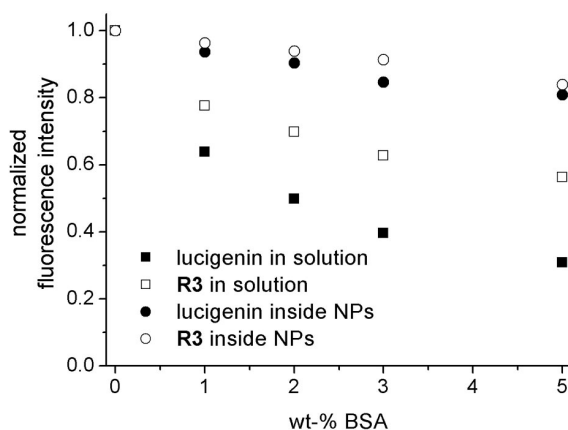


Figure 2.18: Effect of BSA on fluorescence of lucigenin and **R3** in solution and when incorporated into particles. The fluorescence of the solutions and suspensions was excited at a wavelength of 430 nm, to avoid autofluorescence of BSA and the emission was measured at 505 nm (lucigenin) and 604 nm (**R3**), respectively. All measurements were performed in phosphate buffer (pH 7.2).

2.2.5 Oxidation of the Fluorophores

Certain enzymes and substances inside biological fluids are known to catalyze oxidation processes (e.g. monooxygenases) and acridinium-based dyes can be oxidized

to their acridone derivatives (**Figure 2.19 a**).^{59,60} The fluorescence emission spectra of acridones are blue-shifted to approx. 430 nm so that the characteristic emission of lucigenin at 500 nm disappears upon decomposition. In contrast to acridinium dyes, acridones show no fluorescence quenching in presence of halide ions. Thus, lucigenin was investigated towards oxidation by hydrogen peroxide in solution and when protected by the polymer matrix of the particles. The fluorescence intensity of lucigenin in solution decreased about 34% and inside the particles about 28% upon exposure to as high as 110 mM hydrogen peroxide. At lower hydrogen peroxide concentration no difference in the stability against oxidation was observed (see **Figure 2.19 b**). From these data it can be assumed that the poly(acrylamide) matrix does not shield against the entrance of small molecules such as hydrogenperoxide into the NPs.

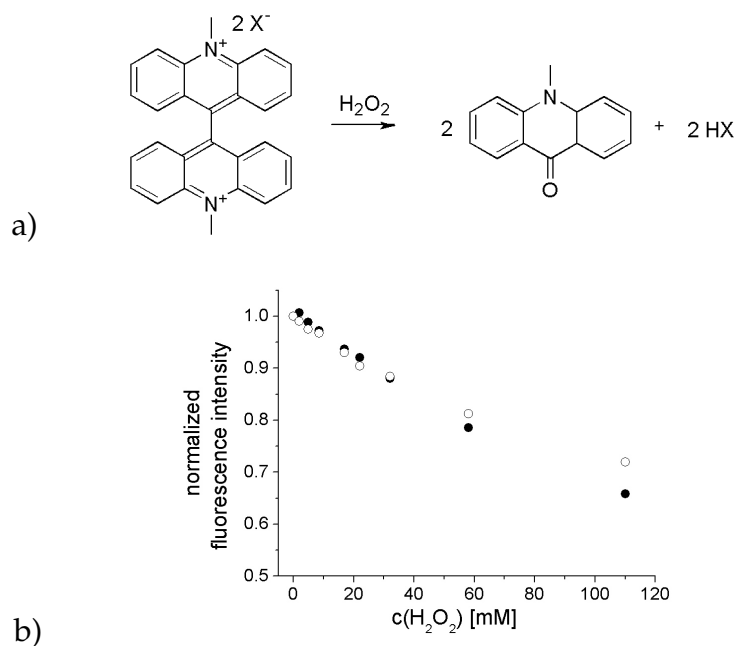


Figure 2.19: a) Oxidation of lucigenin to *N*-methyl acridone by hydrogenperoxide. b) Decrease of the fluorescence intensity of dissolved (●) and incorporated (○) lucigenin at 505 nm upon decomposition by hydrogen peroxide.

2.2.6 Application of the NPs inside Living Cells

In cooperation with the Institute of Physiology II at the University Jena the nanosensors were tested in living cells. They have been incorporated into chinese hamster

ovary (CHO) cells and mouse fibroblasts using the conventional lipofectamine technique. By addition of the liposome-nanosensor solution to the cell culture, a large number of cells was efficiently loaded with the nanosensors. In **Figure 2.20** a confocal cross section of CHO cells incubated with the nanosensors is shown. It appears that the nanosensors were located in the cytoplasm leaving the nucleus blank. Furthermore, the intensity profile along the line in panel c) shows that both dyes were equally distributed in the cytoplasm.

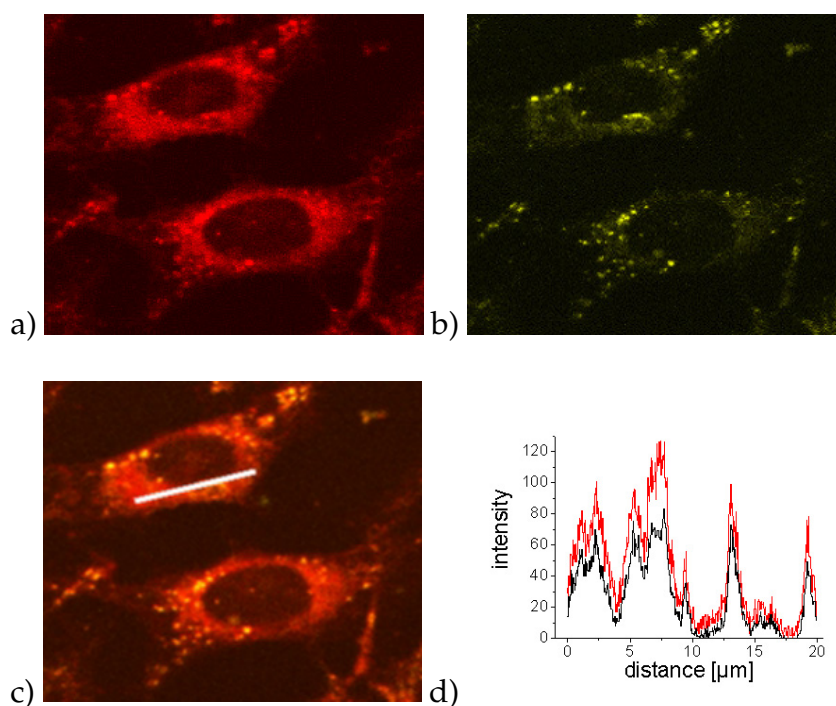


Figure 2.20: Confocal micrographs of CHO cells incubated with nanosensors. a) fluorescence of the reference dye **R3**, b) fluorescence of lucigenin, c) overlap of fluorescence of both dyes, d) intensity profile of both dyes along the line indicated in panel c).

To assess the response of the nanoparticles in living cells, the loaded cells were subsequently superfused with phosphate buffered solutions of pH 7.4 containing 10 mM and 50 mM chloride. Intracellular $[Cl^-]$ was set equal to extracellular $[Cl^-]$ by using tributyltin(IV)chloride and the ionophore nigericin. Tributyltin(IV)chloride acts as a Cl^-/OH^- antiporter, which exchanges Cl^- for OH^- ions.²⁷ To prevent a shift of the intracellular pH, which would have been invariably caused by the Cl^-/OH^- exchange, the K^+/H^+ antiporter nigericin was added, which clamped the intracellular pH to the extracellular pH. **Figure 2.21** shows the time course of

the lucigenin and **R3** fluorescence during such an experiment. In this experiment the cell shifted only slightly so that the reference signal was almost constant. As expected, lucigenin fluorescence decreased at higher Cl^- concentrations and reached the original value after an exchange of the superfusing solution to the initial Cl^- concentration. However, for this type of experiment special care must be taken to prevent phototoxic damage of the cells. Images had to be acquired at a high scan speed ($2.6 \mu\text{s}/\text{pixel}$, $1.6 \text{ s}/\text{image}$) and a low repetition rate (1 image/min). If light exposure was increased, cells were damaged and membrane blebs could be observed.

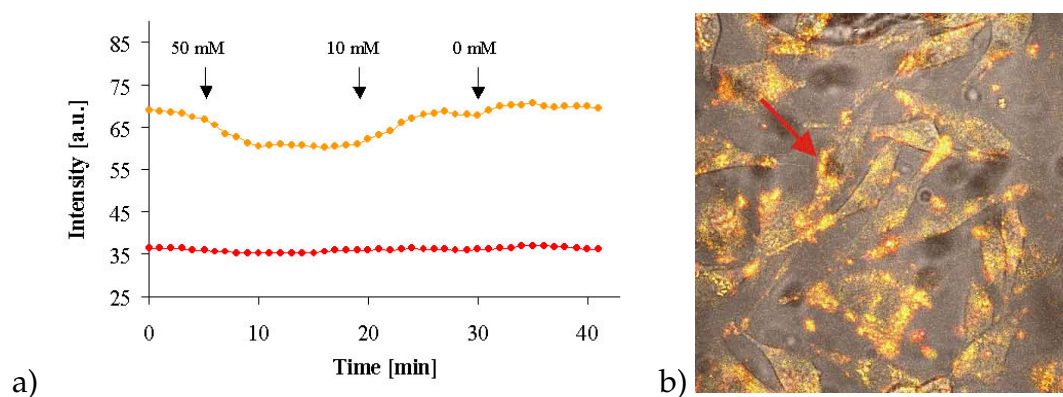


Figure 2.21: Intracellular chloride calibration. a) Time course of lucigenin (orange circles) and rhodamine (red circles) fluorescence in the cytoplasm of the cell marked in panel b) during superfusion with phosphate buffers (pH 7.4) containing chloride in the indicated concentrations. b) Overlay of the transmission and lucigenin and rhodamine fluorescence images obtained from mouse fibroblasts incubated with the ratiometric nanosensors. Cells were permeabilized with tributyltin(IV)chloride and nigericin.

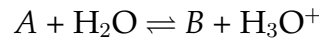
2.3 pH-Sensitive Nanoparticles

2.3.1 pH-Sensing using Fluorescent Indicators

A glass electrode linearly responds to the activity of protons (a_{H^+}) in a solution from which the pH can be determined:

$$U(\text{glass}, H^+; 25^\circ C) = \text{const.} - \frac{RT}{F} \ln a_{H^+} = \text{const.} + 0.059V \cdot pH \quad (2.3)$$

U is the measured voltage between the glass electrode and the solution, R is the gas constant, T the absolute temperature and F the Faraday constant. In contrast, pH-sensing using indicator dyes is based on the optical determination of the acidic $[A]$ and basic form $[B]$ of the indicator. Dissociation of the acidic form of the indicator into the basic form is described as follows:



The dissociation constant of the acid-base equilibrium is:

$$K = \frac{a_B \cdot a_{H_3O^+}}{a_A \cdot a_{H_2O}} \quad (2.4)$$

For low concentrations of the indicator dye it can be assumed that its activity is equal to the concentration and the Henderson-Hasselbalch equation is obtained:

$$pH = pK_a - \log \frac{[A]}{[B]} \quad (2.5)$$

The degree of the dissociation α is the ratio between the concentration of the basic form to the overall indicator concentration. The concentrations of $[B]$ and $[A]$ are obtained from the fluorescence intensities:

$$\alpha = \frac{[B]}{[B] + [A]} = \frac{(S_x - S_A)}{(S_B - S_A)} \quad (2.6)$$

S_x is the fluorescence intensity at a given wavelength and S_A and S_B are the fluorescence intensities of the acidic and basic form of the indicator. Combination with the Henderson-Hasselbalch equation gives the following relation that allows the determination of the pK_a from the measured fluorescence intensities:

$$pH = pK_a - \log \frac{(S_B - S_x)}{(S_x - S_A)} \quad (2.7)$$

The plot of the fluorescence signal S_x versus the pH gives a sigmoidal fit function and the inflection point of this graph is the pK_a of the indicator dye.

$$S_x = \frac{S_B + S_A \cdot 10^{(pK_a - pH)}}{10^{(pK_a - pH)} + 1} = S_A + \frac{S_B - S_A}{10^{(pK_a - pH)} + 1} \quad (2.8)$$

Equation 2.8 is based on the simplifications that the concentrations of A and B are equal to the activities and that the fluorescence intensity directly corresponds to the concentration of the dye. Thus, the determined acidity constant not only depends on the temperature, but also on other factors affecting the activity coefficients (e.g. ionic strength) and on the microenvironment of the dye. Considering the aberrations from ideal behavior, the determined pK_a values are always apparent values. An effect of the deviation between “true” and apparent pK_a is that the sigmoidal titration plots exhibit a smaller slope (i.e. they show a wider dynamic range). The smaller slope causes that the calibration function (eq. 2.8) gives only insufficient description of the experimental data. Therefore, all pK_a values have been determined using the sigmoidal fit function of the data analysis software OriginPro 7.0 (ORIGINLABS). The fit is based on the Boltzmann model and uses an exponential function with an additional correction factor dx that determines the slope of the sigmoid:

$$S_x = \frac{S_A + S_B \cdot e^{(pH - pK_a)/dx}}{e^{(pH - pK_a)/dx} + 1} = S_B + \frac{S_A - S_B}{e^{(pH - pK_a)/dx} + 1} \quad (2.9)$$

The application of optical pH-sensors is limited to the dynamic range of the sigmoidal calibration plot, because only there accurate pH measurements are possible. Usually the dynamic range of an indicator dye in solution is in the interval of $pK_a \pm 1.5$. The most challenging task for the development of novel pH-indicators is to achieve a broad dynamic range and hence a wider field of application. In this work the dynamic range of the indicators have been determined according to Wolfbeis *et al.*⁶¹ The pH-range in which 90% of the total signal change occurs is considered as the dynamic range.

Four different indicator dyes appeared to be suitable for measuring in the neutral pH-range: HPTS, a fluorescein derivative (**F2**) and the naphthalimide-based fluorophores **N1** and **N2** shown in **Figure 2.22**. All pH-indicator dyes were evaluated regarding their fluorescence and sensing properties in solution. Additionally,

they were incorporated together with a reference dye inside cross-linked poly(acrylamide) NPs. The results of the measurements are summarized in **Table 2.6**. The chosen pH-indicators possess excitation wavelengths over 350 nm, which was mandatory for intracellular applications. From the data in **Table 2.6** it can be seen that each fluorophore had both advantages and shortcomings.

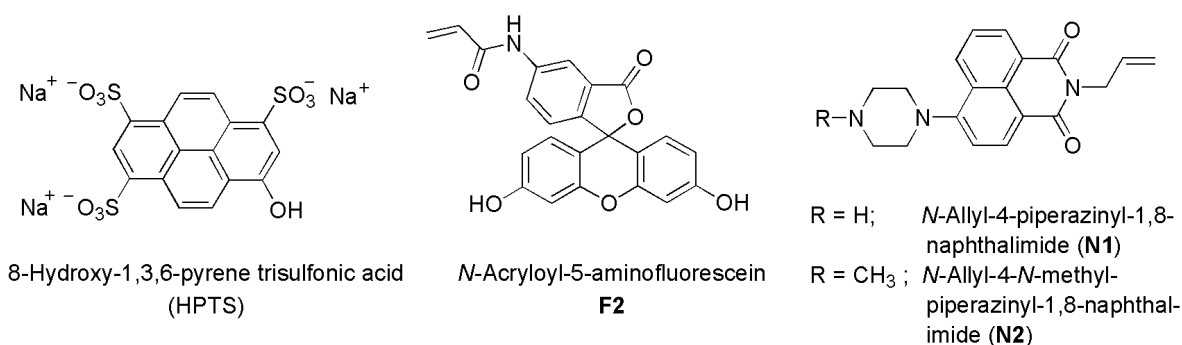


Figure 2.22: Structure of the investigated pH-indicator dyes HPTS, F2, N1 and N2.

In particular, HPTS (**Figure 2.23**) seemed to be the least favorable dye. Despite its high photostability and large Stoke's shift, HPTS is known to show strong cross-sensitivity to ionic strength. Furthermore, a derivative possessing a polymerizable group was synthetically not accessible. Attempts to introduce an acrylate group *via* the reaction of dihydroxypyrene disulfonic acid with acryloyl chloride or methacrylic acid anhydride according to Kermis *et al.*⁴³ were not successful. Thus, HPTS was physically immobilized inside the sensor particles, which led to significant leaching.

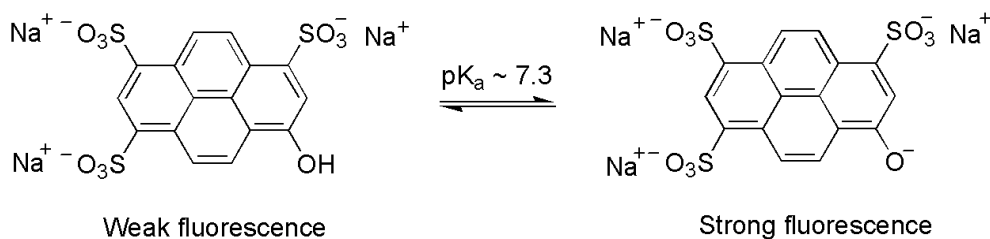


Figure 2.23: Structure and fluorescence of the acidic and basic form of HPTS.

The polymerizable fluorescein derivative (**F2**) was easily accessible *via* reaction of the commercially available 5-aminofluorescein with acryloyl chloride (**Figure 2.24**).⁶²

Fluorophore	λ_{exc} [nm]	λ_{em} [nm]	Stoke's shift [nm]	pK_a	dynamic range [pH units]
HPTS	404 (pH 5) 454 (pH 8)	515	61 - 111	7.35	6.4 - 8.2
HPTS in NPs	404, 454	510	56 - 106	7.51	6.5 - 8.0
F2	490	513	23	6.48	5.4 - 7.6
F2 in NPs	459, 476 (pH 5) 497 (pH 8)	520	23	6.62	5.6 - 7.6
N1	387	532	145	6.43	5.3 - 7.5
N1 in NPs	398 (pH 5) 410 (pH 8)	519 (pH 5) 511 (pH 8)	121 101	6.15	5.3 - 7.1
N2	383	529	146	6.15	4.6 - 8
N2 in NPs	387 (pH 5) 376 (pH 8)	523 (pH 5) 521 (pH 8)	136 145	6.73	5.0 - 8.2

Table 2.6: Spectral properties and pH response of the investigated indicator dyes in solution and when incorporated inside poly(acrylamide) NPs.

The functionalized fluorophore was evaluated in solution and after covalent immobilization into nanoparticles. The maximum excitation wavelength of the dye is 490 nm, which is advantageous for fluorescence microscopy of cells and other biological samples. The Ar⁺-laser line, which is commonly used as excitation light source has a wavelength of 488 nm and thus is fully compatible with the excitation maximum of fluoresceins. This is the reason why fluorescein dyes are frequently used as optical probes in fluorescence microscopy despite their known shortcomings such as low photostability.⁶³ Typically for fluoresceins the pH-indicator **F2** exhibited only a small Stoke's shift and an acidic pK_a , which is less favorable for applications in the e.g. cytosol where the pH is around 7.4.

Naphthalimide-based fluorophores are known to show enhanced photostability and larger Stoke's shifts compared to fluoresceins. In contrast to highly ionic dyes such as HPTS naphthalimides are supposed to be less sensitive to influences of ionic

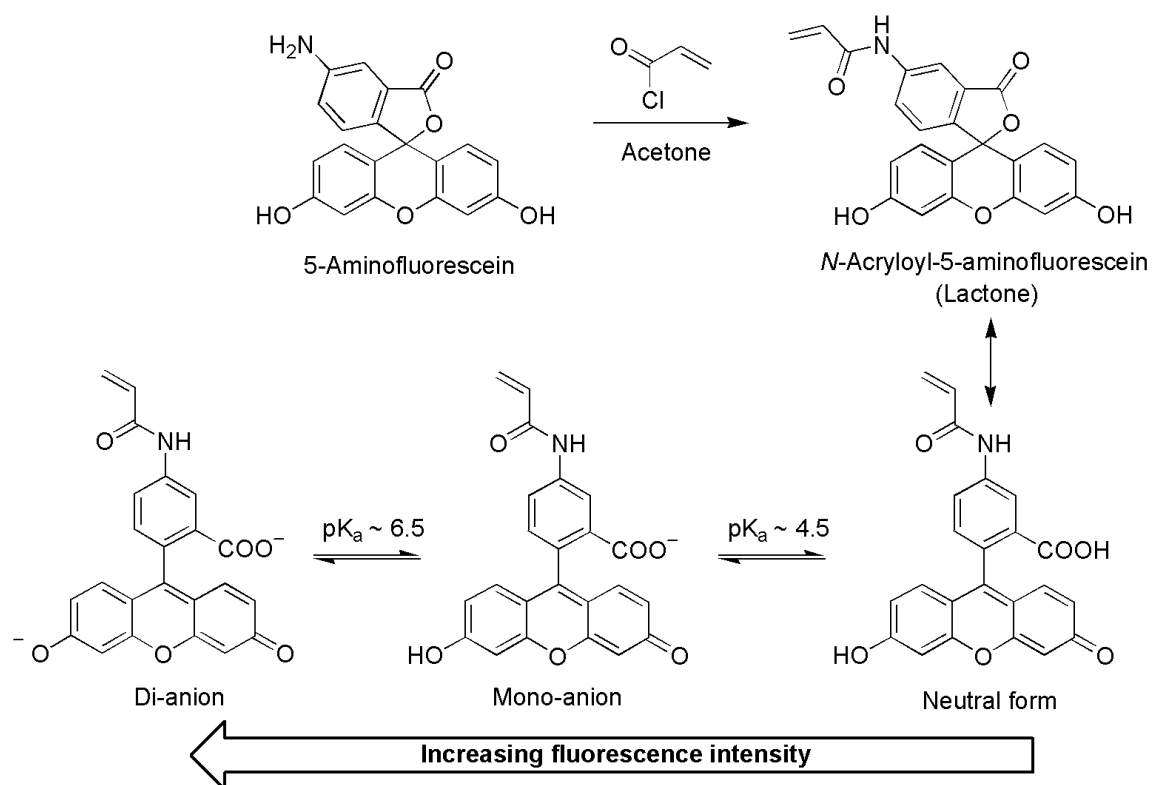


Figure 2.24: Synthesis of the polymerizable fluorescein derivative **F2** and structure of the corresponding di-anion, mono-anion and neutral form.

strength.^{64,65} Furthermore, the dyes exhibit a strong increase in fluorescence intensity upon presence of the analyte. The facile synthesis of various amino-substituted naphthalimides offers the opportunity to develop tailor-made pH-indicators.⁶⁶ The syntheses of the polymerizable pH-indicator dyes **N1** and **N2** are shown in **Figure 2.25**.^{64,67} The pK_a of the indicators was tailored *via* modification of the substituent at the aliphatic amino group. Upon incorporation of the fluorophores inside the NPs it appeared that a methyl substituent afforded a broader dynamic range and a larger Stoke's shift compared to **N1** as well as a pK_a close to 7. Due to these facts the methylpiperazine derivative of the naphthalimide fluorophore (**N2**) was chosen as the pH-indicator for all further experiments. In contrast to the chloride nanosensors, it was possible to covalently attach both the pH-indicator dye and the reference dye **R3** to the particle backbone.

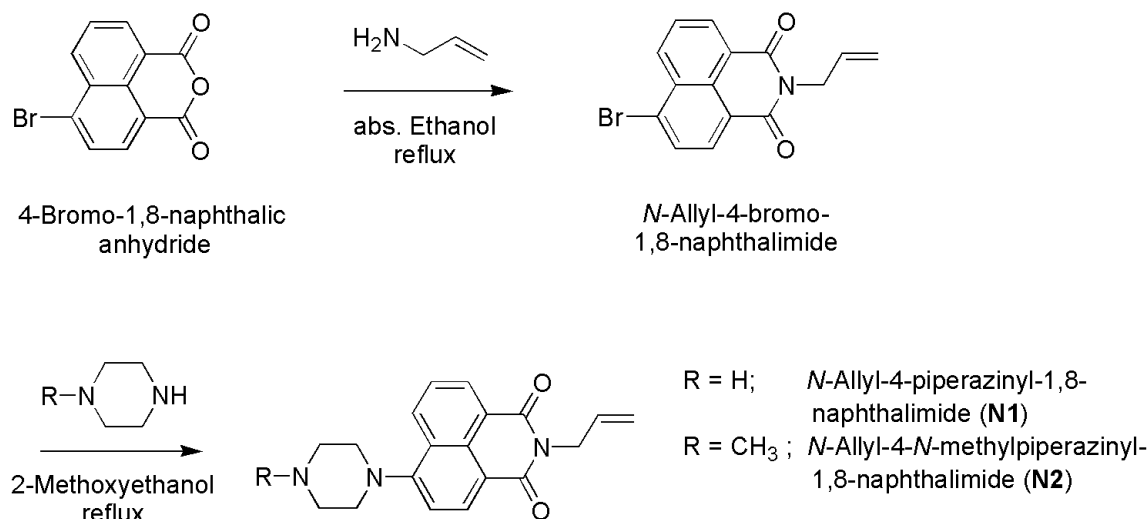


Figure 2.25: Synthesis of the polymerizable pH-indicator dyes **N1** and **N2**.

2.3.2 Influence of Dye Immobilization

The influence of dye immobilization on the yield of the microemulsion polymerization and on the size and specific surface of the final NPs was evaluated. For that purpose NPs with the covalently attached fluorophores **N2** and **R3** have been prepared using APS/TEMED, AIBN or AAPH as the initiator system. The obtained particles have been characterized and the results were compared to the above mentioned dye-free particles (see page 35).

NPs	initiator	yield [%]	d_H [nm]	PDI	ρ [g/cm ³]	BET-surface [m ² /g]
dye-free	APS/TEMED	78	28	0.17	1.7	159
fluorescent ^a	APS/TEMED	18	68	0.16	0.8	125
dye-free	AIBN	92	38	0.10	1.6	180
fluorescent ^a	AIBN	83	≈ 300	0.50	1.2	133
dye-free	AAPH	99	33	0.18	1.4	163
fluorescent ^a	AAPH	99	44	0.13	1.2	159

^aNPs with covalently immobilized fluorophores **N2** and **R3**

Table 2.7: Influence of the co-polymerized fluorophores **N2** and **R3** on the yield of the microemulsion polymerization and on the morphology of the obtained NPs.

As shown in **Table 2.7** the yield of the polymerization using APS/TEMED as initiator system was strongly influenced by the dyes added to the aqueous phase. While co-polymerization with APS/TEMED gave only fair yields ranging from 18 - 65%, the dyes seemed to have no influence on the yields if AIBN or AAPH was used. The hydrodynamic diameters of the dye-loaded NPs were larger than those of the plain NPs independently from the type of initiator. The SEM micrograph in **Figure 2.26** shows, as already observed for the dye-free NPs, larger particle aggregates probably consisting of many small NPs.

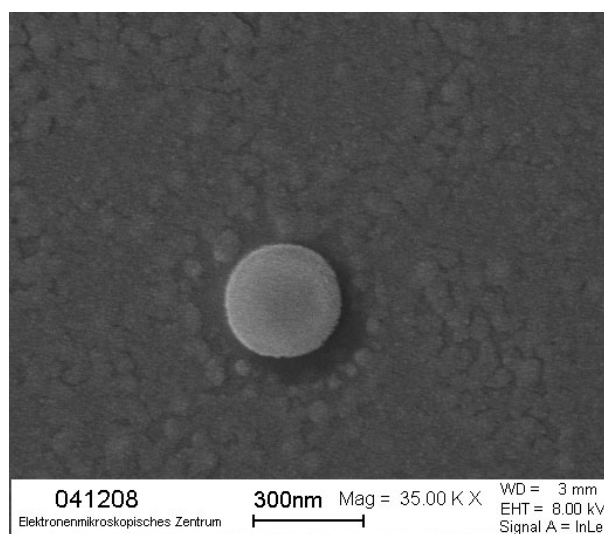


Figure 2.26: SEM micrograph of NPs containing N2 and R3 and polymerized with AAPH at 70 °C.

In particular, fluorescent particles polymerized with AIBN exhibited, to some exceptions, diameters in the range of a few hundred nanometers and high polydispersities. The BET-surface areas exhibited good agreement with the hydrodynamic diameters assuming spherical particles and a smooth particle surface (see equation 2.1). Only in case of AIBN the specific surface is higher than the expected surface which should be approximately 20 m²/g. A reason for the higher specific surface may be a high porosity of the particles.

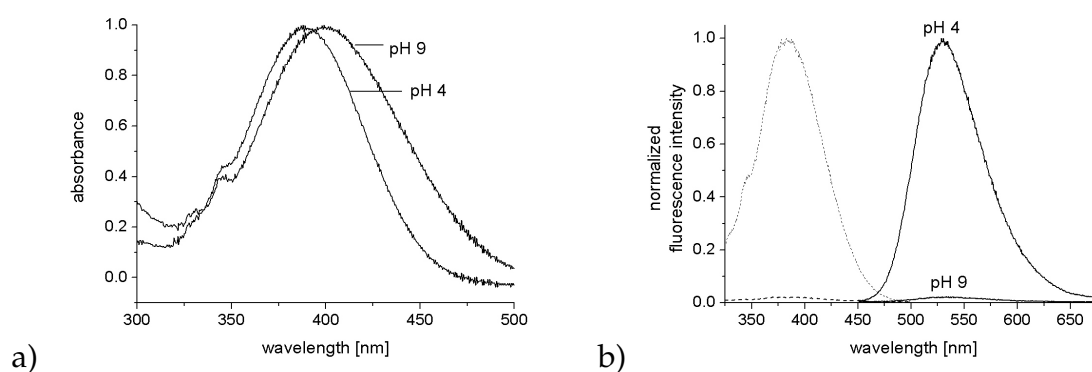


Figure 2.27: a) Absorption and b) fluorescence excitation (dashed line) and emission spectra (solid line) of the pH-indicator dye **N2** in phosphate buffered solutions of pH 4.0 and 9.0 (MeOH/H₂O 1:70, v/v), respectively. The excitation wavelength was 390 nm and the emission wavelength 530 nm.

2.3.3 Absorption and Fluorescence

The absorption spectra of **N2** in acidic and basic solutions are shown in **Figure 2.27 a)**. It appeared that the indicator dye exhibited an almost pH-independent absorbance around 380 nm, which is induced by the “push-pull” character of the aromatic system. In the ground state of the 4-amino naphthalimide fluorophore the naphthalimide moiety acts as an electron acceptor and the amino function as an electron donor. The excitation of the fluorophore causes the transfer of a ground state electron to the lowest excited singlet state. **Figure 2.28** depicts that, after excitation the charge distribution in the fluorophore is inverse due to an internal charge transfer (ICT).⁶⁸

When the pH of the solution was decreased from 9.0 to 4.0, a slight blue-shift of the maximum wavelength was observed. According to the literature, this is most probably caused by partial protonation of the amino group in 4-position leading to reduced ICT character of the fluorophore.⁶⁹

The excitation and emission spectra of dissolved **N2** in acidic and basic buffer are depicted in **Figure 2.27 b)**. In contrast to absorbance, the fluorescence spectra of the fluorophore showed a strong intensity decrease at higher pH. The quantum yield of the protonated form was about 10-fold higher than that of the unprotonated form

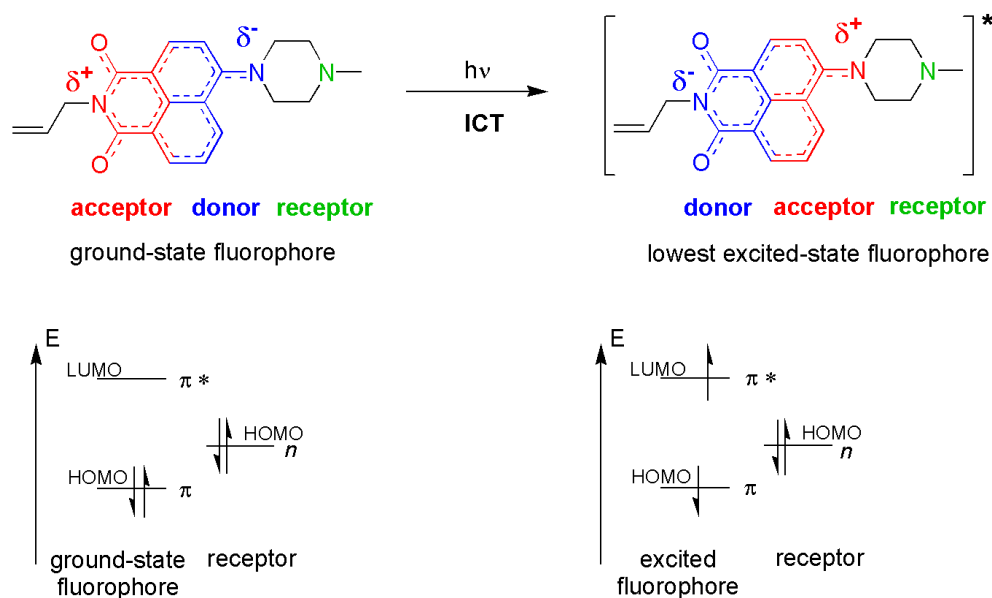


Figure 2.28: Schematic drawing of the “push-pull”-system and the molecular orbital levels for N2 in the ground state. Upon excitation the charge distribution changes due to an internal charge transfer (ICT).

of the dye. This explains why the indicator is considered as a so-called fluorescent “OFF-ON”-switch, whose fluorescence strongly increases in the presence of the analyte. The pH-sensing mechanism of N2 is based on intramolecular photoinduced electron transfer (PET) as depicted in **Figure 2.29** (see page 12).⁴⁸

Indicator dyes employing PET are also known as “OFF-ON”-switches, since they can switch between a nearly non-fluorescent form and a strongly fluorescent one, if the analyte is present in concentrations over a certain threshold.⁷⁰ In the unprotonated form of N2, the lone pair of the aliphatic nitrogen is available to contribute to the electron transfer and prevents fluorescence of the aromatic system (“OFF-state”). Upon presence of the analyte the lone pair of the aliphatic amino group is used for binding the proton. Now electron transfer to the aromatic system is suppressed and strong fluorescence becomes visible (“ON-state”).

The excitation and emission maxima of N2 were slightly shifted to shorter wavelengths upon incorporation of the fluorophore inside NPs (**Figure 2.30**). The maximum absorption, excitation and emission wavelengths as well as the quantum yields and molar extinction coefficients are summarized in **Table 2.8**.

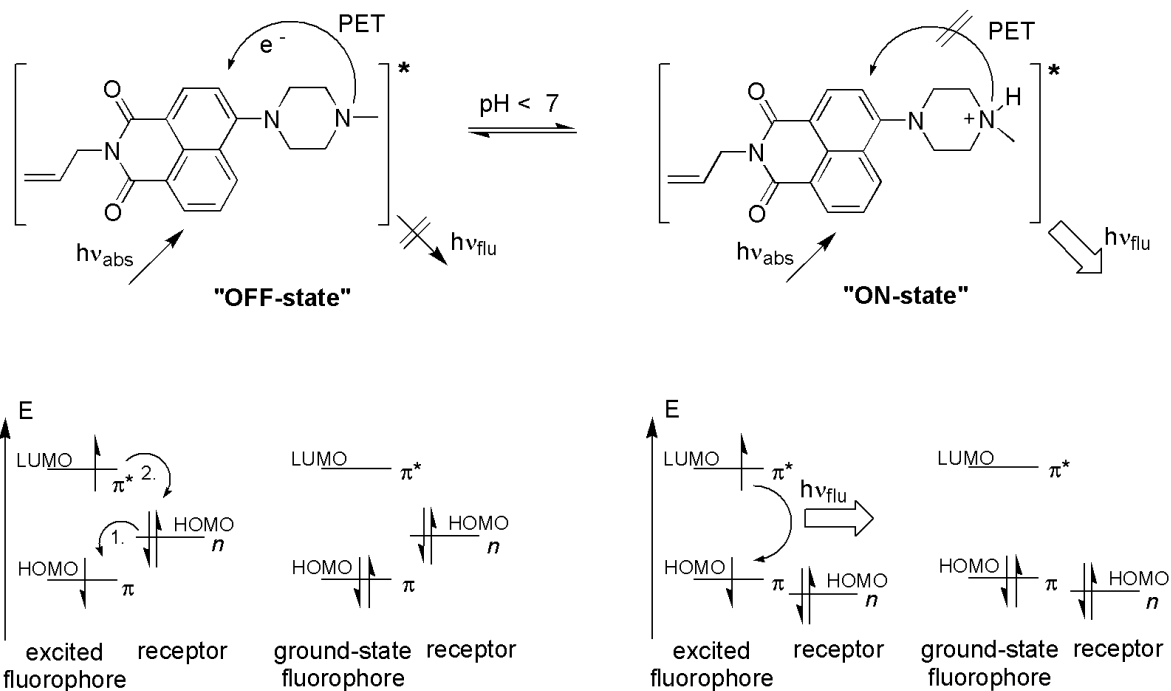


Figure 2.29: pH-Indicator dye N2 in the unprotonated form showing photoinduced electron transfer ("OFF-state"). At pH below 7 protonation of the methylpiperazine receptor group becomes significant, suppresses the PET process and strong fluorescence appears ("ON-state").

To evaluate if the covalent attachment of the pH-indicator dye to the polymer backbone was successful, a nanoparticle suspension was dialyzed against phosphate buffer for 24 hours. The spectra in **Figure 2.31** show, as in case of the chloride-sensitive NPs (see page 44), a decrease in fluorescence intensity. But in contrast to the NPs with the physically embedded lucigenin, the fluorescence of the covalently attached N2 started to decrease significantly after a dialysis time of more than 3 hours. Comparing the leaching rates of lucigenin and N2 after one hour shows that lucigenin leached by 14% and N2 by only 4%. After a dialysis time of 24 hours the fluorescence of lucigenin decreased by 32% while fluorescence of N2 dropped by 18%. Thus, leaching of the chemically bound fluorophore is reduced by almost 50% compared to the non-covalently bound lucigenin.

However, a decrease in fluorescence intensity (10%) of the likewise covalently bound dye R3 was observed as well. This is in agreement with the literature, where leaching of covalently bound fluorescein and rhodamine from poly(acrylamide) NPs

	N2 in solution		immobilized N2	
	pH 4	pH 9	pH 4	pH 9
λ_{abs} [nm]	388	399	-	-
λ_{exc} [nm]	383	378.5	387.5	376
λ_{em} [nm]	528.5	535.5	523.5	521
ϕ	0.45	$4.2 \cdot 10^{-2}$	-	-
ϵ [$M^{-1}cm^{-1}$]	≈ 10000	≈ 10000		

Table 2.8: Absorption, excitation, emission wavelengths, quantum yields (ϕ) and molar extinction coefficients (ϵ) of N2 dissolved in phosphate buffer and immobilized into NPs.

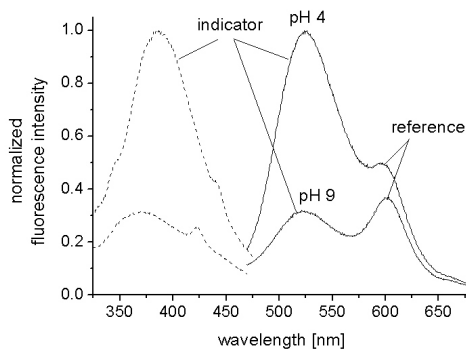


Figure 2.30: Excitation (dashed line) of N2 inside the NPs and emission spectra (solid line) of NPs showing the fluorescence of the pH-indicator dye N2 and the reference dye R3. All spectra were recorded in phosphate buffer at $\lambda_{exc}/\lambda_{em} = 390/525$ nm.

was up to 9% within 6 hours.²⁶ An explanation might be that residual non-polymerized dyes were washed out of the NPs or that a minor amount of very small (≤ 2 nm) nanoparticles diffused through the dialysis membrane. Dilution effects can be eliminated by plotting the ratio of both fluorescence intensities against the dialysis time.

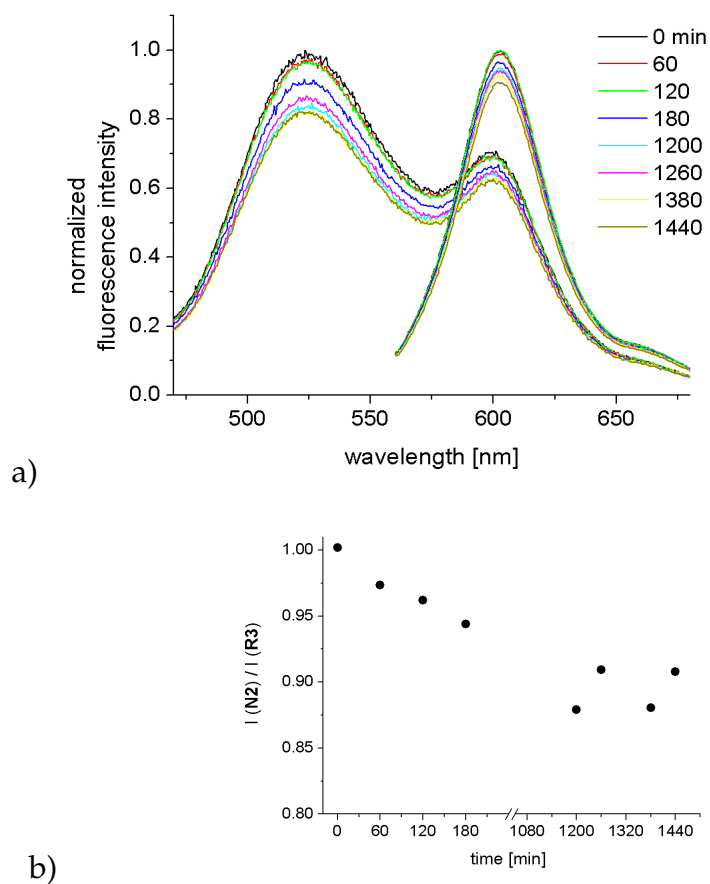


Figure 2.31: a) Emission spectra of NPs containing **N2** ($\lambda_{em} = 520$ nm) and **R3** ($\lambda_{em} = 604$ nm) before and after 60, 120, 180, 1200, 1260, 1380 and 1440 min of dialysis against phosphate buffer. b) The ratio of fluorescence intensities ($I(N2)_{520nm}/I(R3)_{604nm}$) depending on the dialysis time.

2.3.4 Response to pH

The response of the dissolved indicators to pH is depicted in **Figure 2.32**. The pK_a was obtained by plotting the fluorescence intensity against the pH of the solutions. In case of the sensor particles additionally containing the reference dye, the ratio between the intensities of both dyes was plotted depending on the pH of the suspensions (**Figure 2.33**). The pK_a of the indicator dye in solution was 6.15 ± 0.2 and that of the NPs 6.73 ± 0.3 , which is in agreement with pK_a -values reported for similar indicator dyes.⁶⁶

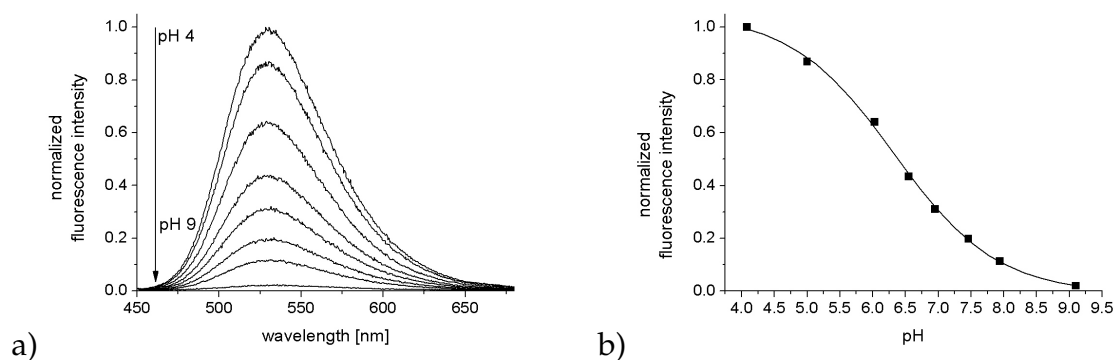


Figure 2.32: a) Emission spectra and b) calibration graph of N2 in phosphate buffered solutions of increasing pH (MeOH/H₂O 1:70, v/v). The intensity for the calibration graph was taken at 530 nm.

Upon immobilization of the sensor dye inside the polymer NPs the relative signal change was reduced. The fluorescence intensity of free N2 dropped by 98% with increasing pH of the solution from 4.0 to 9.0, whereas the fluorescence of N2 inside the NPs only decreased by 68%. The loss in sensitivity after dye immobilization was probably due to the same effect as already explained for the chloride-sensitive NPs. The incorporation of the indicator inside the particles hampered the access of the analyte to the dye. Eventually dye molecules deep inside the polymer matrix were even not accessible to the analyte at all. Protonated dye molecules that were enclosed in the NPs during polymerization might be still present and contribute to the fluorescence of the NPs. When the pH of the suspension medium was decreased, these dye molecules remain unaffected i.e. protonated. That would also explain the

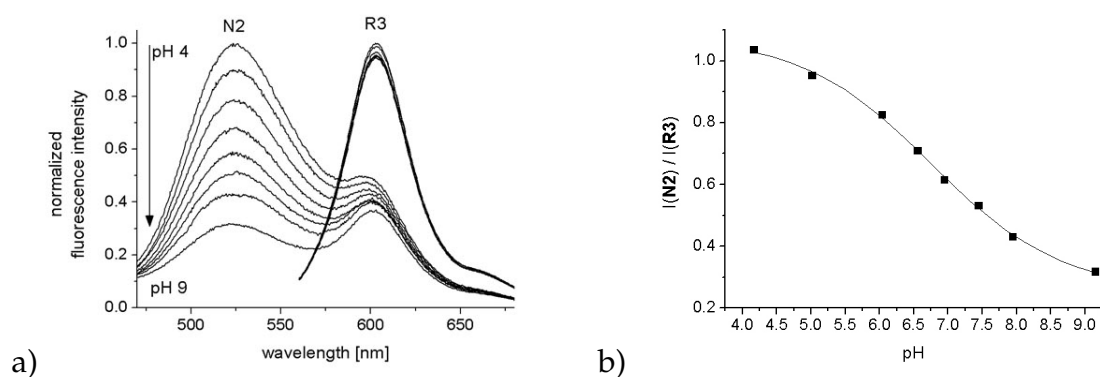


Figure 2.33: a) Emission spectra ($\lambda_{exc}/\lambda_{em,N2} = 390/520$ nm; $\lambda_{exc}/\lambda_{em,R3} = 543/604$ nm) and b) calibration graph of the NPs containing **N2** and **R3** in phosphate buffered suspensions of increasing pH. The ratio of fluorescence intensities ($I(\mathbf{N2})_{520nm}/I(\mathbf{R3})_{604nm}$) was used for the calibration plot.

higher pK_a of 6.73 inside the particles compared to the pK_a of 6.15 in solution. The sensitivity was determined from the slope of the sigmoidal calibration plot. The calibration of the pH-indicator in solution gave a slope of 0.56 per pH unit and that of the sensor-NPs a slightly lower slope of 0.46 per pH unit. The dynamic range was given by the linear part of the calibration plot. The dissolved indicator exhibited dynamic response in the pH-range from 4.6 to 8.0 and the immobilized **N2** in the range from pH 5.0 to 8.2.

2.3.5 Interfering Species

Influence of Ionic Strength

The ionic strength (IS) of different bio-samples can significantly vary depending on the type of biological material. Highly charged indicator dyes such as HPTS are known to show strong cross-sensitivity to changes of ionic strength, while the single charged **N2** should be less sensitive. To prove this thesis, the NPs have been evaluated regarding their cross-sensitivity to increasing concentrations of sodium chloride in the buffered suspensions (**Figure 2.34**).

Unexpectedly, a constant increase of the pK_a -values with rising IS of the suspension was observed. The pK_a of the NPs raised from 6.73 in plain phosphate buffer

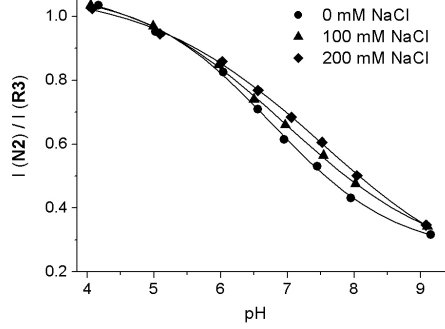


Figure 2.34: Effect of increasing IS on NPs containing **N2** and **R3**. The plot shows the calibration graphs for increasing sodium chloride concentrations (100 mM and 200 mM) of the phosphate buffer (pH 7.0).

to 6.98 and 7.50 in buffer with 100 mM and 200 mM NaCl, respectively. Therefore it was concluded that also the single charge in the protonated form of **N2** affects the cross-sensitivity. The reason for the higher pK_a -values is that the IS is related to the activity coefficient of the dye. According to the Henderson-Hasselbalch equation (equation 2.5) the pK_a only depends on the concentrations of the protonated ($[NH^+]$) and the unprotonated form ($[N]$) of **N2**, since the pH of the buffered nanoparticle suspension is constant. The ratio of the two dye forms $[N]/[NH^+]$ is reciprocally proportional to the activity coefficients (f) leading to the following equation:

$$pK_a = pH - \log \frac{[N]}{[NH^+]} \approx pH - \log \frac{f_{NH^+}}{f_N} \quad (2.10)$$

The ionic strength (IS) and the mean activity coefficient (f_{\pm}) are defined as follows:

$$IS = 1/2 \sum_i z_i^2 \cdot m_i \quad (2.11)$$

$$\lg f_{\pm} = -|z_+ \cdot z_-| A \sqrt{I/m^\circ} \quad (2.12)$$

where z is the charge of the species and m and m° are the molality and the molality of a hypothetical ideal solution. The parameter A is 0.509 for aqueous systems at 25 °C. With rising IS the activity coefficient of the protonated form decreases stronger than the activity coefficient of the neutral unprotonated form. Hence, the ratio f_{NH^+} / f_N becomes smaller and the pK_a increases.

Interaction with Proteins

As in case of the chloride-sensitive NPs, the fluorophores in solution and inside the particles were examined towards their reaction with bovine serum albumin (BSA). To a buffered solution containing both **N2** and **R3** BSA was added to give a solution of 1 wt.-%. The fluorescence of **R3** was quenched by 8%, whereas the fluorescence of **N2** increased by 23% in presence of the protein (**Figure 2.35 a**). In biological samples variations in protein concentration would consequently lead to changes in fluorescence intensity that are not caused by the analyte.

The spectra of the dye-containing NPs (**Figure 2.35 b**) demonstrate that the polymer matrix exhibited a protection effect against the entrance of larger bio-molecules such as BSA. Neither the fluorescence of the reference dye nor the fluorescence of the pH-indicator was affected by albumin, if they were incorporated inside the particles. **Figure 2.36** shows that a calibration of the NPs in presence of 1 wt.-% BSA is still possible, although no sigmoidal fit according to Henderson-Hasselbalch was obtained. The correlation between fluorescence intensity and pH was almost linear in the pH-range from 5.0 to 8.4. This might be due to protonation of the protein or protein adsorption at the surface of the particles.

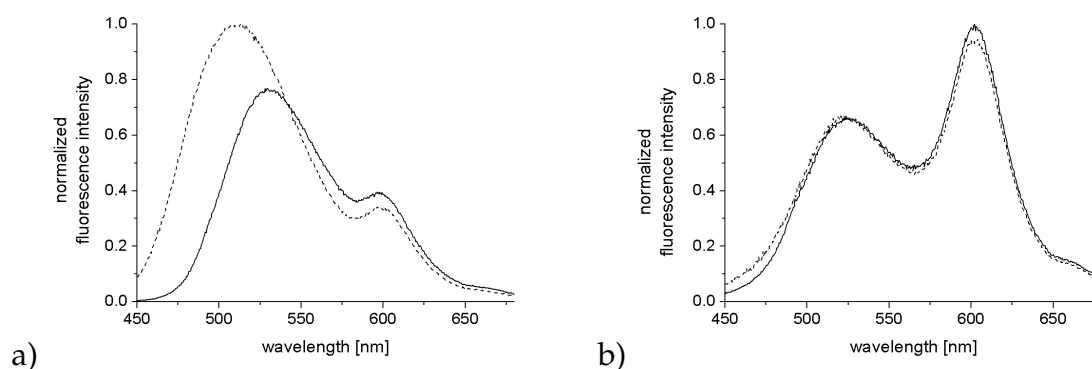


Figure 2.35: Emission spectra of **N2** and **R3** in absence and presence of BSA. a) Fluorescence of **N2** in buffered solution of pH 7.0 (solid line) and in a solution containing 1 wt.-% BSA (dashed line). b) Fluorescence of **N2** and **R3** containing NPs in buffered suspension (pH 7.0) without BSA (solid line) and with 1 wt.-% BSA (dashed line). The fluorescence spectra were obtained by excitation at 420 nm in order to avoid autofluorescence of BSA.

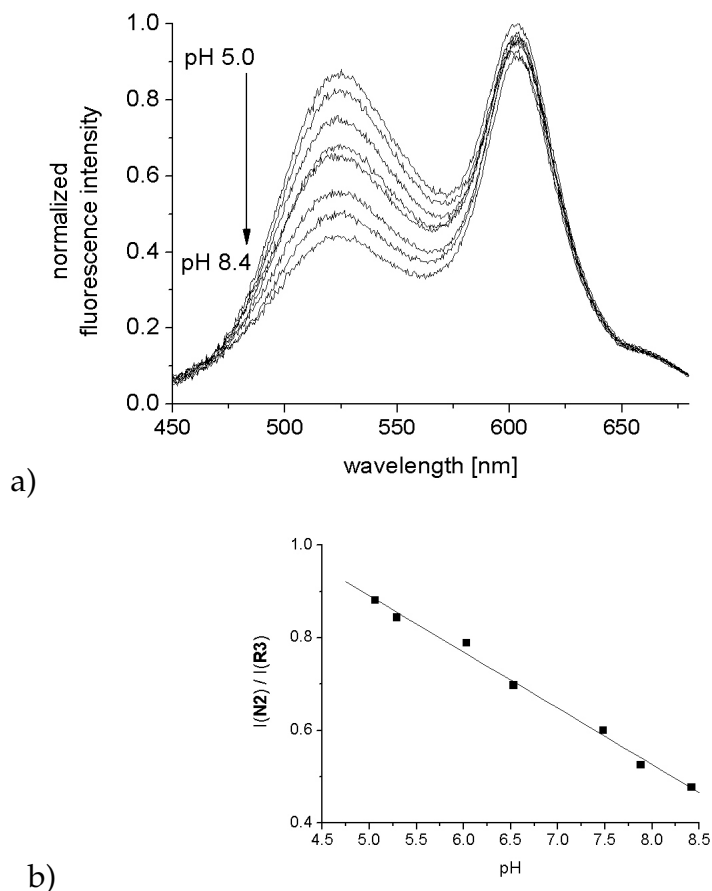


Figure 2.36: a) Emission spectra and b) calibration graph of the NPs containing **N2** and **R3** in presence of 1 wt.-% BSA. The fluorescence spectra were obtained by excitation at 420 nm in order to avoid autofluorescence of BSA.

2.3.6 Photostability and Stability against Oxidation

Measurements with fluorescence microscopes require stable dyes, which are inert against irradiation by light of high intensity (e.g. lasers are common excitation light sources). To examine how the fluorophores were affected by continuous irradiation, a cuvette with either a solution of both dyes or a nanoparticle suspension was exposed to the excitation light source (450 W xenon lamp) in the fluorescence spectrometer. While the pH-sensitive dye **N2** exhibited very good photostability in solution, a decomposition was observed, when **N2** was incorporated inside NPs. After irradiation of the nanoparticle suspension for 2 hours the fluorescence intensity of **N2** decreased by 14% as shown in **Figure 2.37**.

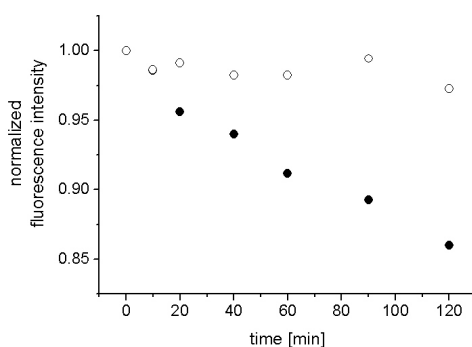


Figure 2.37: Fluorescence intensity of **N2** (●) at 520 nm and **R3** (○) at 604 nm inside the NPs before and after irradiation with a xenon lamp for 10, 20, 40, 60, 90 and 120 minutes, respectively.

The enhanced decomposition of the embedded fluorophore may be related to the lower mobility of the dye inside the polymer matrix and of the particles themselves in the aqueous suspension. Compared to the dye in solution, which can release the absorbed energy also by translation, the relaxation of the embedded fluorophore is hindered due to the reduced mobility. In contrast to the pH-indicator the reference dye is neither affected in solution nor inside the particles. According to the constant fluorescence signal from the reference dye sedimentation of the NPs was excluded. However, if compared to similar nanoparticles with a covalently attached fluorescein derivative (decrease about 30%), the photostability of **N2** is significantly better.^{26,63} The enhanced stability of the naphthalimide fluorophore compared to fluoresceins was demonstrated by exposure of **N2** to increasing concentrations of hydrogen peroxide. As expected, neither the dye in solution nor the incorporated dye was oxidized by hydrogen peroxide in concentrations up to 110 mM.

3

Functionalization of Nanoparticles

In order to enhance both the cellular uptake and the endosomal escape NPs had to be developed bearing positively charged surface groups and/or a positive ζ -potential (see page 15). Particles or vesicles with cationic surface groups are able to associate with negatively charged biological membranes, which enhances the passage through the membrane. Commercially available cell-transfection substances are amphiphilic compounds possessing a lipophilic hydrocarbon chain and a hydrophilic tertiary amino group. They form small vesicles that are able to transfer their content (e.g. nanoparticles) into the cell. Upon internalization the nanoparticles are mostly located in endosomes and later in lysosomes. These compartments of the cell are less interesting from the analytical point of view. Therefore, the sensor particles need to escape from this cellular vesicles by an active process. This so-called endosomal escape is observed for swellable NPs that possess a much higher diameter at acidic conditions or for positively charged NPs having a constant diameter. Different methods for preparation of NPs with positive surface charge and for synthesis of swellable NPs have been evaluated.

3.1 Surface Coating

A facile method for modification of the already existing poly(acrylamide) NPs is the surface-coating with polycationic polymers. Polymers like polyethylene imine (PEI) or poly-L-lysine⁷¹ possess many amino groups that are protonated at neutral and

acidic conditions (e.g. in the endosomes). In particular, branched PEI exhibiting primary, secondary and tertiary amino functions is frequently used for coating of particles and drugs that need to be delivered to the cytosol of cells.

m (PEI) ^a [mg]	m (NPs) ^b [mg]	$m(\text{PEI})/m(\text{NPs})$	m (PEI) ^c [mg]	m (NPs) ^b [mg]	$m(\text{PEI})/m(\text{NPs})$
70	50	1.4	8	50	0.16
250	50	5	32	50	0.64
500	50	10	50	50	1.0
			500	50	10

^aPEI 10 kDa dissolved in 10 mL of a 25 mM sodium acetate buffer

^bsuspended in 4 mL of a 25 mM sodium acetate buffer

^cPEI 600 Da dissolved in 10 mL of a 25 mM sodium acetate buffer

Table 3.1: Composition of the coating solutions and the nanoparticle suspensions.

The cross-linked poly(acrylamide) NPs have been coated with PEI according to Fuller *et al.*⁷¹ For preparation of the coating solutions PEI of high molecular weight (10 kDa) and in a second approach low molecular weight PEI (600 Da) was dissolved in sodium acetate buffer. The nanoparticle suspensions were added to these solutions and stirred for ten minutes. The compositions of the coating solutions and the nanoparticle suspensions are shown in **Table 3.1**. After coating residual PEI was removed by extensive dialysis of the NPs against water. The modified NPs were precipitated by dialysis against ethanol, centrifuged and dried *in vacuo*.

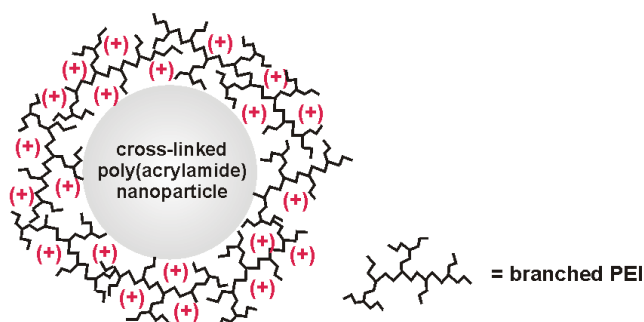


Figure 3.1: Schematic drawing of a poly(AAm) nanoparticle coated with PEI.

It appeared that the NPs coated with PEI of 10 kDa molecular weight were not

completely suspendable in aqueous media anymore. Instead, large aggregates were formed in buffered solutions of pH 5.0 to 8.0 that could be seen by the naked eye. The coating with 600 Da PEI was probably not successful, since the coated particles, which were easily suspendable in buffer, exhibited the same hydrodynamic diameter and a still neutral ζ -potential. It can be assumed that the PEI was completely washed out during dialysis. This shows the main drawback of the surface coating with polymers: the PEI was only physically attached to the NPs *via* electrostatic interactions between the accessible negative surface groups on the particles and the positive ammonium groups of the PEI. Due to the fact that the poly(acrylamide) NPs exhibited a nearly neutral surface charge, the electrostatic interactions were too low to significantly attract the PEI. Therefore, a simple electrostatic coating of polyacrylamide was not possible. An alternatively covalent surface modification requires reactive groups on the nanoparticle surface, which are not present in poly(acrylamide). Therefore the material the NPs were made of was changed from poly(acrylamide) to poly(amino ethyl methacrylates).

3.2 pH-swellable poly(DEAMA) Nanoparticles

Recently, Hu *et al.* reported the synthesis of swellable core-shell NPs possessing additionally a positive surface potential.⁷² According to this reference NPs have been synthesized by a surfactant-free emulsion polymerization in water. In contrast to Hu *et al.* the particles consisted only of the pH-responsive core, where *N,N*-diethyl-2-aminoethyl methacrylate (DEAMA) was used as the monomer and poly(ethylene glycol) dimethacrylate (PEGDMA) as the crosslinker. The diethylamino groups of poly(*N,N*-diethyl-2-aminoethyl methacrylate) (PDEAMA) were protonated at pH below 7.0 and as a result, the positively charged ammonium groups in the protonated PDEAMA repelled each other. The relatively flexible crosslinker PEGDMA enabled a sharp increase in volume of the particles around the pK_a of the diethylamino group (**Figure 3.2**). In order to examine the influence of the polymer matrix on the performance of the dye, NPs were synthesized containing either the pH-sensitive fluorophore **N2** or the reference dye **R3**.

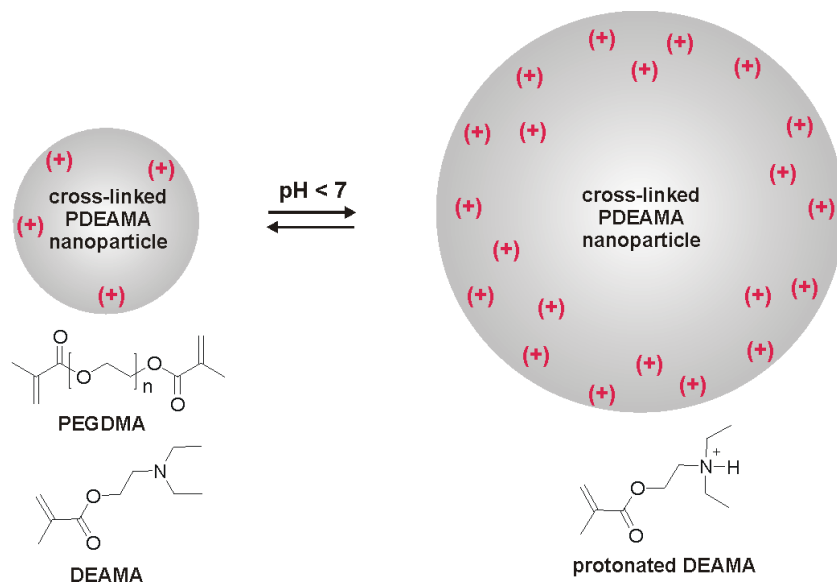


Figure 3.2: Schematic drawing of PDEAMA NPs and their swelling upon protonation of the diethylamino groups.

Due to the surfactant-free polymerization in an oil-in-water emulsion the final NPs were larger in diameter than the particles obtained from w/o microemulsion polymerization. **Figure 3.3** shows the hydrodynamic diameter of N2-containing PDEAMA particles depending on the pH of the suspension. The NPs swelled to more than the double size, when the pH dropped from 8.5 to 4.8. The sharp change of the nanoparticle diameter at a pH around 7 correlated well with the pK_a of the diethylamino group. The swelling was accompanied by the appearance of a number of small particles (d_H around 6 nm) resulting in an increase of the polydispersity from PDI = 0.02 to 0.22. The PDI did not increase at high pH due to formation of larger particle aggregates as expected, but at low pH. An explanation for this surprising behavior could be the disaggregation of a nanoparticle into many small polymer beads as the electrostatic repulsion became stronger. The same was observed for NPs with the immobilized reference dye **R3**.

The examination of the nanoparticle suspensions using fluorescence spectroscopy gave no interpretable results. Similar to the poly(acrylamide) NPs the fluorescence intensity of N2 was highest at pH 5 and strongly decreased, if the pH was raised to 7. When the basicity was further increased to pH 8 the fluorescence of N2 showed an unexpected increase to the initial intensity (**Figure 3.4 a**). Addition-

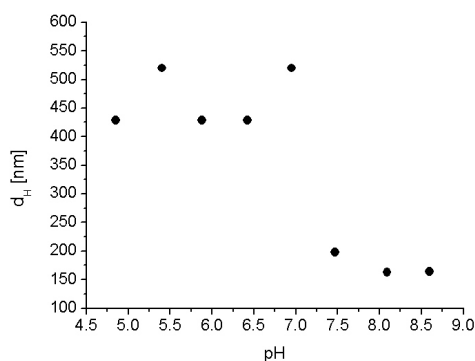


Figure 3.3: The hydrodynamic diameter of the PDEAMA NPs in suspensions of varying pH shows the sharp volume increase at a pH of 7. The fluctuations in the hydrodynamic diameters at acidic conditions are caused by the measurement increments of the device.

ally, the excitation wavelength was red-shifted from 382 to 394 nm and the emission maximum blue-shifted from 527 to 498 nm. Similarly, the fluorescence of the NPs containing the reference dye **R3** switched to higher intensities, when the pH was changed from 7 to 8 (**Figure 3.4 b**). Hence, it was assumed that with the changing size of the particles the microenvironment of the fluorophores was also changed leading to unpredictable fluorescence properties.

3.3 Core-Shell Nanoparticles

Similar to the previous approach using PDEAMA, core-shell NPs have been synthesized, which had a positive ζ -potential but showed minor pH-induced swelling. The monomer used for the nanoparticle-core was *N,N*-dimethyl-2-aminopropyl acrylamide (DMAPA) and the monomer for the shell was acrylamide (AAm). Both monomers were cross-linked with *N,N'*-methylene bisacrylamide. Since the dimethylamino group of the core-polymer is expected to have a pK_a of around 6.7, the particles are supposed to exhibit a positive ζ -potential and by the use of *N,N'*-methylene bisacrylamide as the crosslinker a more rigid polymer backbone. In this manner, a pH-dependent swelling of the NPs due to protonation and repulsion of the dimethylamino group should be prevented. Poly(acrylamide) (PAAm) was chosen as the shell material in order to provide a neutral and non-toxic surface for the

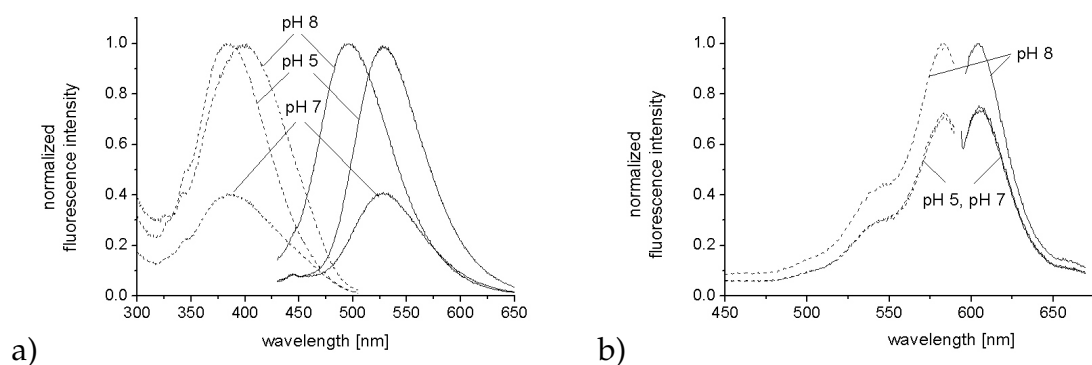


Figure 3.4: Fluorescence excitation (dashed line) and emission spectra (solid line) of PDEAMA NPs a) with immobilized **N2** ($\lambda_{exc}/\lambda_{em} = 390/525$ nm) and b) with **R3** ($\lambda_{exc}/\lambda_{em} = 583/604$ nm).

nanoparticles (**Figure 3.5**).

Attempts to prepare nanoparticles consisting only of the cross-linked core polymer poly(*N,N*-dimethyl-2-aminopropyl acrylamide) (PDMAPA) as well as nanoparticles with a shell made of PDMAPA failed. The usual precipitation of the polymer with ethanol was not observed for PDMAPA particles. This hampered the conventional isolation and purification of the beads after their preparation. Other purification methods such as dialysis or precipitation of the polymer with other solvents (acetone, ether) were also not successful.

For preparation of PDMAPA-core/PAAm-shell NPs a two-stage w/o microemulsion polymerization was employed. For optical sensing of pH the fluorescent pH-indicator dye **N2** was co-polymerized in the shell and the reference dye **R3** in the core of the NPs. The positively charged surfactant cetyltrimethylammonium bromide (CTAB) was used instead of the negative AOT, which is thought to form an ion pair with the protonated amino group of the DMAPA. Due to the limited solubility of CTAB, more of the neutral surfactant Brij 30 was needed to form a stable inverse microemulsion. The emulsion polymerization without the co-surfactant CTAB using only Brij 30 gave large and polydisperse NPs ($d_H = 155$ nm, PDI = 0.4) exhibiting a positive ζ -potential (+33 mV at pH 4) as well. Thus, a positive surface potential due to residual CTAB can be excluded.

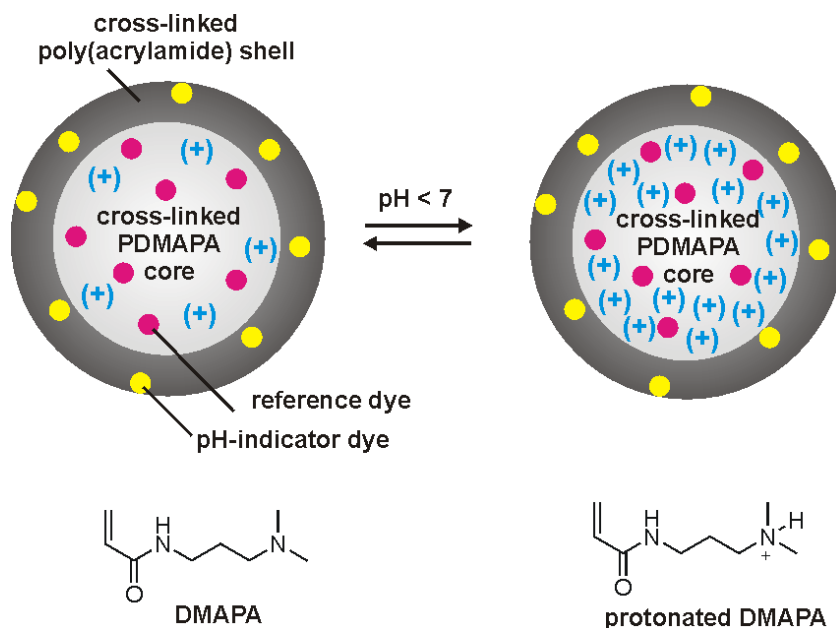


Figure 3.5: Schematic drawing of the core-shell NPs and their protonation at acidic conditions.

3.3.1 Size and Zeta-Potential

The core-shell NPs were evaluated regarding their size distribution and ζ -potential in aqueous buffered suspensions. As depicted in **Figure 3.6** the core-shell NPs had a hydrodynamic diameter of 38 nm at pH 7.0 and, compared to the poly(acrylamide) NPs, a broader size distribution (PDI of 0.31). In contrast to the PDEAMA NPs, a swelling due to protonation of the alkylamino groups in the core polymer was prevented. However, an opposite behavior was observed: the diameter of the core-shell NPs slightly increased, if the pH of the suspension was raised from 3.0 to 10.0.

The PDMAPA core induced a positive ζ -potential of the particles in buffered suspensions of pH 3.0 to 10.0. **Figure 3.7** shows the ζ -potential in dependence on the pH of the nanoparticle suspensions. The surface potential dropped from $+29.7 \pm 6$ mV to $+10.6 \pm 4$ mV as the acidity decreased from pH 3.0 to pH 10.0. A sharp decrease of the potential was observed around pH 6.5, which is in accordance with the pK_a of PDMAPA.

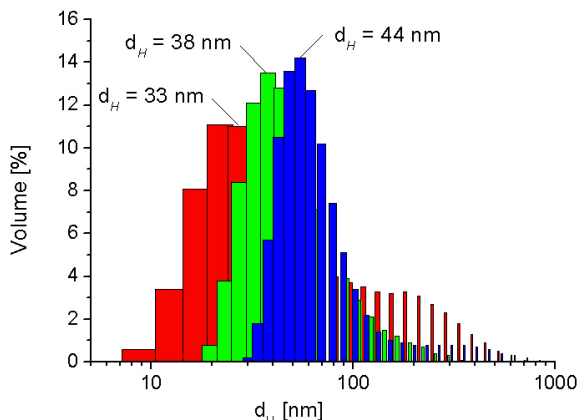


Figure 3.6: Hydrodynamic diameter of the PDMAPA-core/PAAm-shell NPs measured in phosphate buffered suspensions of pH 3.0 (red), pH 7.0 (green) and pH 10.0 (blue).

3.3.2 Fluorescence and Sensing Properties

The optical properties of the immobilized dyes inside the NPs were evaluated using fluorescence spectroscopy. The excitation and emission wavelengths are summarized and compared to data from poly(acrylamide) NPs in **Table 3.2**.

Fluorophore	λ_{exc} [nm]	λ_{em} [nm]	Stoke's shift [nm]
N2 in PAAm (acidic)	387	523	136
(basic)	376	521	145
N2 in core-shell NPs (acidic)	386	522	136
(basic)	390	506	116
R3 in PAAm	585	605	20
R3 in core-shell NPs	571	589	18

Table 3.2: Excitation/emission wavelengths and Stoke's shift of **N2** and **R3** inside the poly(acrylamide) NPs (PAAm) and inside the core-shell NPs.

At acidic pH, the excitation and emission maxima of **N2** in the core-shell NPs ($\lambda_{exc}/\lambda_{em} = 386/522$ nm) were nearly the same as for the poly(acrylamide) NPs ($\lambda_{exc}/\lambda_{em} = 387/523$ nm). However, when the pH of the core-shell nanoparticle

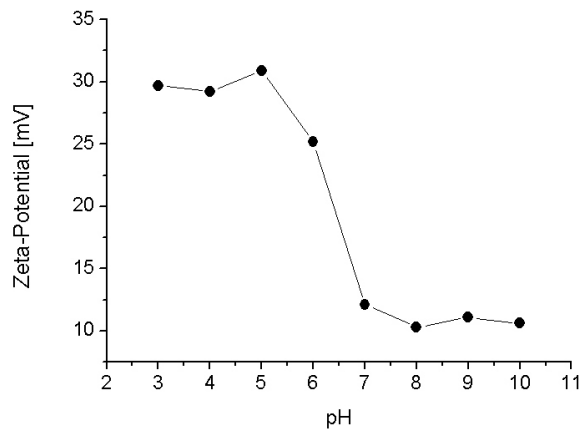


Figure 3.7: Zeta-potential of the PDMAPA-core/PAAm-shell NPs measured in phosphate buffered suspensions of pH 3.0 to 10.0.

suspension was raised to 9.2, a shift in both excitation and emission maxima was observed. The excitation showed a red-shift to 390 nm and the emission was shifted to shorter wavelengths ($\lambda_{em} = 506$ nm). The same was observed for the dye inside the PDEAMA nanoparticles. The excitation and emission wavelengths of the incorporated reference dye **R3** were also blue-shifted to $\lambda_{exc} = 571$ nm and $\lambda_{em} = 589$ nm, respectively. The shift in excitation and emission maxima of both dyes is probably related to the changing microenvironment as mentioned for the PDEAMA NPs. The spectra of **N2** and **R3** incorporated inside the core-shell NPs are shown in (**Figure 3.8**).

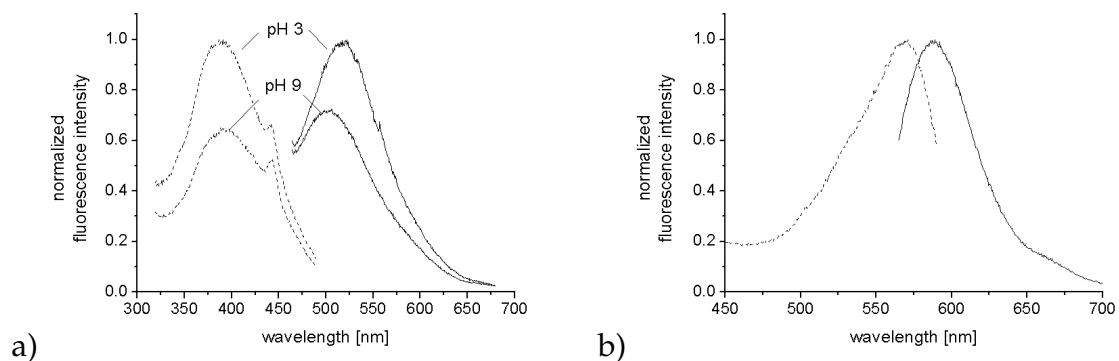


Figure 3.8: Excitation (dashed lines) and emission spectra (solid lines) of a) **N2** and b) **R3** inside the PDMAPA-core/PAAm-shell NPs.

The response of the fluorophores inside the core-shell NPs to varying pH of the suspensions is depicted in **Figure 3.9**. In case of **N2** a decrease in fluorescence intensity with increasing pH was observed, which is in agreement with the results from the fluorescent poly(acrylamide) particles. The fluorescence intensity of **R3** slightly increased with rising pH may be due to the concomitant size increase of the core-shell NPs. Plotting the ratio of both fluorophore signals *versus* the pH gave an almost linear dependency and the determination of a pK_a -value was not possible. This behavior might also be attributed to the highly charged polymer core, which was in close proximity to the indicator dye in the nanoparticle shell.

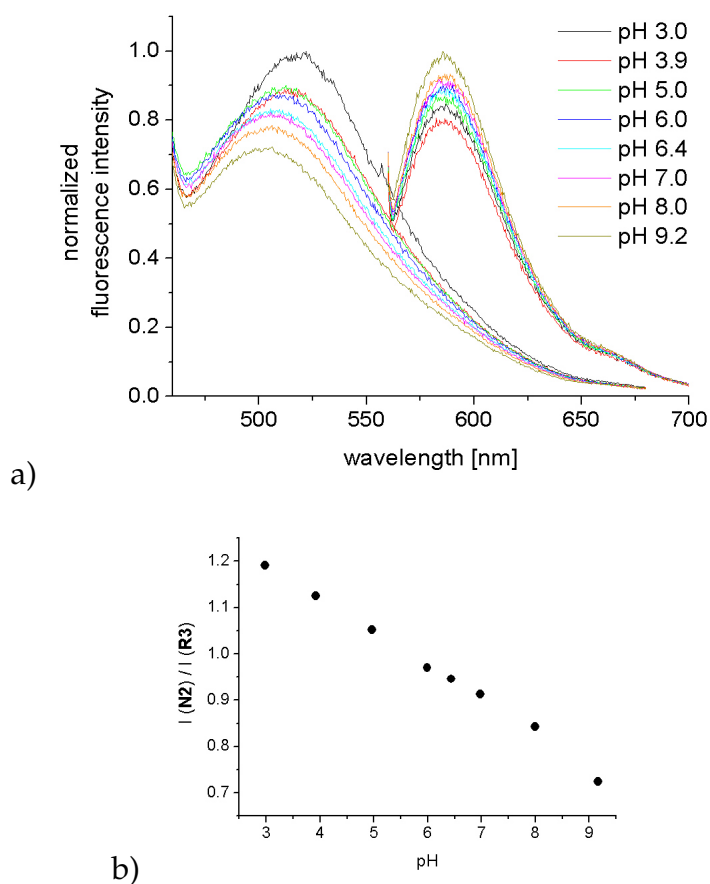


Figure 3.9: a) Response and b) calibration plot of the PDMAPA-core/PAAm-shell NPs to increasing pH of the buffered suspensions. The excitation wavelengths were 390 nm for **N2** and 543 nm for **R3**, respectively. The ratio of fluorescence intensities was taken at $I(N2)_{510nm}/I(R3)_{590nm}$.

4

Discussion and Conclusion

4.1 Inverse Microemulsion Polymerization

Inverse microemulsion polymerization was chosen to develop cross-linked poly-(acrylamide) particles in the nanometer range. It could be shown that the size of the inverse micelles was mainly controlled by the surfactant-to-water ratio r_{SW} . A two-fold increase of r_{SW} from 2.36 to 4.67 gave a seven-fold decrease of the inverse micelles from 68 nm to 10 nm diameter (see page 33). In this manner a control of the final polymer nanoparticle size was supposed to be achieved. However, it was observed that the nanoparticle size was slightly affected by r_{SW} . An increase of r_{SW} from 2.36 to 2.9 and 3.5 yielded NPs, which were only 4 nm less in diameter. This can be explained by the fusion of two or more water droplets to one larger droplet during the polymerization. The slightly increased dispersity (PDI 0.1 - 0.2) of the obtained NPs compared to the narrow dispersity (PDI 0.1) of the micelles might result from droplet fusion as well. With rising temperature of the inverse microemulsion the one-phase area in the pseudo-ternary phase diagram became smaller. Hence, for polymerization at 70 °C more surfactant respectively less aqueous component, was needed to obtain a homogeneous one-phase microemulsion.

The choice of the initiator seemed to have no influence on the yield and size of the resulting nanoparticles, when the polymerization was carried out without fluorophores. The redox-initiator system APS/TEMED and the azo-initiators AIBN and AAPH were selected as radical starters because of their different solubilities. The hy-

drophilic initiators APS/TEMED and AAPH started the polymerization inside the inverse micelles. The more hydrophobic AIBN was supposed to initiate the polymerization at the interface between the continuous oil-phase and the water droplets. This assumption is supported by the NPs obtained by co-polymerization of the fluorescent pH-indicator dye **N2** and the reference fluorophore **R3**. The particles polymerized with AIBN were much larger in size compared to the non-fluorescent NPs and to the fluorescent ones polymerized with AAPH or APS/TEMED. Thus, both the AIBN and the co-polymerized fluorophores seemed to affect the polymerization process.

4.2 Structural and Physico-chemical Properties

The polymerized NPs were purified either by ultrafiltration or by centrifugation. As determined by solid state-NMR experiments the amount of residual surfactants and unreacted monomers was less than 5%. The non-fluorescent NPs were obtained in good to nearly quantitative yields, whereas immobilization of fluorophores significantly decreased the yield of the polymerization with APS/TEMED. The NPs were easily suspendable in aqueous media by ultrasonification forming stable and optically transparent suspensions. Examinations of the particle suspensions using DLS gave hydrodynamic diameters in the range of 30 nm and polydispersities from 0.1 to 0.2. The size of the non-fluorescent NPs was nearly independent from the type of initiator, polymerization temperature, surfactant-to-water ratio and pH of the suspension medium. On the contrary, immobilization of the fluorophores significantly affected the size and PDI of the NPs, depending as well on the type of initiator and thus the location where the polymerization was started. As already mentioned, the NPs with embedded fluorophores were larger in size than the plain particles, but particularly the NPs polymerized with AIBN possessed very large diameters.

The specific surface of the NPs was obtained from nitrogen adsorption and the resulting isotherms were evaluated according to Brunauer, Emmett and Teller (BET). The slightly larger diameter of the dye-doped NPs resulted in smaller BET-surfaces (125 - 160 m²/g) compared to that of the plain NPs (160 - 180 m²/g). Independent

from the type of initiator, the densities of the fluorescent NPs ($0.8 - 1.2 \text{ g/cm}^3$) were determined to be lower than that of the dye-free particles ($1.4 - 1.7 \text{ g/cm}^3$). Under assumption of a spherical particle geometry and a smooth surface a theoretical particle diameter was calculated. In case of APS/TEMED and AAPH as radical starters the hydrodynamic diameters from DLS and the calculated diameters were in good agreement. The measured specific surfaces were a little larger than the expected particle surfaces, which indicates a rough surface and/or porosity of the particles. If AIBN was used as initiator, the determined specific surface area was two times higher than the calculated one for the dye-free NPs and six times higher for the dye-doped NPs. This indicates that the particle surface is rougher and the porosity increased compared to the two other initiators. The difference in particle morphology may be explained by the previously mentioned influence of the location, where the polymerization was started.

The ζ -potential measurement revealed that the poly(acrylamide) NPs exhibited a near-zero surface potential. A positive or negative ζ -potential resulting from the introduction of charged polymer chain end groups by the use of radical initiators could not be observed. Therefore, a stabilization of the colloidal particle suspensions *via* electrostatic repulsion was not possible and it is assumed that the suspensions were sterically stabilized. As the particles were suspended in buffered solutions they probably swelled after inclusion of water in the polymer matrix. This hydrogel-like behavior prevented the aggregation and sedimentation of the NPs. Upon drying the water was removed from the polymer and the NPs aggregated to larger assemblies, as observed by electron microscopy (SEM).

4.3 Chloride-Sensitive Nanoparticles

The chloride-sensitive NPs were prepared by physical entrapment of lucigenin inside the poly(acrylamide) backbone. Lucigenin fulfilled most of the requirements of a chloride-sensitive fluorophore:

- high Stern-Volmer constant (K_{SV}) \rightarrow high sensitivity to the analyte
- long-wavelength absorption and emission maxima

- large Stoke's shift
- high quantum yield
- high water-solubility
- reversibility of the analyte recognition
- large signal changes

Unfortunately, a modification of the dye in order to introduce a polymerizable function was not possible without hampering one of the above mentioned properties.

To enable ratiometric measurements the fluorescent reference dye **R3** was co-polymerized. The fluorophore exhibited an acrylamide monomer group, which allowed the covalent attachment to the polymer matrix. It was shown that the rhodamine-based reference dye was insensitive to the analyte and to changes in pH of the analyte solution. The physically entrapped lucigenin leached three times more from the nanoparticles than the covalently immobilized reference dye during 24 hours of dialysis. The major part of lucigenin was washed out during the first hour probably due to loosely attached dye molecules close to the surface of the particles. Leaching of the reference dye was significantly reduced by co-polymerization.

The response to chloride ions was determined for lucigenin in solution and for lucigenin embedded into NPs. A decrease of K_{SV} was observed upon incorporation of the fluorophore inside the NPs. The sensitivity of the fluorescent NPs was five times smaller than that of the dissolved dye. This was probably due to the lower diffusion coefficient of Cl^- inside the polymer matrix and/or due to the hindered the access to the dye inside the particles. Molecules located deep inside the polymer, which were even inaccessible to the analyte, could still show unaffected fluorescence intensity. The dynamic fluorescence quenching of lucigenin was also observed for other anions, i.e. bromide, iodide and isothiocyanate. The Stern-Volmer constant K_{SV} increased with increasing atomic number in the row Cl^- , Br^- and I^- . Isothiocyanate ions gave a higher quenching constant than bromide ions due to their better polarizability. However, these interfering ions usually occur in low concentrations inside biological samples.

For dissolved lucigenin the cross-sensitivity to pH led to a decrease in fluorescence intensity in absence of chloride ions. The intensity decreased about 33% with

pH rising from 4.9 to 8.1, while the intensity was not affected in the presence of 12 mM chloride. In contrast, lucigenin immobilized inside the poly(acrylamide) NPs exhibited a decrease in fluorescence intensity of about 58% independently from the chloride concentration. Consequently, in solution Cl^- more effectively quenched the fluorescence of lucigenin than OH^- ($K_{SV}(\text{Cl}^-) \gg K_{SV}(\text{OH}^-)$). In contrast, K_{SV} for chloride was lower than K_{SV} for hydroxyl ions, when lucigenin was incorporated inside the NPs. The inversion of the sensitivities was supposed to originate from the higher diffusion coefficients of hydroxyl ions inside the polymer matrix compared to chloride ions. The pH-sensitivity of lucigenin is problematic for application in biosamples, since the pH inside the sample may change during an experiment.

The signal changes due to interaction with protein were reduced upon incorporation of lucigenin and **R3** inside the polymer matrix of the NPs. At a BSA concentration of 5 wt.-% the fluorescence of dissolved lucigenin was quenched by 70% and that of **R3** by 40%. The polymer matrix of the NPs prevented the diffusion of large bio-molecules such as BSA into the particle interior. Hence, the undesired interaction of the fluorophores with the protein and the resulting fluorescence quenching was reduced. The still observable decrease in fluorescence intensity by 10 - 20% might originate from dye molecules located at the surface of the NPs. These dye molecules were probably not hindered to interact with the BSA.

In contrast, the diffusion of small molecules through the polymer network of the nanoparticle was still possible, although their diffusion was hindered. This was on the one hand indicated by the smaller chloride quenching constant of immobilized lucigenin compared to the quenching constant in solution. On the other hand it was shown for the oxidation of lucigenin by hydrogen peroxide. Lucigenin was decomposed probably to its corresponding acridone derivative accompanied by a decrease in fluorescence intensity at 500 nm. The signal decrease of the fluorescent NPs was only slightly lower than the signal decrease of lucigenin in solution. This leads to the conclusion that the access of hydrogen peroxide to the embedded dye is slightly hindered, but not completely prevented.

The transfection substance lipofectamine was employed to introduce the fluorescent poly(acrylamide) NPs into living CHO cells and mouse fibroblasts. As already

described on page 24 lipofectamine formed small vesicles containing the particles, which were able to penetrate through the cell membrane by phagocytosis. Confocal fluorescence microscopy was used to locate the NPs inside the transfected cells. The loading of the cells was effective and the particles were distributed in the cytoplasm. The appearance of larger fluorescent spots in the cytoplasm indicated that a certain part of the particles was most probably located in the endosomes and lysosomes, respectively. This was attributed to the method of transfection leading to encapsulation of the NPs inside cellular organelles. The superfusion of the cells with buffers of varying chloride concentration gave the expected fluorescence signal changes. However, tributyltin(IV)chloride and the ionophore nigericin were needed to render the cell membrane permeable for chloride ions and to achieve an ion exchange. This ion exchange was necessary to fix the pH inside the cell to the pH of the superfusing solutions. Hence, an influence of changing pH on the fluorescence of lucigenin was prevented. The proteins and enzymes in the biological matrix seemed to leave the NPs unaffected, whereas the excitation light source caused damage on the cells and the lucigenin inside the NPs.

4.4 pH-Sensitive Nanoparticles

The fluorescent indicator *N*-allyl-4-(*N*-methylpiperazinyl)-1,8-naphthalimide (N2) was chosen as the most suitable pH-indicator dye for bioanalytical applications, due to the following advantageous properties:

- pK_a in the relevant near neutral range
- absorption and emission in the visible spectral range
- large Stoke's shift
- large signal changes
- high quantum yield
- enhanced (photo)stability
- polymerizable moiety
- full reversibility
- suitable dynamic range

Unfortunately, the solubility of **N2** in water was poor so that the dye needed to be dissolved in methanol and diluted with water to perform experiments in solution. For the preparation of nanoparticles the monomers AAm and MBAAm acted as solubilizers in the aqueous phase. The pH-indicator was copolymerized together with the rhodamine-based reference dye **R3** to give fluorescent poly(acrylamide) nanoparticles. During 24 hours of dialysis the fluorescence intensity of **N2** dropped by 18% and thus was only half the leaching observed for the physically entrapped lucigenin. The decrease in fluorescence intensity is attributed to leaching of unreacted dye molecules and to diffusion of NPs ≤ 2 nm through the dialysis membrane.

Within the pH-range from 4.0 to 9.0 the signal change of the dye-containing NPs was only 70% of that observed for **N2** in solution. Like for the chloride-sensitive NPs the diffusion of the analyte through the polymer network to react with the fluorophores inside the NPs was assumed to be hindered. Thus, protonated dye molecules deep inside the particle could still contribute to the fluorescence, which would also explain the higher pK_a of the immobilized pH-indicator. The dynamic range of **N2** was determined to be between pH 5.0 and 8.2 and is in the adequate range for physiological measurements. Although the dynamic range did not exceed 3 pH units it was broader than that of the other investigated fluorophores. The naphthalimide-based indicator exhibited significant cross-sensitivity to ionic strength. An increase of the pK_a of about 0.7 units was observed with rising sodium chloride concentration from 0 to 200 mM sodium chloride in the analyte solution.

The protection of the co-polymerized fluorophores against interaction with large bio-molecules such as BSA was evaluated. The fluorescence enhancement of dissolved **N2** upon exposure to BSA may be ascribed to the microenvironment of the protein. Probably the dye attached to the protein and a fluorescence change was caused either by protonation or due to the modified polarity. This was nearly completely avoided by the incorporation of the pH-indicator inside the nanoparticles. However, a pH-calibration in presence of 1 wt.-% BSA gave a linear correlation and thus determination of a pK_a -value was not possible.

Compared to fluorescein, **N2** exhibited better photostability. In solution the dye was not affected at all by irradiation with light of high intensity (bleaching). How-

ever, immobilization of the dye inside particles resulted in enhanced bleaching, caused by the lower mobility of the fluorophore molecules.

4.5 Functionalized Nanoparticles

The functionalization of NPs was carried out in order to achieve a positive ζ -potential that is supposed to enhance the cellular uptake of the NPs. For the non-functionalized poly(acrylamide) (PAAm) NPs a constantly neutral ζ -potential was measured and thus it was assumed that the NPs repelled each other by steric interaction to form stable colloidal solutions. The coating with PEI seemed to prevent any repulsion between the particles and large aggregates were formed. The attractive forces between the particles became higher than the repulsive forces from electrostatic or steric interactions. Even in acidic media in which the protonation of PEI should provide a high number of positively charged ammonium groups, a disaggregation could not be observed. Attempts to coat the NPs with PEI of low molecular weight were not successful, because the PEI was washed out during purification by dialysis. The non-covalent coating of the NPs with PEI requires strong electrostatic interactions between a charged particle surface and the oppositely charged PEI. As the PAAm NPs did not possess any surface charge, the attraction between the particles and the protonated PEI was not strong enough to achieve a permanent coating.

Since the coating of the non-functionalized PAAm NPs was unsuccessful, the polymer matrix had to be changed. The cross-linked poly(*N,N*-diethyl aminoethyl methacrylate) (PDEAMA) NPs obtained by a surfactant-free emulsion polymerization were larger in size than the nanoparticles obtained by inverse microemulsion polymerization. The protonation of the diethylamino groups of PDEAMA was intended to enable both a pH-induced swelling of the particles and a positive surface potential. Indeed, a drastically volume change of the NPs was observed at a pH of 7, which corresponded to the pK_a of the diethylamino function. At acidic pH the particle diameters as well as the polydispersities increased. The higher PDI was ascribed to the appearance of a major fraction of very small NPs additionally to the swollen particles. This would imply the disaggregation or even dissolution of

larger nanoparticle assemblies rather than swelling of the NPs. The repulsion in these assemblies might have become stronger with increasing protonation of the polymer leading to larger aggregate diameters and finally to disaggregation. The examination of the incorporated fluorophores revealed an unexpected increase in fluorescence intensity upon aggregation of the NPs at basic conditions.

In order to prevent pH-induced swelling but to maintain a positively charged hydrophilic polymer matrix, poly(*N,N*-dimethyl aminopropyl acrylamide) (PDMAPA) cross-linked with the more rigid *N,N'*-methylene bisacrylamide (compared to poly(ethyleneglycol) dimethacrylate)) was used. As mentioned for PDEAMA, protonation of the aliphatic amino group at acidic pH is expected to cause a positive ζ -potential of the final particles. Around the PDMAPA-core a neutral shell made of cross-linked poly(acrylamide) was polymerized in order to reduce the cytotoxicity of quaternary amino compounds. The reference fluorophore **R3** was co-polymerized in the particle core and the pH-indicator dye was immobilized in the neutral shell. The core-shell composition was realized by a two-stage inverse emulsion polymerization. In the first step the core of the NPs was polymerized and in the second stage the shell monomers were added to the emulsion. It was expected that the added aqueous solution containing the shell monomers was emulsified by the already existing micelles and thus assembled around the nanoparticle core. However, it could not be excluded that NPs were formed consisting only of the shell material and that some of the core particles were not functionalized with a shell. The low yield of isolated polymeric NPs (20 - 50%) after polymerization corroborate this assumption.

The hydrodynamic diameter of the core-shell NPs slightly decreased from 44 nm at basic pH to 33 nm at acidic pH of the suspension. Due to protonation of PDMAPA, the ζ -potential of the nanoparticle suspensions increased from +11 mV to +30 mV and at a pH of 6.5, which corresponds to the pK_a of PDMAPA, the ζ -potential showed a steep increase. The fluorescence excitation and emission spectra of the co-polymerized dyes showed little changes in the intensity maxima compared to the dyes inside the PAAm NPs. The response of the core-shell NPs to increasing pH was significantly lower. The overall signal change was only 30% and thus more than

two times lower than the signal change in the PAAm NPs. The plot of the fluorescence intensity against the pH gave an almost linear dependency, which rendered the determination of the pK_a of **N2** inside the core-shell NPs impossible.

5

Summary and Outlook

In this work the synthesis and characterization of small, stable and fluorescent poly-(acrylamide) NPs for sensing of chloride ions and pH is presented. The NPs were prepared by inverse microemulsion polymerization and characterized regarding their structural and fluorescence properties. It was shown that even little amounts of incorporated dye and the choice of the initiator can influence the yield of the polymerization and the particle size/morphology. Nearly all of the described NPs formed stable colloidal solutions in water and possessed a small diameter, sufficient monodispersity and a neutral surface-potential. Two different kinds of sensor particles were prepared: chloride-sensitive NPs with a physically entrapped indicator fluorophore and pH-sensitive NPs with a covalently bound indicator dye. It was shown that covalent attachment of the dyes to the polymer backbone minimized the leaching out of the NPs. The co-polymerization of a reference dye enabled ratio-metric measurements in suspensions with both types of nanosensors. The nanosensors showed good response to the respective analyte, although the sensitivity was reduced by incorporation of the fluorophores inside the polymer matrix. The polymer matrix protected the fluorophores from undesired interaction with proteins and at the same time allowed small ionic analytes to pass through the polymer. It was mandatory to minimize these analyte-unspecific reactions to apply the NPs inside cells. The chloride nanosensors were transferred into living cells and their response was evaluated using fluorescence microscopy. After transfection of the cells, the NPs were located partially in small cellular organelles (endosomes) as well as in the

cytosol.

In order to enhance the cellular uptake and to force the endosomal escape of the NPs, different methods of functionalization were evaluated. It appeared that coating of the pAAm NPs with polycationic polymers and the synthesis of NPs showing pH-induced swelling were not useful to achieve the expected properties. Therefore, novel core-shell NPs with pH-independent size and a positive ζ -potential were developed. Both, a pH-indicator fluorophore and a reference dye were co-polymerized to enable ratiometric pH-sensing. The signal magnitude in suspension was not as good as for the poly(acrylamide) NPs, although a clear correlation between the fluorescence intensity and the pH was obtained.

In future experiments the uptake of the positively charged core-shell particles by different cell types has to be evaluated and compared to the non-functionalized NPs. In this manner it can be evaluated, if the particles with a positive ζ -potential are more efficiently internalized by the cells. Furthermore, the cytotoxicity of the new sensor materials has to be assessed in order to evaluate the protective effect of the neutral poly(acrylamide) shell. Finally, it is necessary to know in which compartments of the cell the NPs are distributed, i.e whether or not the proposed endosomal escape actually takes place.

6

Zusammenfassung und Ausblick

In der Arbeit wird die Synthese und Charakterisierung von fluoreszierenden Poly(acrylamid)-Nanopartikeln zur Bestimmung von Chloridionen und des pH-Wertes vorgestellt. Die Poly(acrylamid)-Nanopartikel wurden mittels inverser Mikroemulsionspolymerisation hergestellt und hinsichtlich ihrer Struktur und Fluoreszenzeigenschaften untersucht. Es konnte gezeigt werden, dass die Immobilisierung selbst kleiner Farbstoffmengen und die Wahl des Initiators die Polymerausbeute und die Partikelgröße bzw. -morphologie beeinflussen. Fast alle hergestellten Nanopartikel bildeten stabile kolloidale Lösungen in Wasser und besaßen geringe Partikeldurchmesser, relativ enge Größenverteilungen und negative Oberflächenpotentiale. Die physikalische Einbettung eines Indikatorfarbstoffs für Chloridionen oder die kovalente Anbindung des pH-Indikators lieferte zwei unterschiedliche Sensortypen. Auf diese Weise wurde bestätigt, dass die kovalente, chemische Bindung an das Polymer ein Auswaschen des Farbstoffs minimiert. Die Copolymerisation eines Referenzfarbstoffs ermöglichte die ratiometrische Analytbestimmung mit beiden Nanopartikeltypen. Im Vergleich zur Analytbestimmung in Lösung, wurde jedoch die Sensitivität der Indikatorfarbstoffe durch das Einbetten in die Polymermatrix reduziert. Für eine intrazelluläre Anwendung der Nanopartikel war es notwendig analytunspezifische Reaktionen mit Biomolekülen zu minimieren. Die Immobilisierung der Farbstoffe in den Nanopartikeln schützte vor unerwünschten Wechselwirkungen mit Proteinen, erlaubte aber gleichzeitig kleinen, ionischen Analyten in die Polymermatrix zu diffundieren. Die Nanosensoren zu Chloridbestimmung wurden in

lebende Zellen eingeschleust und ihr Ansprechverhalten mittels Fluoreszenzmikroskopie untersucht. Durch die Art und Weise der Zelltransfektion befanden sich die Nanopartikel nach Aufnahme sowohl in kleinen Zellorganellen (Endosomen) als auch im Zytosol.

Es wurden verschiedene Methoden der Funktionalisierung untersucht, um die Aufnahme der Nanopartikel durch die Zellen und die "endosomale Freisetzung" zu verbessern. Es stellte sich heraus, dass die Beschichtung der Poly(acrylamid)-Nanopartikel mit polykationischen Polymeren und die Synthese quellfähiger Nanopartikel nicht geeignet waren die erwarteten Eigenschaften zu erzeugen. Daher wurden neuartige "Core-Shell"-Nanopartikel hergestellt, welche eine pH-unabhängige Größe und ein positives Oberflächenpotential besitzen. Um eine ratiometrische pH-Bestimmung zu gewährleisten wurden ein pH-Indikatorfarbstoff und ein Referenzfarbstoff copolymerisiert. Die Sensitivität der funktionalisierten Partikel in Suspension war nicht so hoch wie die der Poly(acrylamid)-Nanopartikel, jedoch konnte ein linearer Zusammenhang zwischen Fluoreszenzintensität und pH-Wert festgestellt werden.

Die Aufnahme der funktionalisierten "Core-Shell"-Nanopartikel durch verschiedene Zelltypen und der Vergleich mit den Poly(acrylamid)-Nanopartikel muss in weiteren Experimenten untersucht werden. Auf diese Weise kann geprüft werden, ob die Zellen die Partikel mit positivem Zetapotential besser aufnehmen. Des Weiteren muss die Zytotoxizität beider Nanopartikeltypen bestimmt werden, um die schützende Funktion der neutralen Poly(acrylamid)-Hülle zu überprüfen. Abschließend muss untersucht werden wie sich die funktionalisierten Partikel in der Zelle verteilen um den vorgeschlagenen Mechanismus der "Endosomalen Freisetzung" zu verifizieren.

7

Experimental

7.1 Apparatus and Materials

For preparation of aqueous solutions double-deionized water (conductivity $\leq 0.055 \mu\text{S cm}^{-1}$) was used. Phosphate buffer solutions were prepared by mixing 67 mM aqueous solutions of sodium dihydrogen phosphate hydrate and disodium hydrogen phosphate dihydrate until the desired pH was achieved. Solutions with $\text{pH} \leq 4.0$ or $\text{pH} \geq 9.0$ were adjusted with 0.1 M HCl or NaOH, respectively. The pH was controlled with a digital pH meter from Hanna Instruments and calibrated at $(25 \pm 1) ^\circ\text{C}$ with standard buffers pH 4.0 and pH 7.0 (MERCK).

The membranes for ultrafiltration were Whatmann Anodisc 47 filters with a pore size of 20 nm and a diameter of 47 mm. Dialysis was performed with membranes made of regenerated cellulose (molecular-weight-cut-off 8.000-10.000 Da) from ROTH against 67 mM phosphate buffer solutions (pH 7.2).

The UV/VIS spectra of the dye solutions were recorded in a 10 mm quartz cuvette with a PERKIN ELMER Lambda 16 spectrometer at room temperature. All fluorescence spectra were recorded in a 10 mm quartz cuvette on a Fluorolog 3 from JOBIN YVON-SPEX at a temperature of $(25 \pm 1) ^\circ\text{C}$. The fluorescence quantum yields were determined on a LS 50B from PERKIN ELMER using quinine sulfate in a 0.1 N H_2SO_4 solution.

All measurements of lucigenin and *N*-(4-(sulforhodaminyl Q5 sulfonamido)butyl) acrylamide (**R3**) in solution and inside the NPs were carried out in a 67 mM

phosphate buffer of pH 7.2. The wavelengths for excitation of lucigenin and the rhodamine reference **R3** in solution were 368 nm and 583 nm, respectively. Both lucigenin and **R3** inside the chloride-sensitive nanoparticles were excited at 360 nm, if not denoted otherwise. For characterization of the NPs with fluorescence spectroscopy, 2.0 mL of a dialyzed particle suspension was filled in a cuvette and the analyte concentration was adjusted by adding different quantities of a 1 molar aqueous analyte solution.

The excitation wavelength for the pH-indicator **N2** in solution and for the nanoparticles was 390 nm. The reference **R3** inside the pH-sensitive NPs was excited at 543 nm, which is the wavelength of the He/Ne-laser line. The nanoparticle suspensions of different pH were prepared by adding 0.2 mL of a stock suspension (5 mg NPs/ml dist. water) to a cuvette containing 2.0 mL of a phosphate buffer solution with the desired pH. The pH inside the cuvette upon addition of the nanoparticle suspension was controlled with a digital pH meter.

Confocal imaging was performed with a Zeiss laser-scanning microscope (LSM 510, CARL ZEISS, Göttingen, Germany) using a Zeiss C Apochromat 63x (NA 1.20) water immersion objective. Lucigenin was excited with the Ar⁺-laser 458 nm line and the reference dye **R3** with the He/Ne-laser 543 nm line. Fluorescence was recorded with a 505-550 nm band pass (lucigenin) and a 560 nm long pass filter (**R3**).

The particle size and the ζ -potential were determined by dynamic light scattering (DLS) with a ZetaSizer Nano ZS from MALVERN INSTR. (if not denoted otherwise) in disposable polystyrene cuvettes (except the microemulsions, which were measured in a quartz cuvette) using a laser beam at 633 nm and a scattering angle of 173°. For the measurements 10 mM phosphate buffer solutions filtered through a syringe membrane filter of 5 μ m pore size were used. The particle concentration was between 0.5 and 1 mg/ml buffer solution.

The specific surface area was measured *via* nitrogen adsorption using an Autosorb 1 from QUANTACHROME (Odelzhausen, Germany) and evaluated via multi-point BET adsorption isotherms. The densities were determined with helium pycnometry at the Autosorb 1 from QUANTACHROME.

The NMR spectra of the solutions were taken on a AC 250 and AC 400, respectively from BRUKER. Solid-State NMR measurements were carried out on a BRUKER AMX 400 at 300 MHz proton frequency utilizing a BRUKER 3.2 mm HFX probe under MAS conditions and a spinning rate of 5 kHz. The chemical shifts (δ) are given in parts per million (ppm) and the peak assignments are abbreviated as the following: s: singlet, d: doublet, dd: double doublet, m: multiplet. The mass spectra were recorded at a MAT SSQ 710 from FINNIGAN and at a TRIO 2000 from FISIONS. The ionization methods were fast atom bombardment (FAB), electron impact ionization (EI) and direct electron impact (DEI). Elemental analysis was performed using a combustion automat CHNS-932 from LECO. For SEM studies, one droplet of nanoparticle suspension on a mica surface was lyophilized and covered with gold. The images were obtained with the SEM equipment LEO-1530 VP Gemini (LEO, Oberkochen, Germany) operating at 6.0 - 8.0 kV.

The chloride-sensitive compound 9-methyl-*N*-methylacridinium methylsulfate was synthesized according to the literature.⁷³ All other chemicals were purchased from FLUKA, SIGMA-ALDRICH and POLYSCIENCES INC. and used without further purification. Chemical for synthesis were of analytic reagent grade. Prior to use, AIBN was purified by recrystallization from ethanol at 50 °C. The solvents obtained from ROTH were of HPLC grade and used without further purification or drying, if not denoted otherwise. Thin layer chromatography was performed using silica gel cards labeled with fluorescence indicator (254 nm) from FLUKA. The stationary phase for column chromatography was silica gel 60 from FLUKA.

7.2 Procedures

7.2.1 Synthesis of the Polymerizable Dyes

Synthesis of *N*-(4-aminobutyl) sulforhodamine Q5 sulfonamide (R2)

In a 25 mL round bottom vessel, 0.15 g (0.3 mmol) of sulforhodamine Q5 acid fluoride were first dried in vacuum and afterwards dissolved under argon atmosphere in 12 mL of dry acetonitrile. An excess of 1 g (11.3 mmol) of 1,4-diaminobutane

(dried over K_2CO_3) was added slowly with a syringe and the reaction was stirred at room temperature for 20 h. The reaction progress was controlled using TLC (silicagel) with methanol as the eluent. When the reaction was finished, 10 mL of acetone were added to the mixture, the resulting violet solid was filtered and washed thoroughly with acetone. The substance was dried *in vacuo*. Yield: deep violet powder 85%.

MS (FAB): $m/z = 625$ (base peak) $[M+1]$.

1H -NMR (400 MHz, DMSO- d_6): δ (ppm) = 8.40 (1H, s), 7.91 (1H, dd, $^3J_{H,H} = 8$ Hz), 7.40 (1H, d, $^3J_{H,H} = 8$ Hz), 6.96 (2H, d, $^3J_{H,H} = 8$ Hz), 6.86 (2H, d, $^3J_{H,H} = 8$ Hz), 3.58 (4H, m), 3.19 (6H, s), 2.99 (4H, m), 2.86 (2H, m), 2.51 (2H, m), 2.02 (4H, m), 1.38 (4H, m).

^{13}C -NMR (100 MHz, DMSO- d_6): δ (ppm) = 157.4, 154.1, 152.4, 148.4, 142.1, 133.8, 131.2, 126.9, 126.2, 113.7, 112.9, 106.2, 51.3, 43.0, 41.2, 31.1, 29.9, 27.1, 20.0, 19.7.

Synthesis of *N*-(4-(sulforhodaminyll Q5 sulfonamido)butyl) acrylamide (R3)

In a 25 mL round bottom vessel, 80 mg (0.1 mmol) of **R2** and 1 mg ($9 \cdot 10^{-3}$ mmol) of hydroquinone were first dried in vacuum and afterwards dissolved under argon atmosphere in 4 mL of dry acetonitrile. To the stirred solution, 50 μ L of dry TEA and then a solution of 25 μ L (0.3 mmol) of acryloyl chloride in 100 μ L of dry acetonitrile were added slowly at 0 °C. The reaction was stirred for 4 hours at 45 °C and afterwards at room temperature over night. The conversion was controlled using TLC with methanol as the eluent and the procedure of addition of TEA and acryloyl chloride was repeated until the major part of **R2** was converted into the product. When the reaction was finished 70 mL of dichloromethane were added and the mixture was washed with distilled water four times. After drying the separated organic phase over $MgSO_4$ the solvent was evaporated and the crude product was purified by column chromatography with methanol as eluent. Yield: deep violet crystals 58%.

MS (FAB): $m/z = 257$ (base peak), 679 (90%) $[M+1]$.

Elemental analysis calculated for $C_{34}H_{38}N_4O_7S_2 \cdot 3H_2O$ (732.9): C 55.70, H 6.05, N 7.65, found: C 56.03, H 5.98, N 7.36.

$^1\text{H-NMR}$ (400 MHz, DMSO- d_6): δ (ppm) = 8.42 (1H, s), 7.92 (1H, dd, $^3J_{H,H} = 8$ Hz), 7.40 (1H, d, $^3J_{H,H} = 8$ Hz), 6.97 (2H, d, $^3J_{H,H} = 8$ Hz), 6.86 (2H, d, $^3J_{H,H} = 8$ Hz), 6.17 (1H, dd), 6.07 (1H, d), 5.54 (1H, d, $^3J_{H,H} = 8$ Hz), 3.58 (4H, m), 3.19 (6H, s), 3.08 (2H, m), 3.00 (4H, m), 2.88 (2H, m), 2.02 (4H, m), 1.43 (4H, s).

$^{13}\text{C-NMR}$ (100 MHz, DMSO- d_6): δ (ppm) = 165.1, 157.4, 154.1 (2C), 152.4 (2C), 148.5, 142.0, 133.8, 132.3, 131.4, 131.2 (2C), 127.0, 126.3, 125.3, 122.6, 113.7 (2C), 112.9 (2C), 106.2, 51.3 (2C), 42.7, 40.2 (2C), 38.6, 27.0, 26.6, 20.0 (2C), 19.7 (2C).

Synthesis of *N*-acryloyl-5-aminofluorescein (F2)

The synthesis was carried out according to Ferguson *et al.*⁶² In a 100 mL round bottom vessel 180 mg (0.5 mmol) of 5-aminofluorescein were dissolved in 50 mL of dry acetone (freshly distilled over CaCl_2) at room temperature. Under extensive stirring 50 μL (0.6 mmol) of acryloyl chloride were added slowly *via* a syringe. The solution turned red and the orange product precipitated. The reaction was allowed to stir for 3 hours in the dark and afterwards the orange precipitate was filtered. The product was washed three times with little acetone and twice with dichloromethane. Yield: orange powder 85%.

mp: 280 °C.

MS (FAB): $m/z = 402$ (base peak) $[\text{M}+1]$.

$^1\text{H-NMR}$ (400 MHz, DMSO- d_6): δ (ppm) = 10.83 (1H, s), 8.45 (1H, s), 7.96 (1H, d, $^3J_{H,H} = 8$ Hz), 7.23 (1H, d, $^3J_{H,H} = 8$ Hz), 6.76 (2H, s), 6.67 - 6.51 (5H, m), 6.34 (1H, d, $^3J_{H,H,trans} = 18$ Hz), 5.82 (1H, d, $^3J_{H,H,cis} = 10$ Hz), 4.20 (-OH, s).

$^{13}\text{C-NMR}$ (400 MHz, DMSO- d_6): δ (ppm) = 168.91, 164.28, 160.77 (2C), 152.83 (2C), 141.17 (2C), 131.95 (2C), 129.77 (2C), 128.21, 127.75, 126.80, 125.33, 114.81, 113.62 (2C), 110.63 (2C), 102.71 (2C).

Synthesis of *N*-allyl-4-bromo-1,8-naphthalimide

The reaction was carried out according to the literature.⁶⁴ 1 g (3.4 mmol) of 4-Bromo-1,8-naphthalic anhydride was suspended in 25 mL of absolute ethanol and heated up to 70 °C. Upon addition of 330 μL (4.4 mmol) of allyl amine the reaction mixture turned brown. Afterwards the mixture was heated under reflux until the educts

were completely dissolved. After 30 minutes of stirring the product precipitated and the reaction was refluxed for further 2 hours. The reaction was cooled to room temperature and the solid product was filtered, washed with ethanol and dried *in vacuo*. The product was purified by recrystallization from ethanol. Yield: pale brown needles 92%.

mp: 152 °C.

MS (EI): $m/z = 315$ (20%) [$M^{\bullet+}$], 300 (base peak) [M-15].

Elemental analysis calculated for $C_{15}H_{10}N_1O_2Br$ (316.2): C 57.2, H 3.2, N 4.5, found: C 57.1, H 3.1, N 4.4.

1H -NMR (400 MHz, $CDCl_3$): δ (ppm) = 8.65 (1H, dd, $^3J_{H,H} = 7$ Hz, $^4J_{H,H} = 1$ Hz), 8.56 (1H, dd, $^3J_{H,H} = 8$ Hz, $^4J_{H,H} = 1$ Hz), 8.41 (1H, d, $^3J_{H,H} = 8$ Hz), 8.03 (1H, d, $^3J_{H,H} = 8$ Hz), 7.84 (1H, dd, $^3J_{H,H} = 8$ Hz, 7 Hz), 6.01 (1H, m), 5.34 (1H, dd, $^3J_{H,H,trans} = 17$ Hz, $^2J_{H,H} = 1$ Hz), 5.23 (1H, dd, $^3J_{H,H,cis} = 10$ Hz, $^2J_{H,H} = 1$ Hz), 4.80 (2H, m).

^{13}C -NMR (100 MHz, $CDCl_3$): δ (ppm) = 163.3 (2C), 133.3, 132.1, 132.0, 131.3, 131.1, 130.6, 130.3, 129.0, 128.1, 123.0, 122.2, 117.9, 42.5.

Synthesis of *N*-allyl-4-piperazinyl-1,8-naphthalimide (N1)

According to the literature⁶⁴, 950 mg (3 mmol) of *N*-allyl-4-bromo-1,8-naphthalimide, 780 mg (9 mmol) of piperazine and 1 mg ($9 \cdot 10^{-3}$ mmol) of hydroquinone were suspended in 20 mL of 2-methoxyethanol and refluxed for 2 hours at 140 °C until the educts were dissolved. The product was precipitated by pouring the reaction solution into 100 mL of an ice-water mixture. The yellow precipitate was filtered, washed with 20 mL of ethanol and dried *in vacuo*. The product was further purified by recrystallization from ethanol. Yield: yellow needles 93%.

mp: 171 °C.

MS (DEI): $m/z = 321$ [$M^{\bullet+}$], 279 (base peak) [M-42].

Elemental analysis calculated for $C_{19}H_{19}N_3O_2$ (321.4): C 71.01, H 5.96, N 13.08, found: C 71.00, H 5.78, N 12.93.

1H -NMR (400 MHz, CD_2Cl_2): δ (ppm) = 8.50 (1H, d, $^3J_{H,H} = 10$ Hz), 8.45 (1H, d, $^3J_{H,H} = 8$ Hz), 8.43 (1H, d, $^3J_{H,H} = 9$ Hz), 7.65 - 7.69 (1H, m), 7.19 (1H, d, $^3J_{H,H} = 8$ Hz), 5.93 - 6.03 (1H, m), 5.23 (1H, dd, $^3J_{H,H,trans} = 17$ Hz, $^2J_{H,H} = 3$ Hz), 5.15 (1H, dd,

$^3J_{H,H,cis} = 10$ Hz, $^2J_{H,H} = 1$ Hz), 4.72 - 4.74 (2H, m), 3.20-3.22 (4H, m), 3.13 - 3.15 (4H, m).

$^{13}\text{C-NMR}$ (100 MHz, CD_2Cl_2): δ (ppm) = 164.3, 163.8, 157.0, 133.3, 132.7, 131.2, 130.8, 130.3, 126.6, 125.8, 123.5, 116.8, 116.7, 115.2, 54.9 (2 C), 46.6 (2 C), 42.4.

Synthesis of *N*-allyl-4-(*N*-methylpiperazinyl)-1,8-naphthalimide (N2)

470 mg (1.5 mmol) of *N*-Allyl-4-bromo-1,8-naphthalimide, 900 mg (9 mmol) of methyl piperazine and 1 mg ($9 \cdot 10^{-3}$ mmol) of hydroquinone were suspended in 10 mL of 2-methoxyethanol and refluxed for 4 hours at 140 °C until the educts were dissolved. The conversion was controlled using TLC with dichloromethane/methanol 5:1 (v/v) as the eluent. The product was precipitated by pouring the dark yellow solution into 50 mL of an ice-water mixture. The yellow precipitate was filtered, washed with 20 mL of ethanol and dried *in vacuo*. The product was further purified by recrystallization from ethanol. Yield: yellow needles 48%.

mp: 166 °C.

MS (EI): $m/z = 335$ [M].

Elemental analysis calculated for $\text{C}_{20}\text{H}_{21}\text{N}_3\text{O}_2$ (335.4): C 71.62, H 6.31, N 12.52, found: C 71.56, H 6.05, N 12.42.

$^1\text{H-NMR}$ (250 MHz, CDCl_3): δ (ppm) = 8.55 (1H, d, $^3J_{H,H} = 7$ Hz), 8.49 (1H, d, $^3J_{H,H} = 8$ Hz), 8.39 (1H, d, $^3J_{H,H} = 8$ Hz), 7.66 (1H, t, $^3J_{H,H} = 8$ Hz), 7.19 (1H, d, $^3J_{H,H} = 8$ Hz), 5.98 (1H, m), 5.28 (1H, dd, $^3J_{H,H,trans} = 17$ Hz, $^2J_{H,H} = 2$ Hz), 5.17 (1H, dd, $^3J_{H,H,cis} = 10$ Hz, $^2J_{H,H} = 2$ Hz), 4.77 (2H, d, $^3J_{H,H} = 6$ Hz), 3.29 (4H, m), 2.73 (4H, m), 2.42 (3H, s).

$^{13}\text{C-NMR}$ (63 MHz, CDCl_3): δ (ppm) = 164.2, 163.7, 156.0, 132.7, 132.4, 131.2, 130.3, 129.9, 126.1, 125.6, 123.1, 117.3, 116.5, 115.0, 55.1 (2C), 53.0 (2C), 46.1, 42.2.

7.2.2 Preparation of the Nanoparticles

Poly(acrylamide) Nanoparticles

Poly(acrylamide) nanoparticles were prepared by inverse microemulsion polymerization as described by Clark *et al.*²³ A solution of 3.08 g of Brij 30 and 1.59 g (3.6 mmol) of AOT in 43 mL of hexane or heptane was purged with argon for 1 h. To

this mixture, 2 mL of a solution consisting of 0.4 g (2.6 mmol) of *N,N'*-methylene bisacrylamide and 1.85 g (26 mmol) of acrylamide in 4.5 mL of phosphate buffer (5 mM, pH 7.2) was added slowly under extensive stirring and purging with argon. For preparation of the chloride-sensitive NPs 140 μL of a buffered $1 \cdot 10^{-2}$ M solution of lucigenin and 120 μL of a buffered $7.4 \cdot 10^{-4}$ M solution of **R3** were added. To obtain pH-sensitive NPs 0.5 mg of **N2** and 0.1 mg of **R3** were dissolved in 2 mL of the monomer solution before adding it to the organic phase ($m_{\text{dyes}}/m_{\text{monomer}} \approx 1:1000$). The volume of the aqueous phase was held constant by adding 260 μL of plain buffer to the microemulsion. Then the polymerization was started with either:

- 24 μL of an aqueous APS solution (20 wt.-% APS) and 12 μL of TEMED at room temperature or
- 30 mg of solid AIBN (2.5 mol-% of the double bonds) at 70 °C or
- 47 mg of solid AAPH (2.5 mol-% of the double bonds) at 70 °C.

To finish the polymerization process, the emulsion was stirred for 2 h at the respective temperature and at room temperature overnight. Then the organic solvent was removed by evaporation, and the cloudy residue suspended in 100 mL of ethanol. This suspension was filtered with a Millipore system using filter membranes with pore size of 20 nm. For removal of unreacted monomers, remaining surfactants, and dyes, the particles were washed with 300 mL of ethanol until the filtrate was colorless. If filtration was not possible, the suspension was centrifuged and washed four times with each 75 mL of ethanol. The particles were dried *in vacuo* and the chloride-sensitive NPs were further purified *via* dialysis of a nanoparticle suspension (20 mg/10 mL buffer) against 1 L of phosphate buffer solution (67 mM, pH 7.2) for 24 h.

Coating of Poly(acrylamide) NPs with Poly(ethyleneimine)

Coating of the **N2** and **R3** containing poly(acrylamide) NPs was carried out similar to the procedure reported for coating of silica NPs.⁷¹ The coating solution consisted of varying amounts of either high molecular weight (10 kDa) or low molecular weight (600 Da) branched poly(ethyleneimine) (PEI) in 10 mL of a 25 mM sodium

acetate buffer solution. Suspensions of each 50 mg NPs in 4 mL of a 25 mM sodium acetate buffer were added dropwise and under stirring to the coating solution. After stirring the mixture for 10 minutes the residual PEI was removed by extensive dialysis of the NPs against 1 L of dist. water until neutral pH was achieved. The coated NPs were precipitated by subsequent dialysis against ethanol, collected *via* centrifugation and dried *in vacuo*.

Poly(*N,N*-diethyl-2-aminoethyl methacrylate) Nanoparticles

The nanoparticles were prepared similar to the method from Hu *et. al.*⁷² In a round bottom flask 1 mL of *N,N*-diethyl-2-aminoethyl methacrylate and 10 μ L of poly-(ethyleneglycol) dimethacrylate were emulgated by extensive stirring in 9 mL of distilled water. The emulsion was heated up to 70 °C and equilibrated at this temperature for 15 minutes. To start the polymerization 50 μ L of an aqueous APS solution (20 wt.-% APS) was added to the mixture. After stirring for three hours at 70 °C the cloudy emulsion was transferred into a dialysis membrane and dialysed against 1 L of dist. water for three days. The water was changed every 24 hours.

Core-Shell Nanoparticles

A two-stage inverse microemulsion polymerization was used to obtain the positively charged core-shell nanoparticles. For a typical approach a solution of 3.08 g of Brij 30 and 0.5 g (1.4 mmol) of CTAB in 43 mL of hexane was purged with argon for one hour. The monomer solution for preparation of the nanoparticle core consisted of 0.4 g (2.6 mmol) of *N,N*-dimethyl-3-aminopropyl acrylamide (DMAA), 0.09 g (0.6 mmol) of MBAAm and 0.1 mg of **R3** dissolved in 0.8 mL of a 5 mM phosphate buffer (pH 7.2). The solution was heated up to 40 °C to completely dissolve the monomers and 0.22 mL of conc. HCl was added to obtain a pH of around 7. Afterwards, 1 mL of this monomer solution was added dropwise and under extensive stirring to the hexane solution. The polymerization was started by adding 40 μ L of an aqueous APS solution (20 wt.-% APS) and 6 μ L of TEMED at room temperature. After one hour of stirring 0.9 g of Brij 30 were added. To this mixture the monomer solution for the nanoparticle shell consisting of 0.4 g (5.6 mmol) of AAm,

0.09 g of MBAAm (0.6 mmol) and 0.5 mg of N2 in 1 mL of phosphate buffer pH 7.2 was added slowly. The mixture became slightly turbid and was polymerized using 40 μL of an aqueous APS solution (20 wt.-% APS) and 6 μL of TEMED. The reaction was stirred for further three hours at room temperature and then hexane was removed by evaporation. To precipitate the NPs the cloudy residue was suspended in 100 mL of ethanol. Upon centrifugation and washing four times with each 75 mL of ethanol, the purified particles were dried *in vacuo* at room temperature.

7.2.3 Cell Transfection Procedure

Chinese hamster ovary (CHO) and mouse fibroblasts cells were grown on coverslips and transfected with the nanosensors by using the conventional lipofectamine technique. The ratiometric nanobeads (3 mg) were mixed with 100 μL of EC buffer (6 mM Tris-HCl [pH 7.6], 1 M NaCl, 100 mM EDTA [pH 8.0], 0.5% polyoxyethylene 20 cetyether [Brij 58], 0.2% deoxycholate, 0.5% N-laurylsarcosyl), vortexed for 1 min, and sonicated for 3 min. Then 12 μL of Effecten (QIAGEN) and 300 μL of Optimem (INVITROGEN) were added, and the dispersion was again sonicated for 3 min. Cells were superfused with 300 μL of this mixture after removal of the cell culture medium. After an incubation period of 3 h in a 5% CO_2 atmosphere at 37°C, the nanoparticle/liposome mixture was removed by extensive washing. For confocal imaging, the coverslips were transferred to a custom-built microscope chamber that was superfused with phosphate-buffered solutions (pH 7.4) containing 9 mM Na_2HPO_4 , 2.1 mM NaH_2PO_4 , 10 mM glucose, 1 mM MgSO_4 , and potassium chloride in concentrations of 0, 10 and 50 mM, respectively. The chloride concentration was complemented with potassium gluconate to yield a constant osmolarity of 300 osmol/L. To ensure equilibration of $[\text{Cl}^-]$ with the extracellular solution, tributyltin(IV)chloride (40 μM , SIGMA, St.Louis, USA) and nigericin (10 μM) were added.

Bibliography

- (1) Montalti, M.; Credi, A.; Prodi, L.; Gandolfi, M. T. *Handbook of Photochemistry 3rd Edt.*; CRC Press Taylor & Francis, Florida, 2006.
- (2) Valeur, B. *Molecular Fluorescence-Principles and Applications*; Wiley-VCH, Weinheim, 2002.
- (3) Lakowicz, J. R. *Principles of Fluorescence Spectroscopy*; Plenum Press, New York, 1986.
- (4) Bissell, R. A.; Calle, E.; deSilva, A.; deSilva, S. A.; Gunaratne, H. Q. N.; Habibiwan, J. L.; Peiris, S. L. A.; Rupasinghe, R. A. D. D.; Samarasinghe, T. K. S. D.; Sandanayake, K. R. A. S.; Soumillion, J. P. J. *Chem. Soc.-Perkin Trans. 2* **1992**, 1559–1564.
- (5) Czarnik, A. *Fluorescent Chemosensors for Ion and Molecule Recognition*; American Chemical Society, Washington DC, 1993; Vol. 538.
- (6) Desvergne, J. P.; Czarnik, A. W. *Chemosensors of Ion and Molecule Recognition (NATO Science Series, Serie C. Mathematical and Physical Sciences)*; Kluwer Academic, London, 1997.
- (7) Tusa, J.; He, H. J. *Mater. Chem.* **2005**, *15*, 2640–2647.
- (8) Yushchenko, D. A.; Vadzyuk, O. B.; Kosterin, S. O.; Duportail, G.; Mely, Y.; Pivovarenko, V. G. *Anal. Biochem.* **2007**, *369*, 218–225.
- (9) Dahan, M.; Levi, S.; Luccardini, C.; Rostaing, P.; Riveau, B.; Triller, A. *Science* **2003**, *302*, 442–445.
- (10) Tsien, R. Y. *Annu. Rev. Neurosci.* **1989**, *12*, 227–253.
- (11) Kress-Rogers, E.; Brimelow, C. J. B. *Instrumentation and Sensors in the Food Industry*, 2nd ed.; Woodhead Publishing Ltd., Cambridge, 2001.
- (12) Wolfbeis, O. S. *Anal. Chem.* **2008**, *80*, 4269–4283.
- (13) Barker, S.; Thorsrud, B.; Kopelman, R. *Anal. Chem.* **1998**, *70*, 100–104.
- (14) Park, E.; Reid, K.; Tang, W.; Kennedy, R.; Kopelman, R. *J. Mater. Chem.* **2005**, *15*, 2913–2919.
- (15) Graefe, A.; Haupt, K.; Mohr, G. *Anal. Chim. Acta* **2006**, *565*, 42–47.

-
- (16) Mohr, G.; Spichiger, U.; Jona, W.; Langhals, H. *Anal. Chem.* **2000**, *72*, 1084–1087.
- (17) Nezel, T.; Fakler, A.; Zhylyak, G.; Mohr, G.; Spichiger-Keller, U. *Sens. Actuat. B-Chemical* **2000**, *70*, 165–169.
- (18) Borisov, S. M.; Klimant, I. *Analyst* **2008**, *133*, 1302–1307.
- (19) Buck, S.; Xu, H.; Brasuel, M.; Philbert, M.; Kopelman, R. *Talanta* **2004**, *63*, 41–59.
- (20) Tsien, R. Y. *Biochemistry* **1980**, *19*, 2396–2404.
- (21) Grynkiewicz, G.; Poenie, M.; Tsien, R. Y. *J. Biol. Chem.* **1985**, *260*, 3440–3450.
- (22) Meier, B.; Werner, T.; Klimant, I.; Wolfbeis, O. S. *Sens. Actuat. B-Chemical* **1995**, *29*, 240–245.
- (23) Clark, H.; Hoyer, M.; Philbert, M.; Kopelman, R. *Anal. Chem.* **1999**, *71*, 4831–4836.
- (24) Gouanve, F.; Schuster, T.; Allard, E.; Meallet-Renault, R.; Larpent, C. *Adv. Funct. Mat.* **2007**, *17*, 2746–2756.
- (25) Park, E. J.; Brasuel, M.; Behrend, C.; Philbert, M. A.; Kopelman, R. *Anal. Chem.* **2003**, *75*, 3784–3791.
- (26) Sun, H.; Scharff-Poulsen, A. M.; Gu, H.; Almdal, K. *Chem. Mater.* **2006**, *18*, 3381–3384.
- (27) Aylott, J. *Analyst* **2003**, *128*, 309–312.
- (28) Nelson, D. L.; Cox, M. M. *Lehninger Biochemie*; Springer-Verlag Berlin Heidelberg, 2001.
- (29) Belguise-Valladier, P.; Behr, J. P. *Cytotechnology* **2001**, *35*, 197–201.
- (30) Sonawane, N. D.; Szoka, F. C.; Verkman, A. S. *J. Biol. Chem.* **2003**, *278*, 44826–44831.
- (31) Panyam, J.; Zhou, W. Z.; Prabha, S.; Sahoo, S. K.; Labhasetwar, V. *FASEB Journal* **2002**, *16*, 1217–1226.
- (32) Vasir, J. K.; Labhasetwar, V. *Adv. Drug Deliv. Rev.* **2007**, *59*, 718–728.
- (33) Ow, H.; Larson, D.; Srivastava, M.; Baird, B.; Webb, W.; Wiesner, U. *Nano Lett.* **2005**, *5*, 113–117.
- (34) Hladky, S.; Rink, T. *Body Fluid and Kidney Physiology*; Hodder Arnold, London, 1986.
- (35) Ashcroft, F. M. *Ion Channels and Disease*; Academic Press, San Diego, 2000.
- (36) Boron, W. F.; Boulpaep, E. L. *Medical Physiology*; Elsevier Saunders, Philadelphia, 2003.

- (37) Demaurex, N. *News Physiol. Sci.* **2002**, *17*, 1–5.
- (38) Brasuel, M.; Miller, T.; Kopelman, R.; Philbert, M. *Analyst* **2003**, *128*, 1262–1267.
- (39) Geddes, C.; Apperson, K.; Karolin, J.; Birch, D. *Dyes Pigm.* **2001**, *48*, 227–231.
- (40) Krapf, R.; Illsley, N.; Tseng, H.; Verkman, A. *Anal. Biochem.* **1988**, *169*, 142–150.
- (41) Geddes, C. *Dyes Pigm.* **2000**, *45*, 243–251.
- (42) Biwersi, J.; Tulk, B.; Verkman, A. *Anal. Biochem.* **1994**, *219*, 139–143.
- (43) Kermis, H.; Kostov, Y.; Rao, G. *Analyst* **2003**, *128*, 1181–1186.
- (44) Kraayenhof, R.; Sterk, G. J.; Sang, H. W. W. F. *Biochemistry* **1993**, *32*, 10057–10066.
- (45) Rink, T.; Tsien, R.; Pozzan, T. J. *Cell Biol.* **1982**, *95*, 189–196.
- (46) Paradiso, A.; Tsien, R.; Machen, T. *Proceed. Nat. Acad. Sci. United States America-Biolog. Sci.* **1984**, *81*, 7436–7440.
- (47) Whitaker, J.; Haugland, R.; Prendergast, F. *Anal. Biochem.* **1991**, *194*, 330–344.
- (48) Daffy, L.; de Silva, A.; Gunaratne, H.; Huber, C.; Lynch, P.; Werner, T.; Wolfbeis, O. *Chem.-Eur. J.* **1998**, *4*, 1810–1815.
- (49) Geddes, C. *Measurement. Sci. & Techn.* **2001**, *12*, R53–R88.
- (50) McNamara, K.; Nguyen, T.; Dumitrascu, G.; Ji, J.; Rosenzweig, N.; Rosenzweig, Z. *Anal. Chem.* **2001**, *73*, 3240–3246.
- (51) Kreft, O.; Javier, A. M.; Sukhorukov, G. B.; Parak, W. J. *J. Mater. Chem.* **2007**, *17*, 4471–4476.
- (52) Burns, A.; Ow, H.; Wiesner, U. *Chem. Soc. Rev.* **2006**, *35*, 1028–1042.
- (53) Daubresse, C.; Grandfils, C.; Jerome, R.; Teyssie, P. J. *Colloid Interface Sci.* **1994**, *168*, 222–229.
- (54) Poulsen, A. K.; Arleth, L.; Almdal, K.; Scharff-Poulsen, A. M. *J. Colloid Interface Sci.* **2007**, *306*, 143–153, 55.
- (55) Munshi, N.; De, T. K.; Maitra, A. *J. Colloid Interface Sci.* **1997**, *190*, 387–391, 141.
- (56) Candau, F.; Leong, Y. S.; Fitch, R. M. *J. Polym. Sci., Part A: Polym. Chem.* **1985**, *23*, 193–214.
- (57) Murray, M. J.; Snowden, M. J. *Adv. Colloid Interface Sci.* **1995**, *54*, 73–91.
- (58) Graefe, A.; Stanca, S. E.; Nietzsche, S.; Kubicova, L.; Beckert, R.; Biskup, C.; Mohr, G. J. *Anal. Chem.* **2008**, *80*, 6526–6531.

- (59) Rauhut, M. M.; Sheehan, D.; Clarke, R. A.; Roberts, B. G.; Semsel, A. M. *J. Org. Chem.* **1965**, *30*, 3587–3592.
- (60) Huber, C.; Fahrnich, K.; Krause, C.; Werner, T. *J. Photochem. Photobiol., A* **1999**, *128*, 111–120.
- (61) Lobnik, A.; Oehme, I.; Murkovic, I.; Wolfbeis, O. S. *Anal. Chim. Acta* **1998**, *367*, 159–165.
- (62) Ferguson, J.; Healey, B. G.; Bronk, K. S.; Barnard, S. M.; Walt, D. R. *Anal. Chim. Acta* **1997**, *340*, 123–131.
- (63) Schulz, A.; Hornig, S.; Liebert, T.; Birckner, E.; Heinze, T.; Mohr, G. *J. Org. Biomol. Chem.* **2009**, *7*, 1884 – 1889.
- (64) Niu, C. G.; Zeng, G. M.; Chen, L. X.; Shen, G. L.; Yu, R. Q. *Analyst* **2004**, *129*, 20–24.
- (65) Grabchev, I.; Sali, S.; Betcheva, R.; Gregoriou, V. *Eur. Polym. J.* **2007**, *43*, 4297–4305.
- (66) Trupp, S.; Hoffmann, P.; Henkel, T.; Mohr, G. *J. Org. Biomol. Chem.* **2008**, *6*, 4319–4322.
- (67) Niu, C. G.; Gui, X. Q.; Zeng, G. M.; Yuan, X. Z. *Analyst* **2005**, *130*, 1551–1556.
- (68) deSilva, A. P.; Gunaratne, H. Q. N.; Habibjiwan, J. L.; McCoy, C. P.; Rice, T. E.; Soumillion, J. P. *Angew. Chem., Int. Ed.* **1995**, *34*, 1728–1731.
- (69) Gunnlaugsson, T.; McCoy, C. P.; Morrow, R. J.; Phelan, C.; Stomeo, F. *Arkivoc* **2003**, 216–228.
- (70) deSilva, A. P.; Gunaratne, H. Q. N.; Gunnlaugsson, T.; Huxley, A. J. M.; McCoy, C. P.; Rademacher, J. T.; Rice, T. E. *Chem. Rev.* **1997**, *97*, 1515–1566.
- (71) Fuller, J. E.; Zugates, G. T.; Ferreira, L. S.; Ow, H. S.; Nguyen, N. N.; Wiesner, U. B.; Langer, R. S. *Biomaterials* **2008**, *29*, 1526–1532.
- (72) Hu, Y.; Litwin, T.; Nagaraja, A. R.; Kwong, B.; Katz, J.; Watson, N.; Irvine, D. J. *Nano Lett.* **2007**, *7*, 3056–3064.
- (73) Griffiths, J.; Cox, R. *Dyes Pigm.* **2000**, *47*, 65–71.

List of Figures

1.1	Jablonski diagram	7
1.2	Franck-Condon principle and resulting Stoke's shift	9
1.3	Static quenching	11
1.4	Rate constants for dynamic fluorescence quenching	11
1.5	Intermolecular photoinduced electron transfer (PET)	12
1.6	Intramolecular photoinduced electron transfer (PET)	13
1.7	Resonance energy transfer (RET)	14
1.8	Electrical double layer and zeta-potential of a particle	15
1.9	Glycine receptors in living neuron cells	17
1.10	General design of a chemical sensor	18
1.11	Schematic design of fluorophores for sensing of ions or molecules.	20
1.12	Typical design of a sensor nanoparticle	22
1.13	Common methods for delivering nanoparticles into cells	23
1.14	Cellular uptake of NPs using the lipofectamine technique	24
1.15	Cellular uptake and endosomal escape of nanoparticles	25
1.16	Acridinium-based fluorophores for anion sensing	28
1.17	Fluorescent pH-indicators for the near neutral range	29
2.1	Preparation of cross-linked poly(acrylamide) nanoparticles	32
2.2	Pseudo-ternary phase diagram and size distribution graph	33
2.3	Structures of monomers, surfactants and initiators	34
2.4	Size distribution of the nanoparticles	35
2.5	SEM micrographs of nanoparticles	38
2.6	MAS- ¹³ C-ss-NMR spectra of AAm, MBAAm and the polymerized nanoparticles	39
2.7	Zeta potential of NPs polymerized with APS/TEMED and AAPH	41
2.8	Investigated chloride-sensitive fluorophores	42
2.9	Synthesis of the polymerizable reference dye R3	43
2.10	Size distribution by DLS and SEM micrograph of NPs doped with lucigenin and R3	44
2.11	Absorption and emission spectra of lucigenin and the reference dye R3 in solution	45
2.12	Excitation and emission spectra of NPs containing lucigenin and R3	46
2.13	Emission spectra of NPs containing lucigenin and R3 before and after dialysis	47
2.14	Emission spectra and Stern-Volmer plot of lucigenin in solution	48
2.15	Emission spectra and Stern-Volmer plot of NPs	48

2.16	Sensitivity of the NPs	49
2.17	Effect of pH on fluorescence of lucigenin	49
2.18	Effect of BSA on fluorescence of lucigenin	51
2.19	Oxidation of lucigenin to <i>N</i> -methyl acridone by hydrogenperoxide	52
2.20	Confocal micrographs of CHO cells incubated with nanosensors	53
2.21	Intracellular chloride calibration in mouse fibroblasts	54
2.22	Structure of the investigated pH-indicator dyes	57
2.23	Structure of HPTS	57
2.24	Synthesis of a polymerizable fluorescein derivative	59
2.25	Synthesis of the polymerizable pH-indicator dyes N1 and N2	60
2.26	SEM micrograph of NPs doped with N2 and R3	61
2.27	Absorption, excitation and emission spectra of N2 in solution	62
2.28	Excitation and internal charge transfer of N2	63
2.29	pH-Indicator dye N2 showing photoinduced electron transfer	64
2.30	Excitation and emission spectra of NPs with the pH-indicator dye N2 and R3	65
2.31	Emission spectra of pH-sensitive NPs before and after dialysis	66
2.32	Emission spectra and calibration graph of N2 in solution	67
2.33	Emission spectra and calibration graph of the pH-sensitive NPs	68
2.34	Effect of increasing ionic strength on the pH-sensitive NPs	69
2.35	Emission spectra of N2 and R3 in absence and presence of BSA	70
2.36	Emission spectra and calibration graph of the NPs in presence of BSA	71
2.37	Photostability of the dyes inside the NPs	72
3.1	Coating of poly(AAm) NPs with poly(ethyleneimine)	74
3.2	Schematic drawing of PDEAMA NPs and mechanism of pH-induced swelling	76
3.3	Hydrodynamic diameter of the PDEAMA NPs depending on the pH	77
3.4	Fluorescence spectra of PDEAMA NPs containing N2 or R3	78
3.5	Schematic drawing of the core-shell NPs	79
3.6	Hydrodynamic diameter of the PDMAPA-core/PAAm-shell NPs	80
3.7	Zeta-potential of the PDMAPA-core/PAAm-shell NPs	81
3.8	Excitation and emission spectra of N2 and R3 inside the PDMAPA-core/PAAm-shell NPs	81
3.9	Response and calibration plot of the PDMAPA-core/PAAm-shell NPs	82
B.1	MAS-SS- ¹³ C-NMR spectrum of acrylamide.	115
B.2	MAS-SS- ¹³ C-NMR spectrum of methylene bisacrylamide.	116
B.3	MAS-SS- ¹³ C-NMR spectrum of nanoparticles.	116

List of Tables

2.1	Composition of the w/o microemulsions	35
2.2	Size and polydispersity of the NPs depending on the initiator	36
2.3	Determined BET-surfaces, densities and theoretical diameters of different NPs	39
2.4	¹³ C-NMR shifts of the monomers, the particles and the surfactants	40
2.5	Absorption/excitation and emission wavelengths, quantum yields and extinction coefficients of lucigenin and R3	45
2.6	Spectral properties of the investigated pH-indicators	58
2.7	Influence of immobilized dyes on properties of nanoparticles	60
2.8	Absorption, excitation and emission wavelengths of dissolved and immobilized N2	65
3.1	Composition of the coating solutions	74
3.2	Excitation/emission wavelengths and Stoke's shift of N2 and R3 inside core-shell NPs	80
A.1	Spectral properties of the investigated fluorophores	114

Appendix A

Investigated Fluorophores

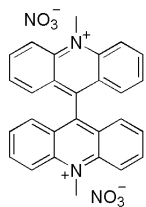
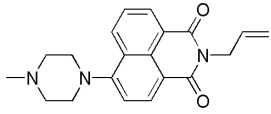
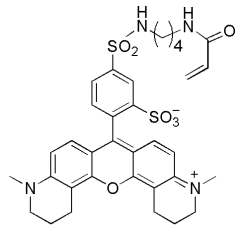
Fluorophore	λ_{exc} [nm]	λ_{em} [nm]	Stoke's shift [nm]	ϕ	ϵ [$M^{-1}cm^{-1}$]
 <p>Lucigenin</p>	369, 431 (pH 7.2)	503 (pH 7.2)	134	0.37	32000
 <p>N2</p>	388 (pH 4) 399 (pH 9)	529 (pH 4) 536 (pH 9)	141 137	0.45 $4.2 \cdot 10^{-2}$	10000 10000
 <p>R3</p>	582 (pH 7.2)	602 (pH 7.2)	20	0.35	40000

Table A.1: Excitation/emission maxima, Stoke's shift, quantum yield and molar extinction coefficient of the fluorophores in aqueous buffered solution.

Appendix B

Spectra

^{13}C -Solid State-NMR Spectra

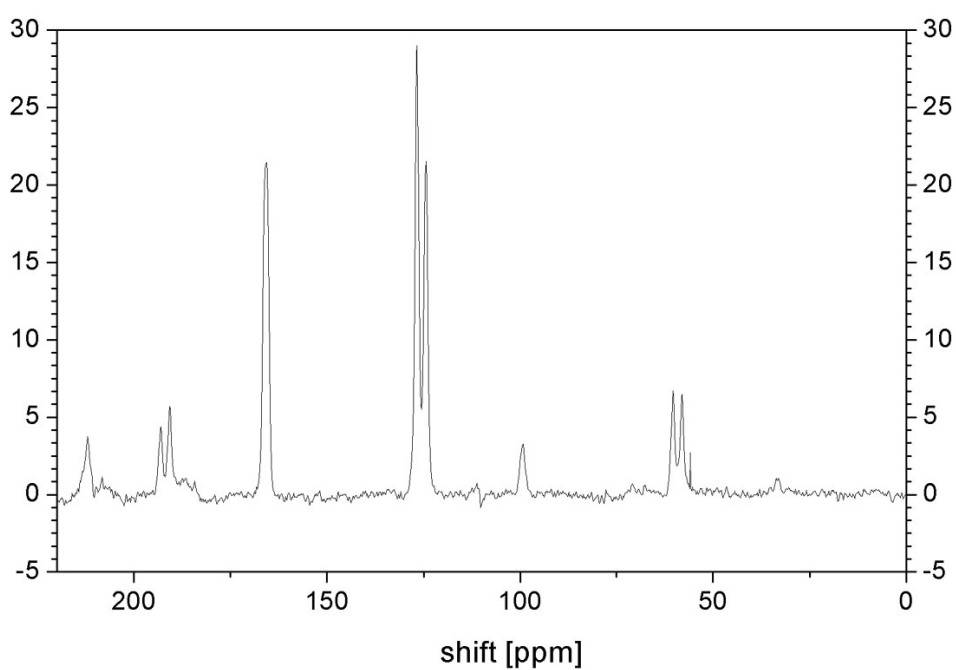


Figure B.1: MAS-SS- ^{13}C -NMR spectrum of acrylamide.

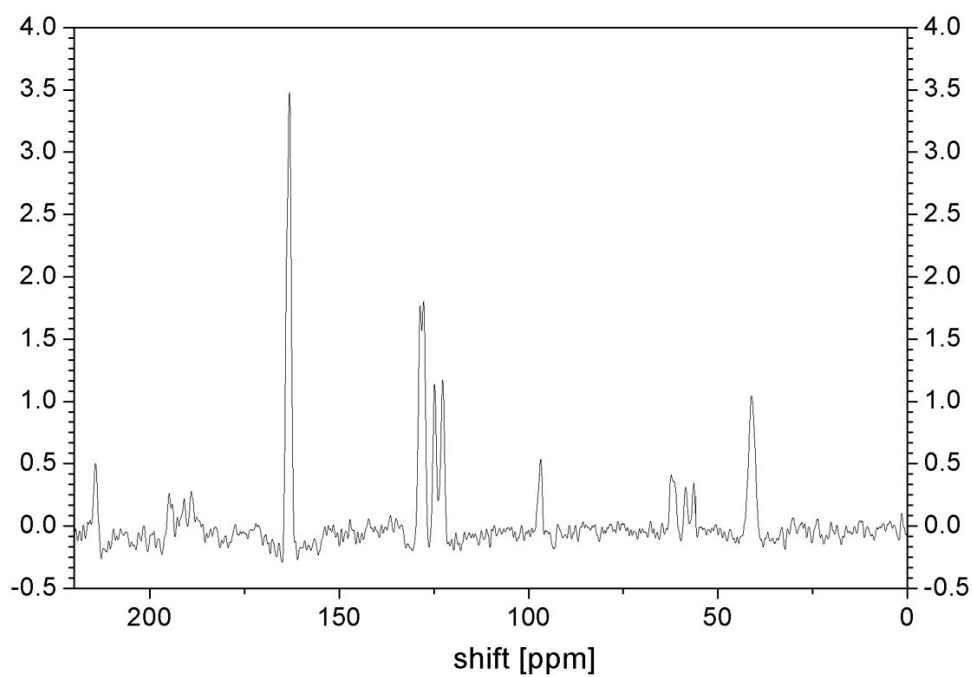


Figure B.2: MAS-SS-¹³C-NMR spectrum of methylene bisacrylamide.

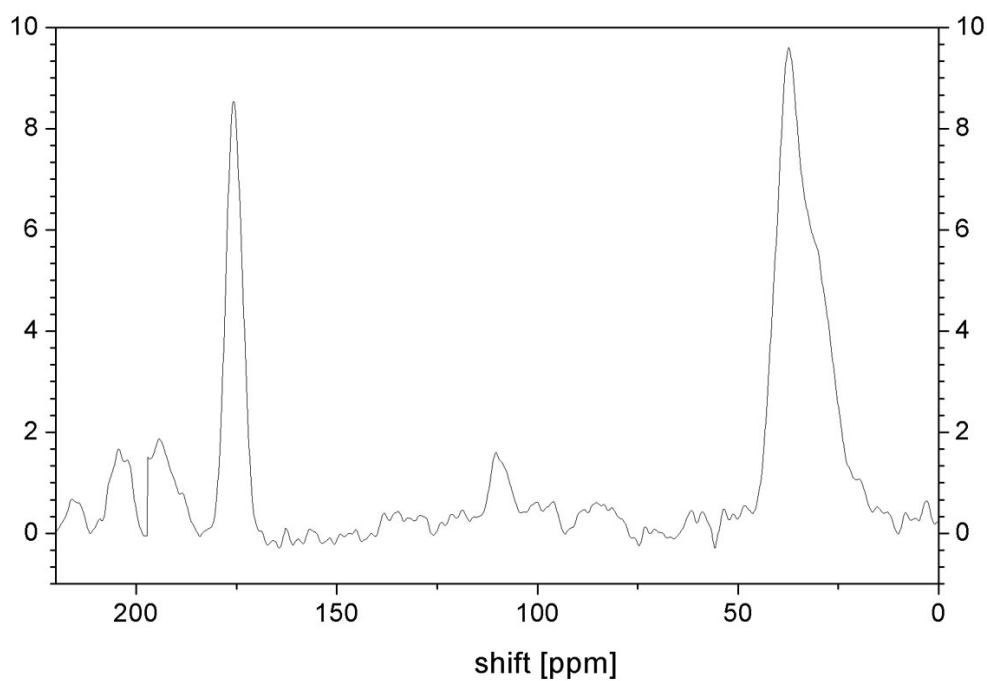


Figure B.3: MAS-SS-¹³C-NMR spectrum of nanoparticles.

List of Publications

Publications in refereed journals

1. Anja Gräfe, Karsten Haupt, Gerhard J. Mohr *Anal. Chim. Acta*, **2006**, *565*, 42-47. *Optical Sensor Materials for the Detection of Amines in Organic Solvents.*
2. Stephanie Hornig, Christoph Biskup, Anja Gräfe, Jana Wotschadlo, Tim Liebert, Gerhard J. Mohr, Thomas Heinze *Soft Matter*, **2008**, *4*, 1169–1172. *Biocompatible Fluorescent Nanoparticles for pH-Sensing.*
3. Anja Gräfe, Sarmiza E. Stanca, Sandor Nietzsche, Lenka Kubicova, Rainer Beckert, Christoph Biskup, Gerhard J. Mohr *Anal. Chem.*, **2008**, *80*, 6526-6531. *Development and Critical Evaluation of Fluorescent Chloride Nanosensors.*
4. María Comes, M. Dolores Marcos, Ramón Martínez-Máñez, Félix Sancenón, Luis A. Villaescusa, Anja Gräfe, Gerhard J. Mohr *J. Mater. Chem.*, **2008**, *18*, 5815–5823. *Hybrid Functionalised Mesoporous Silica - Polymer Composites for Enhanced Analyte Monitoring using Optical Sensors.*
5. Anja Schulz, Stepahnie, Hornig, Tim Liebert, Eckhard Birckner, Thomas Heinze, Gerhard J. Mohr, *Organic Biomol. Chem.*, **2009**, *7*, 1884 – 1889. *Evaluation of Fluorescent Polysaccharide Nanoparticles for pH-Sensing.*

Conferences

1. Talk: "Development of Chemically Reactive Dyes for MIPs in Order to Foster Selective Recognition Processes." 3rd Graduate Student Symposium in Molecular Imprinting, 17. Februar 2006, Universität Dortmund
2. Poster: "Fluoreszierende Sensornanopartikel für die intrazelluläre Bestimmung von Ionenkonzentrationen." ANAKON 2007, 27.-30. März 2007, FSU Jena
3. Talk: "Design of Fluorescent Sensor Nanoparticles for Intracellular Chloride Determination." Internationaler Workshop im Rahmen des SNIB-Projekts, 22.-23. Juni 2007, FSU Jena

4. Talk: "Fluorescent Sensor Nanoparticles for Intracellular Chloride Determination." First NASCENT International Meeting 2007, 10.-12. September 2007, Queen Mary Universität London
5. Poster: "Fluorescent Sensor Nanoparticles for Intracellular Chloride Determination." 2. Symposium "Nanotechnology and Toxicology in Environment and Health" 2.-3. April 2008, Helmholtz-Zentrum für Umweltforschung Leipzig

Curriculum Vitæ

Persönliche Daten

Name: Anja Schulz, geb. Gräfe
Geburtsdatum: 05.12.1981
Geburtsort: Merseburg/Saale
Familienstand: verheiratet
Staatsangehörigkeit: deutsch

Ausbildung/

wissenschaftlicher Werdegang

1988 bis 1992 Besuch der Grundschule in Gera
1992 bis 2000 Besuch des Karl-Theodor-Liebe-Gymnasiums in Gera
09/2000 bis 08/2005 Studium der Chemie an der Friedrich-Schiller-Universität Jena
12/2004 bis 08/2005 Anfertigung der Diplomarbeit „Development of chemically reactive dyes for MIPs in order to foster selective recognition processes“ in der Arbeitsgruppe von PD Dr. Gerhard J. Mohr
12.08.2005 Abschluss des Studiums als Diplom-Chemikerin
seit 09/2005 Wissenschaftliche Mitarbeiterin in der Arbeitsgruppe von PD Dr. Gerhard J. Mohr
02/2006 bis 05/2009 Anfertigung der Dissertation mit dem Titel „Fluorescent Nanoparticles for Ion Sensing“ im Rahmen des DFG-Projekts „Multifunctional Molecular Structures for Biotechnology and Clinical Diagnostics“ (MO 1062/2-1 und 2-2)

Danksagung

Ich möchte mich an erster Stelle bei meinem wissenschaftlichen Betreuer Herrn Dr. Gerhard Mohr dafür bedanken, dass er mir die Möglichkeit gegeben hat ein spannendes und interessantes Thema zu bearbeiten. Durch sein Engagement war es mir möglich an zahlreichen Konferenzen teilzunehmen und von internationalen Kooperationen zu profitieren. Prof. Dr. Thomas Heinze danke ich für die Anfertigung des Zweitgutachtens.

Allen, auch ehemaligen, Mitarbeitern der Arbeitsgruppe gebührt ein großer Dank für die schöne Arbeitsatmosphäre, die Unterstützung bei Problemen im Laboralltag und die bereichernden Diskussionen. Danken möchte ich auch allen Mitarbeitern des Instituts für Physikalische Chemie, insbesondere Frau Dr. Berg (MS), Dr. Jochen Schmidt, Frau Anna Schmidt (BET, Dichtemessungen, DLS), Dr. Hergen Breitzke (Festkörper-NMR) und Frau Preuße. Mein spezieller Dank gilt Heidrun Müller für die Messung der Quantenausbeuten und Dr. Eckhard Birckner für die produktive Zusammenarbeit.

Des Weiteren möchte ich Frau Dr. Sarmiza Stanca und Dr. Christoph Biskup für die Durchführung der Zellexperimente und die Einführung in die konfokale Fluoreszenzmikroskopie danken. Ich möchte mich bei Frau Dr. Stephanie Hornig für die Aufnahme der SEM-Bilder und die gute Zusammenarbeit bedanken. Ebenfalls danke ich Jana Wotschadlo, Dr. Tim Liebert, Prof. Dr. Rainer Beckert für die fruchtbare Kooperation. Außerdem danke ich den Mitarbeitern des Instituts für Organische Chemie und Makromolekulare Chemie für die Aufnahme der NMR-Spektren und die Elementaranalysen, sowie den Mitarbeitern des Elektronenmikroskopischen Zentrums. Der Arbeitsgruppe um Prof Dr. Fahr in der Pharmazeutischen Technologie danke ich für die Bereitstellung des DLS.

Besonderen Danke schulde ich meinen Freunden, Kommilitonen und der Mensarunde für die sehr schöne Zeit während meiner Promotion. Außerdem möchte ich mich herzlich bei den Korrekturlesern dieser Arbeit für ihre Mühe und Geduld bedanken. Ein spezielles Dankeschön geht an Martin und meine Familie für den Rückhalt und die Unterstützung bei Problemen aller Art.

Selbständigkeitserklärung

Ich erkläre, dass ich die vorliegende Arbeit selbständig und unter Verwendung der angegebenen Hilfsmittel, persönlichen Mitteilungen und Quellen angefertigt habe.

Jena, den 08. Mai 2009